Politecnico di Torino

ScuDo
Scuola di Dottorato ~ Doctoral School
WHAT YOU ARE, TAKES YOU FAR

Doctoral Dissertation
Doctoral Program in Electrical, Electronics and Communications Engineering
(35^{th}cycle)

Physics-based modeling of 850 nm Tunnel Junction VCSELs

By

Alberto Gullino

******

Supervisor(s):
Prof. Michele Goano, Supervisor
Prof. Francesco Bertazzi, Co-Supervisor
Prof. Giovanni Ghione, Co-Supervisor
Dr. Pierluigi Debernardi, Co-Supervisor

Doctoral Examination Committee:
Prof. Guilhem Almuneau, Referee, LAAS-CNRS
Prof. Wolfgang Elsäßer, Referee, Technischen Universität Darmstadt

Politecnico di Torino
2023

Declaration

I hereby declare that the contents and organization of this dissertation constitute my own original work and does not compromise in any way the rights of third parties, including those relating to the security of personal data.

Alberto Gullino
2023

* This dissertation is presented in partial fulfillment of the requirements for **Ph.D. degree** in the Graduate School of Politecnico di Torino (ScuDo).

I would like to express my heartfelt dedication to my parents who have unwaveringly believed in me since the beginning of my university experience, providing me with not just words of encouragement but also standing by my side during the most challenging decisions.

Acknowledgements

I would like to dedicate this thesis to my parents, that helped and sustained me in any possible way throughout my years of studies and research. Then, I wish to extend my gratitude to my entire family for their exceptional support during the three years of this journey, with a special mention to my brothers, Federico and Davide. A heartfelt thanks goes to my closest friends, and especially to Alberto, Angelo, Davide, Edoardo and Iacopo, for standing by my side during the most challenging times. Then, I wish to praise my colleagues Matteo, Eva and Gemma, with whom I have shared both laughs and difficult times. Their camaraderie and support in the MOG group made my experience much more enjoyable from the very first day we met. I could not have asked for better fellows, that now I can call friends.

With regards to my work, I would like to express my gratitude to my tutor Prof. Michele Goano, for providing me financial support and technical help with every bureaucratic detail. I also wish to extend my appreciation to Dr. Alberto Tibaldi, who introduced me to the physics-based simulations and various other fascinating topics, not to mention all the insights crucial to solve a wide number of issues, in collaboration with Prof. Francesco Bertazzi. Last but not least, I must offer a special thanks to Dr. Pierluigi Debernardi, who patiently guided and trained me towards the mastering of the already developed codes. Nothing would have been achieved without their support.

Abstract

The challenges posed by the exponentially growing market of hyperscale datacenters require high-speed components, able to withstand harsh conditions during their operations. In this framework, with optical interconnects by now dominant in short-communication links, AlGaAs Vertical-Cavity Surface-Emitting Lasers (VCSELs) take crucial importance. State-of-the-art 850–980 nm VCSELs emit circular beams that are easily coupled to optical fibers and capable of delivering single-mode powers up to some mW. These are based on *pin*-like junctions, where stimulated emission occurs in multi-quantum wells (MQWs), inserted in the intrinsic cavity. Carriers reach the MQWs through oppositely doped distributed Bragg's reflectors (DBRs). Electrical and optical confinement comes from an oxide aperture placed in the proximity of the cavity.

The thesis aims at providing a preliminary assessment of an alternative design, to pave the way for the next generation of VCSELs. A sizable limitation to *pin* VCSELs comes from the massive presence of *p*-doping in the top DBR. This inherently induces worse electrical conductivity and stronger free-carrier absorption losses. Moreover, the wet oxidation process is not capable of growing small oxide apertures for single-mode emission with high reliability. For different reasons, these issues have been addressed in III-nitride, InP and GaSb-based VCSELs by adopting tunnel junctions (TJs). In fact, in AlGaN devices relevant *p*-doping levels cannot be realized due to high acceptor ionization energies. Additionally, oxide aperture concept is hardly reproducible in nitride, InP and GaSb systems due to the absence of Al-rich layers. TJs effectively inject holes in the active regions, allowing *n*-doping in the top DBR. Radially defined TJs are used to realize lateral confinement. Our goal is to verify whether TJ benefits can be transferred to AlGaAs VCSELs.

Pin VCSELs market pervasion prompts a technologically computed-aided design approach. In this perspective, we adopt our in-house tool VENUS, a quantum-

corrected drift-diffusion (DD) solver dealing self-consistently with the connected optical and thermal problems. Our physics-based framework allows to go beyond the phenomenological rate equations model, a fundamental tool to interpret results of any laser, that fails to predict in depth the effectiveness of new concepts. The merits of various designs can be assessed by inspecting a wide set of inner quantities, that determine the output figures of merits. Eventually, a crucial difference with respect to commercial software is the full control over the simulation parameters and models.

TJ modeling cannot be realized within a semiclassical model, as carrier transport mainly depend on quantum interband tunneling across a reversely biased heavily doped *pn* junction. Non-equilibrium Green's function (NEGF) approach is exploited here as a genuine quantum treatment of TJ interband current. This is ultimately converted into a net generation rate introduced in the DD model. The novel NEGF-DD scheme is initially applied to a 1D version of VENUS: D1ANA. First, this is properly calibrated to extract reliable results on a reference *pin* VCSELs. Then, a TJ-VCSEL obtained from minor modifications of the reference device is generated as a test-bed for the proposed approach. As a final step, the NEGF-DD scheme enters VENUS. The lateral features neglected in D1ANA are explored for two TJ-VCSELs with varying reciprocal position of TJ and oxide aperture. An optimal design is defined, with TJ above the oxide aperture, ensuring a current confinement comparable to the *pin* device. Static electrical and optical characteristics confirm quantitatively the predictions of D1ANA. The voltage drop across the TJ increase the differential resistance. The optical characteristics are enhanced: the maximum output powers are almost doubled at heat sink temperatures ranging from 20 to 110°C, keeping the threshold current and the modal spectrum unchanged, thanks to lower self-heating and top DBR doping conversion.

Contents

List of Figures

List of Tables

Symbols

Roman Symbols

$\bar{n}$ VCSEL effective refractive index used in (3.2)

$\mathbf{A}$ Matrix containing all the mode amplitudes in (2.15)

$\mathbf{B}$ Free-propagation constant matrix describing field propagation in the reference medium, (2.15)

$\mathscr{E}_m(z,\rho)$ Optical modal field throughout the VCSEL, from VELM

A_ν Amplitude of the mode ν in (2.14)

B^{rad} Radiative recombination coeffecient, Tab. 3.1

$C_{n/p}^{\mathrm{Aug}}$ Electron and hole Auger recombination coeffecient, Tab. 3.1

$C_{\mathrm{cap},n/p}$ Net electron and hole capture rate, defined in (2.6)–(2.7) and entering in (2.2)–(2.5)

$D_{n/p}$ Electron and hole diffusivity

$E(\rho,\phi,z)$ Electromagnetic field expressed in cylindrical coordinates as (2.14)

$E_{\mathrm{C,V}}$ Conduction and valence band edge energy, defined in (A.3)

$E_{\mathrm{F},n/p}$ Electron and hole quasi-Fermi level, defined in (A.4)–(A.5)

E_g Energy gap

f Signal frequency

f_{corr} Corrective factor defined as (2.24), accounting for the total power unbalancing

f_{TJ} Fitting factor for the TJ heating terms, used in (5.1) and (5.3)

g QW gain extracted from the LUT according to N_{2D}, P_{2D}, λ_m, T

G_{BTBT} Band-to-band tunneling generation rate extracted from NEGF with (2.11)

G_{th} Gain at threshold

G_m Modal gain, defined in (2.17) and entering (2.13)

I_{bias} Bias current imposed by an external generator (current-controlled simulations), defined in (2.27)

I_{cont} Measured or simulated current at the contact of the device under test, computed as (2.28)

I_{leak} Leakage current

I_{th} Threshold current

J_{TJ} Current density across the TJ extracted from NEGF

$J_{n/p}$ Electron and hole current density, defined in (2.9)–(2.10) and entering in (2.2)–(2.5)

k Wavevector

k_{B} Boltzmann constant

L_{TJ} TJ length along z-direction

L_m Modal losses, from VELM, in (2.13)

$m^*_{n/p}$ Electron and hole effective mass, Tab. 3.1

M_i Generalized transmission matrix in layer z_i, entering (2.16)

n Electron density, defined in (A.1) and entering the drift-diffusion system (2.1)–(2.5)

N_{A} Acceptor doping concentration (N_{A}^-: ionized concentration, see (A.8))

$N_{\mathrm{C,V}}$ Conduction and valence band effective density of states

N_D Donor doping concentration (N_D^+: ionized concentration, see (A.7))

N_2 Maximum bound electron density allowed in a QW, entering (2.6)

n_i Intrinsic carrier density

n_r Refractive index

p Hole density, defined in (A.2) and entering the drift-diffusion system (2.1)–(2.5)

P_{elec} Input electrical power in (2.24)

P_{max} Peaj output optical power

P_{opt} Output optical power in (2.24)

P_{therm} Dissipated thermal power at each bias, entering in (2.24)

P_2 Maximum bound hole density allowed in a QW, entering (2.7)

q Elementary charge

r_{sp} QW spontaneous emission rate extracted from the LUT according to N_{2D}, P_{2D}, λ_m, T

S_m Spontaneous emission rate in the lasing mode, in (2.13)

T_{velm} Simulation parameter used to check if the maximum temperature variation is large enough to induce a relevant modification of VELM output parameters

$U_{n/p}$ Net electron and hole recombination rate inserted in in (2.9)–(2.10) and entering in (2.2)–(2.5)

V_{bias} Bias voltage imposed by an external generator (voltage-controlled simulations), defined in (2.27)

V_{cont} Measured or simulated drop across the contact of the device under test, computed as (2.25)

V_{TJ} Voltage drop across the TJ, computed as (B.2)

v_s Signal source, scheme in Fig. 3.9

V_T Thermal voltage

W_{opt} Optical standing wave in (2.19)

W_{QW} Quantum well width

Y Input admittance in parallel to ideal current generator and device under test (current-controlled simulations)

Z Input impedance in series between ideal voltage generator and device under test (voltage-controlled simulations)

z Longitudinal direction coordinate

Z_0 Generator characteristic impedance, scheme in Fig. 3.9

z_L p-side extreme point of the TJ

z_R n-side extreme point of the TJ

LP Linearly polarized modes (01: fundamental, denoted by $\circ$ – Gaussian shape; 11: first order mode, denoted by $\triangledown$; 02: second radial mode without azimuthal variations, denoted by $*$)

Greek Symbols

α Absorption coefficient defined in (4.1) and used in (2.19)

$\alpha_{\Gamma,L,X}$ Varshi model parameter for $E_g(T)$, Tab. 3.1

β_g Varshi model parameter for $E_g(T)$, Tab. 3.1

β_i Exponential fit coefficient of the TJ current density, used in (B.1)

β_T Exponent governing non linearity between temperature and thermal conductivity, Tab. 3.1 and (3.4)

χ Electron affinity, Tab. 3.1

$\Delta E_{\text{D,A}}$ Donor and acceptor activation energy, see (A.9)–(A.10)

$\Delta\lambda$ Cavity detuning, see Fig. 3.11

$\Delta_{C/V}$ Quantum barrier height used in (2.19)

ε Dielectric constant

ε_r Relative dielectric constant, Tab. 3.1

ε_{NL} Gain compression factor

η_{WP} Wall-plug Efficiency

Γ_z Longitudinal confinement factor, entering (2.13)

κ Thermal conductivity in (2.19)

λ Emission wavelength

λ_{nom} Nominal emission wavelength of the VCSEL, see Fig. 3.11

λ_{opt} Emission wavelength at which the gain in maximum, see Fig. 3.11

$\mu_{n/p}$ Electron and hole mobility

ν Generic mode of the complete basis used to expand the electromagnetic field in VELM

ω Signal pulsation

ϕ Electrostatic Potential in Poisson's equation (2.1)

ϕ_{bi} Built-in potential defined by (2.26)

ρ Radial direction coordinate

σ Electrical conductivity in (2.19)

τ^{cap} QW capture lifetimes in (2.6)–(2.7)

Superscripts

2D Bound quantity

3D Bulk quantity

$\sim$ Signal amplitude bias point introduced in (3.5)

Subscripts

Γ, L, X Brillouin Zone high symmetry critical points

DC Stationary bias point

sp Spontaneous emission recombination, see Appendix A.3.1

st Stimulated emission recombination

Other Symbols

∇ Gradient operator

∇^2 Laplacian operator

∂ Partial derivatives

Acronyms / Abbreviations

A-TJ-VCSEL Oxide-confined Tunnel junction VCSEL with oxide *above* the TJ

AR Active Region

Aug Auger recombination, see Appendix A.3.2

B-TJ-VCSEL Oxide-confined Tunnel junction VCSEL with oxide *below* the TJ

BTBT Direct Band-to-band quantum Tunneling

CB Conduction band edge

D1ANA Drift-diffusion 1-d ANAlysis

DBR Distributed Bragg's Reflector

DC Duty Cycle

DD Drift-diffusion system

EEL Edge-Emitting Laser

FCA Free-Carrier Absorption

FEM Finite Element Method

GR Generation-recombination

IR Infrared radiation

LDOS Local Density of States

LED Light-Emitting Diode

LiDAR Light Detection and Ranging

LIV Light-Current-Voltage characteristics

LUT Look-up table, where precomputed quantities are stored and then extracted

MBE Molecular Beam Epitaxy

MEM Morthar Element Method

MJ-VCSEL Multi-Junction VCSEL

MMF Multimode glass fiber

MOCVD Metal-Organic Chemical Vapour Deposition

MQW Multi-Quantum Well

NEGF Non-equilibrium Green's Function

PAM Pulse-Amplitude Modulation

QCDD Quantum-Corrected Drift-diffusion system

SF Size Factor used to calibrate D1ANA, see Section 3.1.1

SMI Self-mixing Interferometry

SRH Shockley-Read-Hall (or trap-assisted) recombination, see Appendix A.3.3

SW Optical Standing Wave

TCAD Technology Computer-Aided Design approach

TJ Tunnel Junction

UV Ultraviolet radiation

VB Valence band edge

VCSEL Vertical-Cavity Surface-Emitting Laser

VELM Vcsel ELectroMagnetic code

VENUS Vcsel Electro-opto-thermal NUmerical Simulator

ViP VCSELs with integrated photodiodes

WKB Wentzel-Kramers-Brillouin theory for tunneling

WPE Wall-plug Efficiency

Chapter 1

Introduction

Any telecommunication system conveys information from a source to the final user. The information is first converted into a signal and then the transmitter transfer it into a physical channel. Here, the signal propagates through a medium until it reaches the receiver. Eventually, the signal is converted back to a readable form for the final user. These tasks are accomplished following the steps depicted in the schematic of Fig. 1.1. Depending on the physical channel length, data transmission is classified into short-haul and long-haul. In short-haul communication, distances up to several hundreds meters for in-building cabling or local-area networks are covered. Long-distance communication connects cities and countries, linking people and infrastructures to the global network. From the beginning of electronic telecommunication era, the latter has been extensively improved to connect increasingly distant places. A result of those efforts is that even the farthest parts on the Earth (and even space) are now connected. Bell Labs are arguably the most famous company that have dealt with these issues throughout the entirety of the 20th century. Even though the research field of the data telecommunication (or *telecom*) is still in continuous expansion (5G or Starlink from SpaceX are just two excellent recent examples), the focus is shifting towards addressing challenges in short-distance communication, where a significant number of issues requires targeted solutions to keep up with the long-haul counterparts.

The most demanding requirements come from server racks and data-processing centers, where the main concerns are operational stability and high-speed connectivity. These are harsh environments where temperature up to 80°C are ordinarily

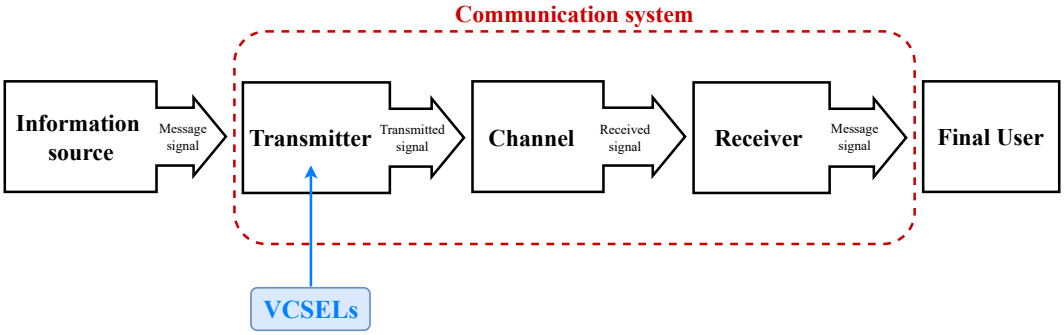

Fig. 1.1 Schematics of a generic communication system.

reached, thus limiting the performance of every device. Therefore, the single channel data rate doubling each 24 months in data storage has greatly limited the copper links applicability in favour of optical interconnects (OIs), also referred to as *optical datacom*. In OIs framework, a huge breakthrough has been provided by the introduction of Vertical-Cavity Surface-Emitting Lasers (VCSELs) coupled to multimode glass fibers (MMF) as transmitters [1]. First theorized by Prof. Kenichi Iga in 1977 [2], starting from mid 1980s 850 nm VCSELs have quickly replaced the light-emitting diodes (LED) and edge-emitting lasers (EELs) as light sources for short-reach communication links [3–8]. The reasons are manyfold. The emitting area of VCSELs translates into a circular far-field beam, thus providing high coupling efficiencies to optical fibers, wide modulation bandwidth even at low current levels, single-mode operation (due to its short cavity length), and reduced power consumption [9]. A VCSEL is able to deliver single mode optical power as large as few mW, limited by the small aperture required for maintaining sufficient discrimination against higher order transverse modes. Additionally, it facilitates large-scale cost-effective production due to its compatibility with inexpensive wafer-level fabrication techniques (such as ion implantation) and simple on-chip testing methods.

Moreover, the COVID-19 pandemic has brought even more attention to the need for enhanced intradatacenter links. Improving online services, which are at the core of modern entertainment, remote work, and distance education, represents a crucial challenge for the global interconnected system. As a result, efficient short-range data communication is becoming increasingly urgent. Clearly, novel design possibly improving state-of-the-art devices require extended campaigns of prototyping, which involve huge amount of time and resources during the trial-and-error procedure. To ease this process, a technology computer-aided design (TCAD) approach can

offer a qualitative description of VCSELs operation, provided that it must deal with multiscale and multiphysics problems, and account self-consistently with the closely interdependent optical, electric, and thermal problems.

1.1 VCSELs structure and applications

Let's now provide a brief overview about VCSELs, whose modeling is the subject of this thesis. VCSELs are semiconductor lasers emitting photons perpendicularly to their surface and parallel to its growth direction, a major difference with respect to the EEL, where light propagates parallel to the wafer surface on the semiconductor chip. A sketch of a typical VCSEL structure is shown in Fig. 1.2. From the electrical transport standpoint, state-of-the-art VCSELs usually are *pin* axisymmetric diodes, whose intrinsic region contains the cavity where active layers generate the emitted photons from stimulated emission process. In conventional devices, the active region (AR) comprises a set of stacked quantum wells (QWs), aligned to a maximum of the optical field. The oppositely doped sides correspond to the distributed Bragg's reflectors (DBRs) that provide optical feedback and select the emission wavelength, making VCSELs optically referable to as open dielectric resonators. Typically, VCSELs have a lateral size of 150–250 μm and a height of 100–300 μm, depending on the material system of choice.

DBRs consist of alternating sequences of high and low refractive index $\lambda/4$ layers (on the order of tens, with λ emission wavelength). Their spectral reflectivity depends on the refractive index step, where partial reflections at each interface add constructively. As a result, DBR reflectivity spectrum has a wide transmittance window centered around the emission wavelength, which is determined by the cavity length. Nevertheless, the mirrors should provide reflectivities larger than 97% to overcome the short gain length of the VCSEL cavity. Either dielectric (non-epitaxial) and semiconductor (epitaxial) DBRs are used to confine light in the longitudinal direction. Historically, dielectric DBRs have been the first to be produced from deposition of amorphous dielectric layers with oxides (SiO_2, HfO_2), nitrides (SiN_x), fluorides (MgF_2,...) [10]. Dielectric DBRs provide an optimal selective reflectivity but require additional efforts to solve the issues coming from their lack of thermal and electrical conductivity, such as the introduction of intra-cavity current spreading layer contacts. Therefore, dielectric DBRs are

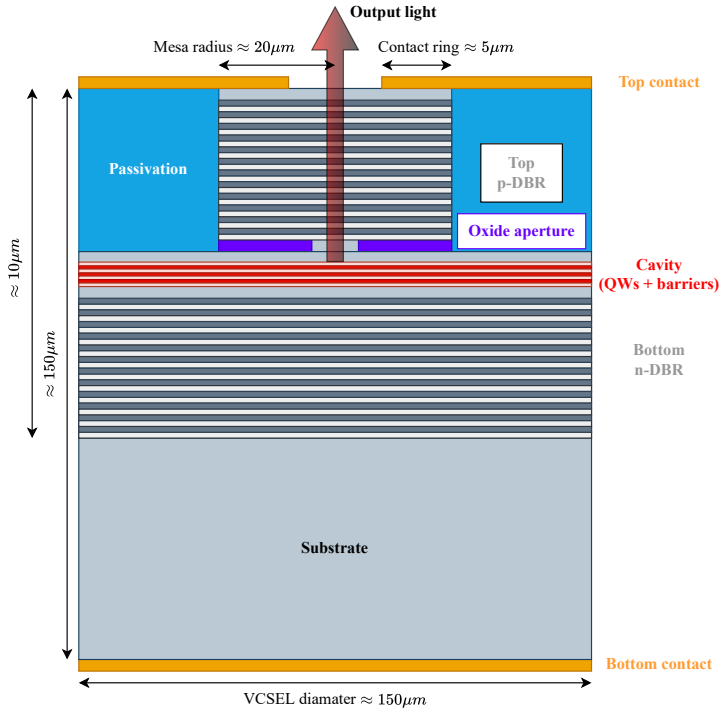

Fig. 1.2 Side view of an axisymmetric VCSEL structure.

often introduced in long-wavelength VCSELs when refractive index step of a given material system is not large enough to produce the mirror reflectivity needed to satisfy the round-trip condition (GaSb-based VCSELs [11]) or when doping becomes technologically problematic or even impossible (in case of III-nitride systems [12]) or when differences in lattice parameters between the stacked layers introduce strong strain effects [13]. On the other hand, semiconductor DBRs have been first introduced in 1983 in III-V VCSELs using molecular beam epitaxy (MBE) or metal-organic chemical vapour deposition (MOCVD) [14], enabling a continuous growth of full VCSEL structures. Ohmic contacts on top and bottom sides of the laser are used to inject the driving current, enhancing current uniformity reaching the cavity. Also, the smaller refractive index step in the semiconductor DBR layers with respect to the dielectric counterparts leads to thicker mirrors in the former case. Notice that at the photon emission side the contact becomes annular, with an inner radius larger than the oxide aperture radius, otherwise the dominant metal reflectivity would prevent photon escape and provoke strong absorption. Doping and composition grading must be introduced between semiconductor DBRs layers to avoid the creation of unwanted potential barriers preventing good electrical conductivity.

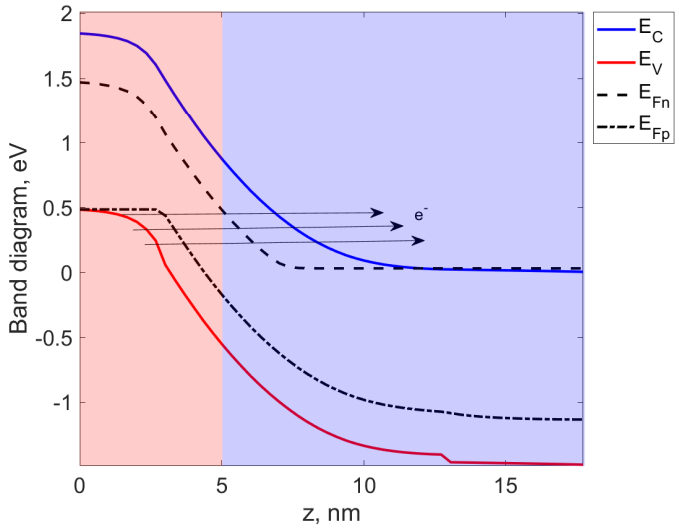

Fig. 1.3 TJ band diagram at 0.5 V, including also the quasi-Fermi levels (in black). Arrows indicate the tunneling path of electrons from the valence band of the p^{++} side (denoted by the red rectangle) to the conduction band of the n^{++} side (denoted by the blue rectangle).

Usually, *p*-on-*n* configuration is preferred to *n*-on-*p*, due to the larger defect densities of *p*-doped layers, that impact on the electrical conductivity and on the free-carrier absorption losses. Electrical and optical confinement are crucial for defining modal and polarization features of a VCSEL. In AlGaAs systems, emitting in the 850–980 nm spectral window, confinement comes from the oxidation of aluminum-rich layers. In the end, after MOCVD or MBE process, the structure with highly-doped layers needs low-resistance ohmic contacts. The top mirror is laterally etched down to the cavity and a mesa of diameter $\approx 25\,\mu$m is obtained. At this point, through selective lateral oxidation of an $Al_{>0.98}GaAs$ layer thick some tens of nanometers, an oxide aperture is realized [15–17]. Oxide aperture diameter is on the order of few micrometers, depending on the requirement on the modal emission. Size and shape strongly depend on the aluminum concentration level and on the vapor exposure time. Further details on the technological limitations resulting from this process will be discussed in the forthcoming chapters.

Emission wavelengths different from near-IR are reached by VCSELs growth with InP-, Sb- or nitride-based materials. Beside the additional challenges caused by these ternary and quaternary alloys, such as lattice matching to a GaAs substrate, thermal dissipation, and mirror thickness, the main concern is related to electrical and optical confinement. As a matter of fact, AlAs oxidation technique cannot be used

anymore, hence effective alternatives have been explored. Wafer fusion technique is a valid alternative in some cases, but it is a complex technique with limited yield and epitaxial growth steps on different wafers. A more robust technique relies on the introduction of a laterally structured buried tunnel junctions (BTJs) within the VCSEL structure. A TJ is a reverse-biased heavily-doped *pn* junction: a sketch of a TJ energy band diagram is reported in Fig. 1.3. Inside the TJ, diffusion current no more dominates carrier transport across the junction, whereas a strong tunneling current enabled by quantum direct band-to-band tunneling (BTBT) brings electrons from the valence to the conduction band, as indicated by the arrows of Fig. 1.3. This phenomenon was observed by Prof. Leo Esaki more than 60 years ago [18, 19], from which the concept of TJ was theorized and developed. Externally to the TJ, a blocking *pn* junction arises, only capable of sustaining a negligible saturation current. The transverse limitation of the BTJ is accomplished by selectively etching off the top side of the TJ outside the needed diameter exploiting highly accurate photolithographic process. This is followed by an epitaxial regrowth of moderately doped layers. The refractive index map provided in Fig. 1.4 helps to understand the geometry of a BTJ-VCSEL. Lithography requires additional intermediate steps during the VCSEL growth, as the solid source MBE should stop right after the TJ layers growth. Then, a photoresistive mask covers the TJ region to be defined, with radius ρ_{TJ}. The radial area outside ρ_{TJ} is etched away. Eventually, the MBE starts again; the epitaxial regrowth over the BTJ introduces a significant lateral refractive index step acting as a phase-shifting mesa. Such an inner relief propagates from the BTJ up to the semiconductor-air interface, and actually provides optical and electrical confinement that is different compared to the lithographic *pin* VCSEL proposed in [20]. Lithographic BTJ definition gives also the ability to reach smaller sizes that are hard to achieve with high reliability for oxide-confined VCSELs. In fact, the wet oxidation process that defines the oxide aperture size cannot be laterally controlled with high resolution [35–37]. This comes from the anisotropic oxidation speed that is strongly dependent on the spatially non-uniform Al molar concentration. As a consequence, apertures smaller than $2\,\mu$m for very small-volume fast devices result critical from a technological standpoint, unless slow and expensive accurate calibration and in-situ monitoring are implemented [38]. The demonstration of AlGaAs BTJ-VCSELs with good scaling properties could be an relevant step toward producing ultra-small size laser diodes with good size control, manufacturability and high die yield [21]. This will be an important research path for our future works.

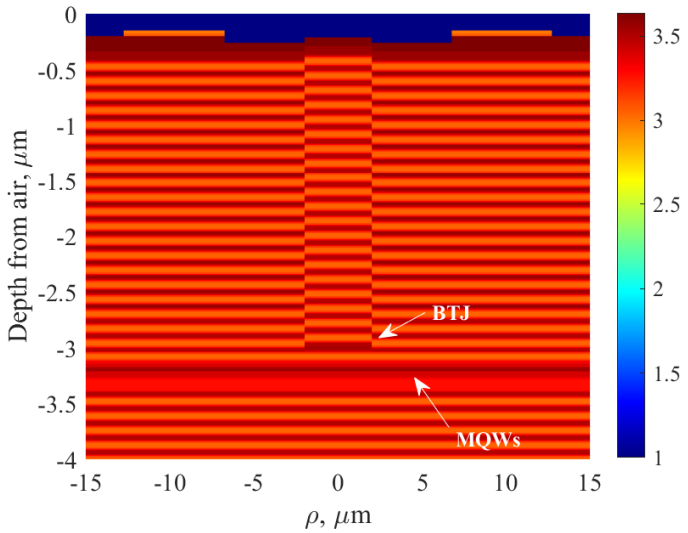

Fig. 1.4 Refractive index profile of the BTJ-VCSEL, from the opmost bottom DBR layers (in shades of orange and red) to the output facet. The three dark stripes in the AR denote the QWs; the TJ has an Al molar fraction close to the DBR. Optical and electrical confinement come from the inner index step induced by the MBE process above the photolithographically defined BTJ.

For the aforementioned reasons, TJs are technological enablers for long wavelength VCSELs, allowing to achieve electrical confinement by placing them just above the cavity region. Successful examples are InGaAlAs/InP VCSELs lasing at 1.55 μm [22–24] and, in the mid-IR spectral region, GaSb-based VCSELs lasing up to 4 μm [25–27].

On the other hand, in the thesis we deal with oxide-confined TJ-VCSELs, where optical confinement comes from the refractive index step introduced by a thin aluminum oxide layer. A planar TJ provides an effective hole injection mechanism into the active layers [29, 30]. Hence, TJs are exploited to convert the top DBR doping type from p to n. The conduction type inversion authorizes also to replace the p-type ohmic contact with a n-type one. As a result, only few tens of nanometers inside the TJ p^{++} side remain. Additionally, the high doping levels of the TJ impose to place it in a node of the optical standing wave (SW) to limit the free-carrier absorption (FCA) losses induced by the re-absorption of the emitted photons [28]. A further discussion on this point is proposed in Section 4.1 of Chapter 4. The removal of most of the p-type layers has a straightforward advantage in UV emitting GaN/AlGaN LEDs and VCSELs, where huge acceptor ionization energies

coupled to very poor hole transport properties prevent efficient hole injection [31–34]. In more conventional structures, the top DBR shows a reduction of FCA losses and electrical resistivity when *n*-doping replaces *p*-doping. These are related to a lower absorption coefficient and to a higher carrier mobility caused by a smaller effective mass, respectively. The established presence of TJs in both lower and higher bandgap material systems makes them credible candidates also for near-IR VCSELs, to improve their performances in terms of self-heating and device reliability. Our hypothesis is that the advantages brought by the TJ in the mentioned VCSELs still hold in AlGaAs/GaAs devices.

The demonstration of AlGaAs/GaAs oxide-confined VCSELs with TJs dates back to the early 2000s, proposed by Prof. Ebeling's group [39–42]. The main focus was directed towards the increase of the quantum efficiency, in order to enhance the gain given by the cavity and reach significantly larger optical powers. This was realized by inserting more active stages whose carriers were "recycled" by means of in-cavity planar TJs. Confinement was still demanded to the oxide apertures. The increasing amount of output power required by automotive applications is driving the market of multi-juntion (MJ) VCSELs toward maturity for LiDAR applications [43–45]. The idea of replacing a *p*-DBR with a *n*-DBR was first suggested by Lott's group in a 980 nm VCSEL [46]. As in the Ebeling's works, the TJ was not yet laterally structured. In fact, while TJs provide an enhancement of VCSELs static and dynamic performances, the requirement of smaller apertures and the related technological issues are more recent concerns. Besides, the inclusion of a TJ complicates the conventional VCSEL epitaxial growth. Nevertheless, TJs have been demonstrated to work properly in different material systems and in various applications. In 2017, Wong demonstrated a 850 nm TJ-VCSEL [47], showing that TJ-VCSELs can represent a viable alternative to the established confinement scheme.

As previously mentioned, 850–980 nm AlGaAs/GaAs VCSELs are widespread in short communication links for data-centres and high-performance computers, thanks to their high modulation speed and an optimal coupling with optical fibers. Staying on these wavelengths, VCSELs with integrated photodiodes (ViP) in the rear of their package can be used as light sources for self-mixing interferometry (SMI) [48], that is capable of velocity measurements by extracting the Doppler shift induced by motion [49–51] or to realize Chaotic LiDAR systems [52]. Interesting is their inclusion in PC mice to increase accuracy, acceleration and surface compatibility of these devices, that represented the first mass application of single-mode 850 nm VCSELs [53]. In

the evolving consumer electronics market, infra-red (IR) illumination provided by VCSELs finds specific applications in 3D sensing (gesture recognition) and 3D image capture [54]. More recent is the development of patents from Apple for their TrueDepth Cameras that from iPhone X uses VCSEL arrays for Face ID 3D sensing [55]. Single-mode near-IR VCSELs are also used as compact and efficient, low-cost sources in optically pumped miniature atomic clocks where the emission lines of an RF modulated single-mode VCSEL interact with atomic transitions in the atomic vapor (852 and 895 nm for Cs or 780 or 795 nm for Rb) [9, 56]. In a similar wavelength window, VCSELs are used for O_2 sensing through wavelength modulation spectroscopy. Mid-IR VCSELs are diffused in gas sensing, in particular of CO, CO_2, NO_2, CH_4 presenting strong absorption lines between 1.7 and 4 μm [57–59], thanks to their linearly polarized quasi-Gaussian transverse mode pattern and wavelength tunability [60, 61]. All the sensor-related applications benefit from the low power consumption, noise and superior beam quality of VCSELs.

The introduction of AlGaAs TJ-VCSELs on the market would imply a change of paradigm for state-of-the-art VCSELs in the 850–980 nm spectral region. Hence, the role of a reliable TCAD approach becomes pivotal. Some examples come from Streiff *et al.* [62] and Mehta *et al.* [63]. Commercial tools like PICS3D [64] or LaserMOD [65] coupled to *Sentaurus Device* by Synopsis are available, but they have limitations. In addition, it is not possible to have the complete control on the working flow of the solvers, that is vital for understanding in depth the operation of a VCSEL, not to mention that TJ modeling requires a genuine quantum approach, not available in commercial codes.

The thesis is focused on the development and expansion of an in-house solver capable of grasping the operation details of standard oxide-confined *pin* and TJ-VCSELs [66, 67]. The work is structured as follows. Chapter 2 is devoted to the description of our in-house models adopted to investigate this class of semiconductor lasers, with a particular emphasis on the multiscale and multiphysics nature of the involved problems. Chapter 3 deals with the calibration of a in-house 1D solver (D1ANA) over a reference *pin* VCSEL. Then, the same tool is used in Chapter 4 as a test-bed to move our first steps towards the implementation of a novel scheme to investigate TJ-VCSELs, that involves a coupling between a nonequilibrium Green's function (NEGF) treatment of the TJ with the semiclassical electrical solver. In Chapter 5 we finally extend the original 3D solver (VENUS) with the NEGF results. The performances of two test oxide-confined TJ-VCSELs are compared to the

reference *pin* VCSEL, showing the possibility of overcoming the state-of-the-art devices. A preferred design is determined, and different heat sink temperatures are investigated. The typical static VCSEL figures of merits are assessed, including the light-current-voltage (*LIV*) characteristics and the inner temperature variation together with the wavelength red shift.

Chapter 2

Multiscale and multiphysics VCSELs modeling: VENUS and D1ANA

As mentioned in the previous chapter, a paradigm shift for the established datacom VCSEL market should be led by a reliable TCAD approach on the new design concepts, rather than extended prototyping campaigns. The complete modeling of VCSELs is a non-trivial task, as the electrical, optical and thermal problems are strongly interconnected and all play a crucial role in determining the laser performance. Compact models are suited to interpret qualitatively the measurement results, but fail when it comes to provide manufacturing guidelines. A notorious example is represented by the rate equations model, a well-established system of equations capable of extracting and describing the operations of VCSELs. Rate equations model can be extended to perform increasingly sophisticated analysis, but they will still lack of quantitative predictivity.

A leap in the near-IR VCSEL market must be supported by tools capable of extract the main figures of merits starting from a layer-by-layer description of the structure details under investigation. Physics-based modeling has the ambitious target of quantitatively predicting the behaviour of a device. Additionally, it provides a direct access to inner quantities that are extremely important to comprehend thoroughly the VCSEL working principles. The interplay of various effects impose that a physics-based solver for VCSELs must deal simultaneously with carrier transport, optical mode evaluation and the heating effects, in a multiphysics framework. Furthermore, in lasers the coherence emission of photons comes from nanostructured

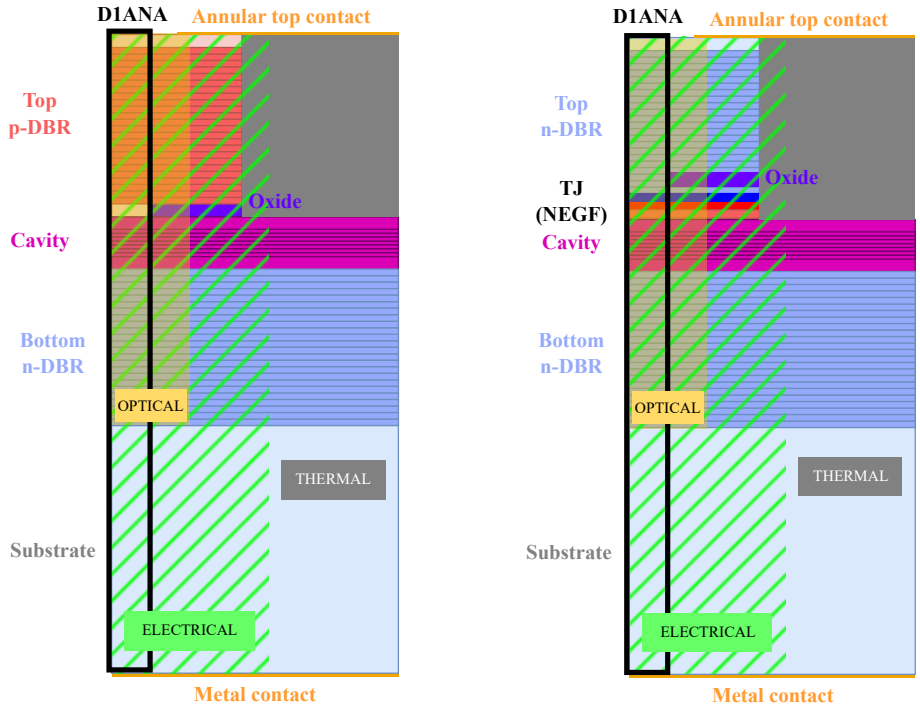

(a) *Pin* VCSEL (b) TJ-VCSEL

Fig. 2.1 VENUS simulation domains superimposed to the oxide-confined *pin* (**a**) and TJ (**b**) VCSEL 2D schematics. Thermal solver is applied on the whole device. The DD model (green hatched lines) is radially limited to a slightly larger portion beyond the mesa. The optical solver (yellow shaded area) accounts for the region above the substrate; radially, it includes the oxide aperture and a portion of the top annular contact. D1ANA acts on the central 1D "cut" denoted by the black rectangles. The oxide is not simulated and the top contact is vertically aligned to the aperture. NEGF simulates only the TJ layers.

ARs, such as stacked multi-QWs (MQWs), modeled by quantum models that can be coupled to the semiclassical ones. A multiscale approach cannot be avoided to fully understand VCSELs operation. To this aim, our group has developed the comprehensive 3D VCSEL electro-opto-thermal numerical simulator VENUS (Vcsel Electro-optho-thermal NUmerical Simulator) [66–68]. The schematics of the axisymmetric structures (oxide-confined TJ and *pin* VCSELs) investigated with VENUS are reported in Fig. 2.1, together with the domains over which the corresponding problems are solved. The dimension of each subdomain is related to the computational resources optimization, and will be discussed in the following sections. From VENUS, we develop a 1D version of the solver (D1ANA [69, 70]), meaning that all the electrical, thermal and optical problems reduce to one-dimensional, leading to much faster simulations. The approximation of the 3D features requires a calibration process of D1ANA, that simulates just a central 1D cut (represented in Fig. 2.1 as thin 2D rectangles) of the VCSEL. This is done on a reference *pin* VCSEL, starting from the same operation parameters used in VENUS. The details of the calibration process are reported in [70] and discussed in Section 3.1. At the end of this work, we have at disposal two tools capable of predicting at different levels of accuracy and computational burden oxide-confined *pin* and TJ-VCSELs operations.

The most relevant modification to VENUS and D1ANA presented across the thesis is the possibility of simulating TJ-VCSELs. In fact, the modeling of TJs cannot be carried out within a semiclassical picture, as the main transport mechanism across a TJ is the purely quantum mechanical phenomenon of band-to-band tunneling. Classically, BTBT across potential barriers is not allowed. Nevertheless, such a mechanism is able to bring a remarkable amount of charges from one side to the other one of the junction, building up a significant current. Some insights on how the TJ is simulated in our solvers are provided in Section 2.1.2.

2.1 Multiphysics approach

A comprehensive model of VCSELs should account for transport of carriers across the nanostrucutured AR and the DBRs, electromagnetic computation of the optical modes, absorption/gain of the material, and thermal effects. The model details have been discussed in depth elsewhere [66]: only the most important ones are addressed

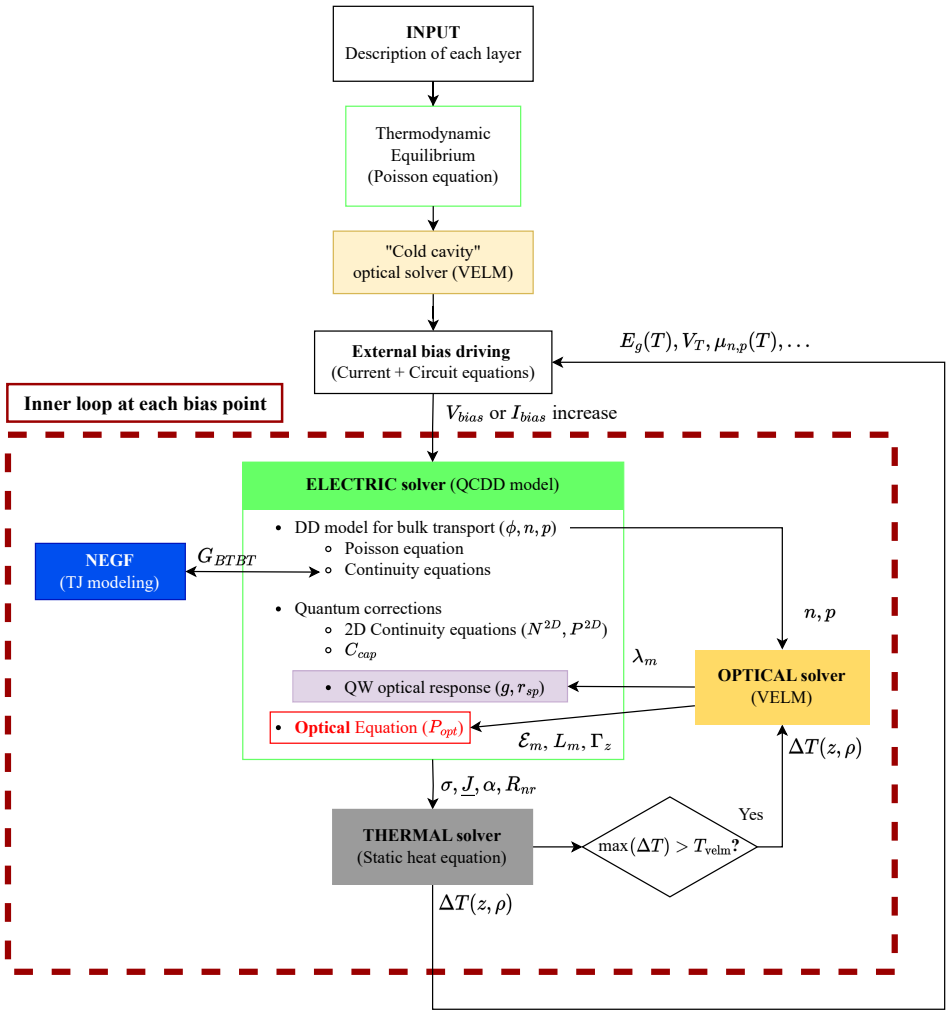

Fig. 2.2 Simulations flow chart of VENUS and D1ANA. The three blocks at the top define the structure and solve the electrical and optical problem at equilibrium. The blocks included in the big dashed rectangle represent the inner loop performed at each bias point, imposed by the external circuit. Green block: QCDD model, including electrical transport, quantum corrections (purple block) and optical rate equation (in red). In case of TJ-VCSEL, this is connected to the NEGF simulation (in blue) through the tunneling rate. Once the QCDD converges within the Newton's scheme, the heat sources are computed and taken as inputs of the thermal solver (gray block). If the temperature increase is larger that the control parameter T_{velm}, VELM (yellow block) is run again to extract the optical modal features.

in the sections below, with emphasis on the coupling terms that account for the complex interplay between the multiphysical aspects of the problem.

Schematically, VENUS and D1ANA are based on an identical flow chart, sketched in Fig. 2.2. The initial step consists in defining every layer of the VCSEL. Each layer has its thickness, radial extension, doping level and molar fraction (in case of alloys). These data represent the geometrical and material input of our in-house solvers. A fundamental assumption is the steady-state condition, that greatly simplifies the models implemented in our solvers. The relevant results are represented by the static electrical and optical characteristics (*LIV*); additionally, the adopted physics-based approach allows to grasp the VCSEL operation details by taking a look to the inner quantities, including the wavelength shift as a function of current and temperature, or the energy band diagram and the carrier densities.

2.1.1 Quantum-Corrected Drift-Diffusion model

In our solvers, carrier transport problem is solved by means of the semiclassical drift-diffusion (DD) model [71–75], alongside a set of quantum corrections introduced according to [62, 76, 77]. These are crucial for a DD solver dealing with nanostructured devices, as a correct QW modeling is of utmost importance to extract the stimulated emission process that dominates any laser operation. Hence, a physics-based framework represents a good compromise between the phenomenological rate equations model and more computationally demanding quantum approaches [78, 79]. Our static (no time derivatives) quantum-corrected drift-diffusion (QCDD) model is based on the following system of five equations, where two sets of populations (bulk, 3D and bound, 2D) are treated:

$$-\nabla^2\phi = \frac{q}{\varepsilon}\left(p^{3\mathrm{D}} - n^{3\mathrm{D}} + P^{2\mathrm{D}} - N^{2\mathrm{D}} + N_{\mathrm{D}}^{+} - N_{\mathrm{A}}^{-}\right) \tag{2.1}$$

$$\frac{1}{q}\nabla J_{n^{3\mathrm{D}}} = U_{\mathrm{SRH},n}^{3\mathrm{D}} + U_{\mathrm{sp},n}^{3\mathrm{D}} + U_{\mathrm{Aug},n}^{3\mathrm{D}} + U_{\mathrm{BTBT},p} + C_{\mathrm{cap},n} \tag{2.2}$$

$$-\frac{1}{q}\nabla J_{p^{3\mathrm{D}}} = U_{\mathrm{SRH},p}^{3\mathrm{D}} + U_{\mathrm{sp},p}^{3\mathrm{D}} + U_{\mathrm{Aug},p}^{3\mathrm{D}} + U_{\mathrm{BTBT},p} + C_{\mathrm{cap},p} \tag{2.3}$$

$$\frac{1}{q}\nabla J_{N^{2\mathrm{D}}} = U_{\mathrm{SRH},n}^{2\mathrm{D}} + U_{\mathrm{sp},n}^{2\mathrm{D}} + U_{\mathrm{st}}^{2\mathrm{D}} + U_{\mathrm{Aug},n}^{2\mathrm{D}} - C_{\mathrm{cap},n} \tag{2.4}$$

$$-\frac{1}{q}\nabla J_{P^{2\mathrm{D}}} = U_{\mathrm{SRH},p}^{2\mathrm{D}} + U_{\mathrm{sp},p}^{2\mathrm{D}} + U_{\mathrm{st}}^{2\mathrm{D}} + U_{\mathrm{Aug},p}^{2\mathrm{D}} - C_{\mathrm{cap},p} \tag{2.5}$$

The conventional DD system (2.1)–(2.3) includes the Poisson equation (2.1) coupled to the carrier continuity equations (2.2)–(2.3), to model transport of bulk carriers (n^{3D} and p^{3D}) within a semiclassical picture. From (2.1), the electrostatic potential ϕ inside the structure is computed. The incomplete ionization of the impurity dopants is accounted by introducing the donor and acceptor activation energies ΔE_D, ΔE_A [80, 81], that return the ionized fractions of donor and acceptor concentrations N_D^+ and N_A^- (see Section A.2 of Appendix A). Bound carriers N^{2D} and P^{2D} are also included. In the same equation, q is the elementary charge and ε indicates the static dielectric permittivity. Electron and hole current densities in (2.2)–(2.3) are denoted by $J_{n,p^{3D}}$. The net generation/recombination (GR) rates U_{SRH}, U_{Aug}, and U_{sp}, describe Shockley-Read-Hall (SRH) recombination, Auger transitions, and radiative processes, respectively. The BTBT across the TJ is modeled by means of a U_{BTBT} rate extracted with a non-equilibrium Green's function (NEGF) approach. Details about the adopted procedure are provided in Section 2.1.2. All these processes model electron-hole pairs annihilation/creation. Further insights on the net recombination rates are presented in Appendix A, Section A.3.

Two additional 2D continuity equations (2.4)–(2.5) accounting for electrons and holes transverse current densities $J_{N,P^{2D}}$ extend the bulk DD system. The potential barriers introduced between each QW generate confinement along the longitudinal direction. Therefore, (2.4)–(2.5) have a reduced dimensionality with respect to (2.2)–(2.3), and the gradient acts only on the transverse coordinates. Eventually, an analogous set of GR rates U^{2D} (excluding the tunneling term) is introduced. Notice that the stimulated emission term U_{st}^{2D} connects the electrical transport model to the optical problem as described in Section 2.1.3. The key concept connecting bulk and bound populations is the capture/escape rate $C_{cap,n/p}$ at the QW nodes [82–85]:

$$C_{cap,n} = \left[1 - \exp\left(\frac{E_{F,n}^{2D} - E_{F,n}^{3D}}{k_B T}\right)\right]\left(1 - \frac{N^{2D}}{N_2}\right)\frac{n^{3D}}{\tau_n^{cap}} \tag{2.6}$$

$$C_{cap,p} = \left[1 - \exp\left(\frac{E_{F,p}^{3D} - E_{F,p}^{2D}}{k_B T}\right)\right]\left(1 - \frac{P^{2D}}{P_2}\right)\frac{p^{3D}}{\tau_p^{cap}} \tag{2.7}$$

where $E_{F,n/p}^{2D}$, and $E_{F,n/p}^{3D}$ represent the bound and bulk quasi-Fermi levels, respectively. Temperature is denoted by T, while k_B is the Boltzmann constant. Depending on the sign of the square parentheses of (2.6)–(2.7), $C_{cap,n/p}$ is either a recombination term (positive) modeling bulk carriers captured by the QWs, or a generation term (nega-

tive), when QW carriers escape to the bulk region ($C_{\mathrm{esc},n/p}$). Notice that the terms in the second parentheses cannot go negative, as they contain the maximum densities N_2, P_2 admitted by each QW and determines its filling: the capture rates drop to zero in case of full QW. The capture lifetimes $\tau_{n/p}^{\mathrm{cap}}$ are phenomenological terms in the order of picoseconds connected to the probability of a carrier capture/escape by the QW, and can be used as fitting factors of the simulations. The results presented in Chapters 3 and 4 are obtained by taking $\tau_n^{\mathrm{cap}} = 10\,\mathrm{ps}$ and $\tau_p^{\mathrm{cap}} = 5\,\mathrm{ps}$. Furthermore, overall carrier balance is ensured by energy separation of the populations, together with the fact that $C_{\mathrm{cap},n/p}$ takes opposite sign in the 2D and 3D equation:

$$C_{\mathrm{cap},n/p}^{\mathrm{2D}} = -C_{\mathrm{cap},n/p}^{\mathrm{3D}} \cdot W_{\mathrm{QW}} \tag{2.8}$$

meaning that capture (recombination) from bulk results in a generation inside the QW, and viceversa. The conversion between bulk and bound capture requires the multiplication by the QW width W_{QW}. As any other GR rate of the presented QCDD model, at thermodynamic equilibrium the net capture rate is equal to zero.

The typical DD constitutive relations:

$$J_n = -q\mu_n n\nabla\phi + qD_n\nabla n \tag{2.9}$$

$$J_p = -q\mu_p p\nabla\phi - qD_p\nabla p \tag{2.10}$$

close the QCDD model by expressing the current densities in terms of the system unknowns, namely ϕ, n, p (both 2D and 3D). Electron and hole mobilities are denoted as $\mu_{n,p}$; the diffusion coefficients $D_{n,p}$ are related to $\mu_{n,p}$ by the Einstein's relation. The bound analogous of (2.9)–(2.10) have a reduced dimensionality with respect to bulk, and are not reported here. Notice that all the mentioned carrier populations are assumed to obey the Fermi-Dirac statistics (see Section A.1 of Appendix A) by introducing an additional term in the definition of potential. The static QCDD model reported in (2.1)–(2.5) and (2.9)–(2.10) is written in a generic 3D form. The axisymmetric structure of a VCSEL permits to simplify the implementation by introducing the cylindrical coordinates. In VENUS, this model is applied to the green hatched lined region of Fig. **??**, as radial current beyond that region is negligible. In D1ANA, a cartesian 1D version of the QCDD model is solved, such that Laplacian and gradient operators are reduced to derivatives along the longitudinal transport

direction z. An extended discussion about the 1D approximation is presented in Section 3.1.

Similarly to TJs, the QWs optical response cannot be computed within a semi-classical picture. Quantum corrections must be introduced to describe quantization effects in the QWs, and evaluate their gain/absorption features. The Schrödinger equation related to the QW problem is solved on a multiband $\mathbf{k} \cdot \mathbf{p}$ description of the electronic structure, under axial invariance assumption that leads to a 4-band formulation (heavy holes, light holes, split-off and electrons). In this way, the energy subbands and the corresponding wavefunctions are computed and plugged inside the QW description adopted in the DD model. The corresponding gain is obtained applying Fermi's golden rule (purple block in Fig. 2.2), where the electronic band structure is described with the Luttinger–Köhn Hamiltonian [86]. Gain g and spontaneous emission into the lasing mode r_{sp} depend on the 2D electron N^{2D} and hole P^{2D} densities, on the emission wavelength λ and on temperature [67, Fig. 8]. A wide set of configurations is simulated, with the results stored in a 4-D look-up table (LUT). The LUT is used to extrapolate g and r_{sp} at each applied bias step of the simulation.

After the geometry definition, the simulation begins with the thermodynamic equilibrium solution (see schematics in Fig. 2.2), from which quantities including energy band diagram, carrier populations, QW filling, are extracted by solving the Poisson equation (2.1). Then, the applied bias brings the system out of equilibrium (green blocks), and the full QCDD simulation computes the laser characteristics. The nonlinear nature of the system (2.1)–(2.5) requires the adoption of a numerical approach to reach a solution at each bias step. Implementation and resolution of the model are discussed in Section 2.2.

2.1.2 NEGF-DD framework: tunnel junction treatment

Carrier transport in TJs is dominated by purely quantum mechanical tunneling. The nature of the phenomenon does not allow the semiclassical treatment described in the previous section. The simplest model dealing with quantum tunneling mechanisms is based on the Wentzel-Kramers-Brillouin (WKB) theory [87], which evaluates bound-state energies and tunneling rates through a potential barrier. The basic idea behind WKB theory is to avoid the application of the perturbation theory to reach a solution of the one-dimensional time independent Schrödinger equation. This is possible

within the assumption of a particle moving in a *slowly varying* potential. In a TJ, the energies available for quantum tunneling span from the valence band edge energy at the *p*-side to the conduction band edge energy at the *n*-side. Such energies can be used to identify the *classical turning points* needed for the WKB approximation, that returns the Fowler-Nordheim tunneling transmission expression [88, 89]. Following WKB theory, Kane proposed different local tunneling models [90, 91], that suffer of serious limitations [92, 93]. Even the Hurkx's model [94–96], specifically developed for reversely-biased junctions and exploited in commercial software like *Sentaurus Device* by Synopsys [97], heavily underestimates the tunneling current in AlGaAs systems due to the saturation of the net generation rate [98]. Approaches more adherent to the actual physics of BTBT are the *non-local* tunneling models [99, 100], where carriers do not "disappear" from one point to appear in another, but an actual carrier transport across the forbidden band is computed. An example is the one implemented in *Sentaurus Device* [97], that relies on a huge amount of fitting parameters, strongly affecting the predictivity of the model. As TJs are of prime importance also in III-V multijunction solar cells, some models have also been implemented to compute the tunneling peak current in the forward bias window $0-0.3\,\mathrm{V}$ [101, 102], relying on the Tsu-Esaki formula [103].

During the non-local BTBT, electrons tunnel across the forbidden band, from the valence band (VB) on the *p*-side of the TJ and reappearing in the conduction band (CB) on the *n*-side side (see sketch in Fig. 2.3a). The nature of the phenomenon requires a genuine quantum mechanical treatment, also accounting for its non-local nature. Together with the MQW region, the presence of TJ leads to a *multiscale* problem, where the semiclassical DD picture assumes local quasi-equilibrium condition and the tunneling region is treated through quantum corrections. In contrast to non-self-consistent quantum models of tunneling, where tunneling probabilities are evaluated from the Schrödinger's equation with frozen potential profiles and closed boundary conditions, here we propose a self-consistent solution of nonequilibrium Green's function (NEGF) and QCDD models. The bridging is realized by introducing an additional net recombination rate U_{BTBT} inside the bulk continuity equations (2.2)–(2.3) right hand sides (blue block in Fig. 2.2). In practice, we propose a DD simulation of the whole VCSEL structure, quantum-corrected with a NEGF-derived GR rate to describe the tunneling current. The NEGF current can be restricted to just the interband tunneling component by integrating the spectral current density in an appropriate energy range, while the classical intraband component is still computed

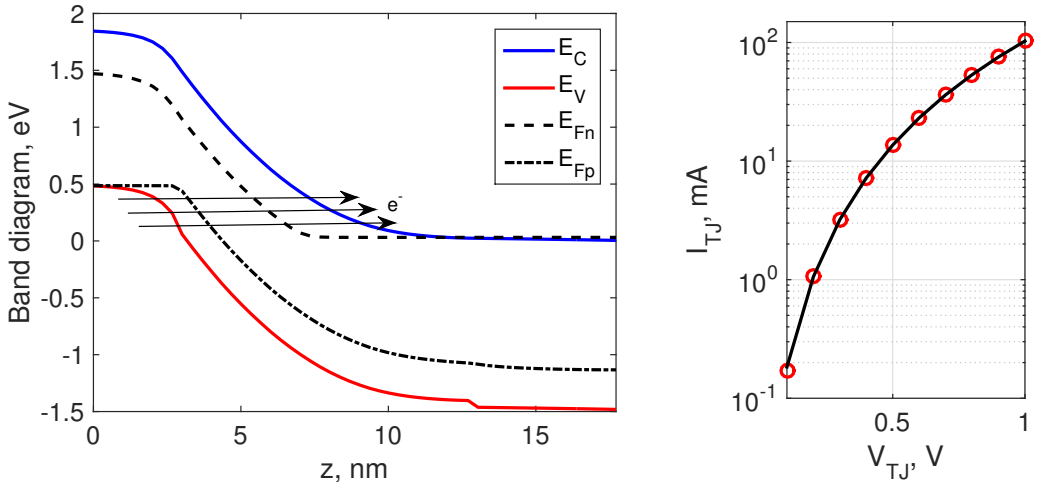

(a) (b)

Fig. 2.3 TJ modeling. (**a**): band diagram of the TJ at $V_{\mathrm{TJ}} = 0.5$ V. Black arrows indicate the tunneling path of electrons from the valence band of the p^{++} side to the conduction band of the n^{++} side. (**b**): current computed from NEGF (red circles) and corresponding high-order fit (black solid line), as a function of V_{TJ}.

by the DD approach. The spectral current density is an energy- and position-resolved current density extracted from NEGF, useful to study how carriers propagate in the investigated device. In the TJ case, it determines where tunneling occurs and the tunneling current magnitude.

NEGF framework is based on a multiband $\mathbf{k} \cdot \mathbf{p}$ description similar to the one used to compute the QW bound states described in the previous section, where the semiempirical Luttinger parameters listed in [104] are adopted. The steady-state Keldysh and Dyson equations are iteratively solved in the NEGF space-energy window with the Hartree potential obtained from the DD band diagram. A finite-element discretization leads to a coupled set of equations that are parametrically dependent on the transverse wave vector and the energy. Upon convergence of the self-consistent Born approximation (SCBA) iterative scheme, when Green's functions and fully non-local scattering self-energies are self-consistent, the divergence of the spectral current integrated over the whole energy range should be zero, the SCBA being current-conserving [98]. Restricting the energy integral to the conduction or valence bands gives, in the absence of interband scattering mechanisms, the BTBT (net)

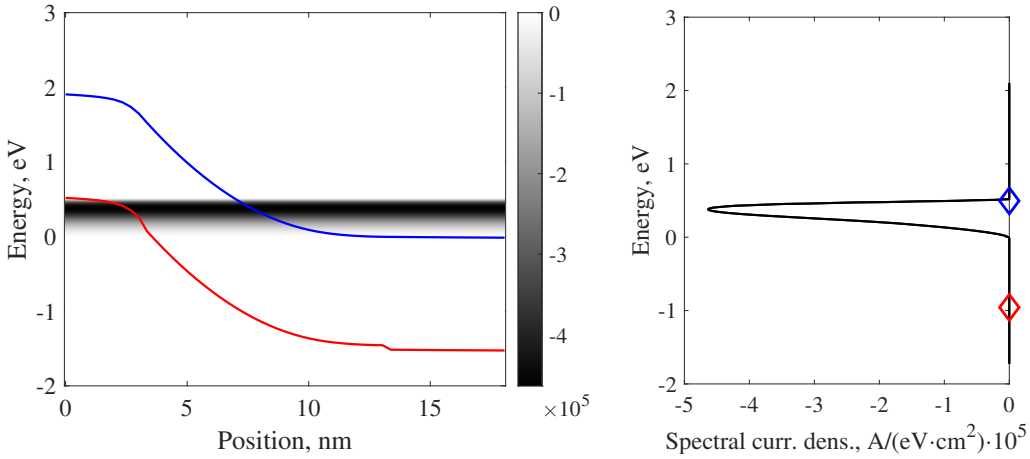

(a) Spectral current in the NEGF simulation window (b) Spectral current cut at 7 nm

Fig. 2.4 (**a**): electron spectral current density (in black) as a function of energy and position across the TJ, at $V_{\mathrm{TJ}} = 0.5$ V, superimposed to the TJ energy band diagram (red: VB, blue: CB). The bar code scale expresses the spectral current magnitude in terms of A/(eV·cm^2). (**b**): spectral current cut at 7 nm vs. energy. Diamonds represent CB and VB edges at that position.

recombination rate U_{BTBT}, that turns out to be a generation rate G_{BTBT}, is:

$$G_{\mathrm{BTBT}}(V_{\mathrm{TJ}}) = \frac{1}{q}\frac{J_{\mathrm{TJ}}(V_{\mathrm{TJ}})}{L_{\mathrm{TJ}}} \tag{2.11}$$

where q is again the elementary charge, $J_{\mathrm{TJ}}(V_{\mathrm{TJ}})$ is the current density computed by integrating the NEGF spectral current flowing across the TJ as a function of the voltage drop V_{TJ} across it (simply V hereinafter) and L_{TJ} is the TJ length along the longitudinal axis. For a classification of conduction and valence states within a multiband model of the electronic structure, we refer to [98]. In the spirit of a multiscale simulation, the calculation of the Green's functions is limited to the tunneling region. In fact, the high doping levels impose that the quasi-Fermi levels associated with the majority carriers are pinned on both sides of the TJ. As a consequence, well defined Fermi levels for the calculation of the boundary self-energies are available (see black dotted lines in Fig. 2.3a).

In Fig. 2.4a, the electron spectral current density at 0.5 V along the TJ is reported in black. Notice that it is energetically peaked where the tunneling path is shorter. By taking a cut at 7 nm of it, Fig. 2.4b is obtained: tunneling current is sustained only in the energy window between 0 and 0.5 eV, where CB and VB are overlooking.

In addition, the density current of Fig. 2.4a remains longitudinally constant for each energy value due to the ballistic assumption, *i.e.*, no scattering event redistributes the carrier energy, hence conserving it from one contact to the other. This is a reasonable assumption as in direct bandgap semiconductors symmetry arguments suggest that electron-phonon coupling is inefficient across the TJ [105]. In the specific case of an AlGaAs TJ with small Al concentrations considered here, the two processes (coherent interband tunneling and phonon interaction) are sequential rather than simultaneous, and so, strictly speaking, the tunneling process is mainly a coherent process (i.e., phononless) [98]. Trap-assisted tunneling (TAT) is not included in the simulation, as the presence of defects is not expected to reduce the relatively short tunneling path induced by the large band bending under strong reverse bias.

For computational efficiency, it is convenient to pre-compute $G_{\mathrm{BTBT}}(V)$ for different values of the voltage drop across the TJ, so as to fit the $I(V)$ characteristics of the TJ and then extrapolate the needed value for the DD simulation. A high-order exponential fit provides a good overlap with the computed NEGF current vs. voltage (see Fig. 2.3b), also at low bias where convergence of the Newton's scheme is more critical:

$$J_{\mathrm{TJ}}(V) = 10^{\left(\beta_0+\beta_1 V+\beta_2 V^2+\beta_3 V^3+\ldots\right)} \tag{2.12}$$

with β_i coefficient of the exponential fit. The resulting analytical expression is plugged in (2.11) and can be easily derived with respect to the bulk drift-diffusion unknowns (*i.e.*, ϕ, n^{3D}, p^{3D}), providing the derivatives to be inserted in the *Jacobian* matrix employed in the Newton algorithm described in Section 2.2. Additional details on the implementation of the NEGF-DD scheme are proposed in the Appendix B. This procedure has been first validated in [98], where experimental data on a test structure designed and characterized by Chalmers University have been reproduced by our NEGF-DD approach.

To provide further insights of the results coming from a NEGF simulation, let's comment on some of the output quantities that are extracted at $V = 0.5$ V. NEGF is here applied to the 18 nm TJ included in the TJ-VCSELs diffusely described in Section 4.1. In Fig. 2.5a–2.5b, the carrier spectral distribution along the TJ are reported. These are compatible to the semiclassical charge densities obtained in a DD simulation, with the difference of being energetically-resolved other than spatially. This means that an integration over energy would be necessary to compare the quantities. The fringes arising in both figures are consequence of the interference

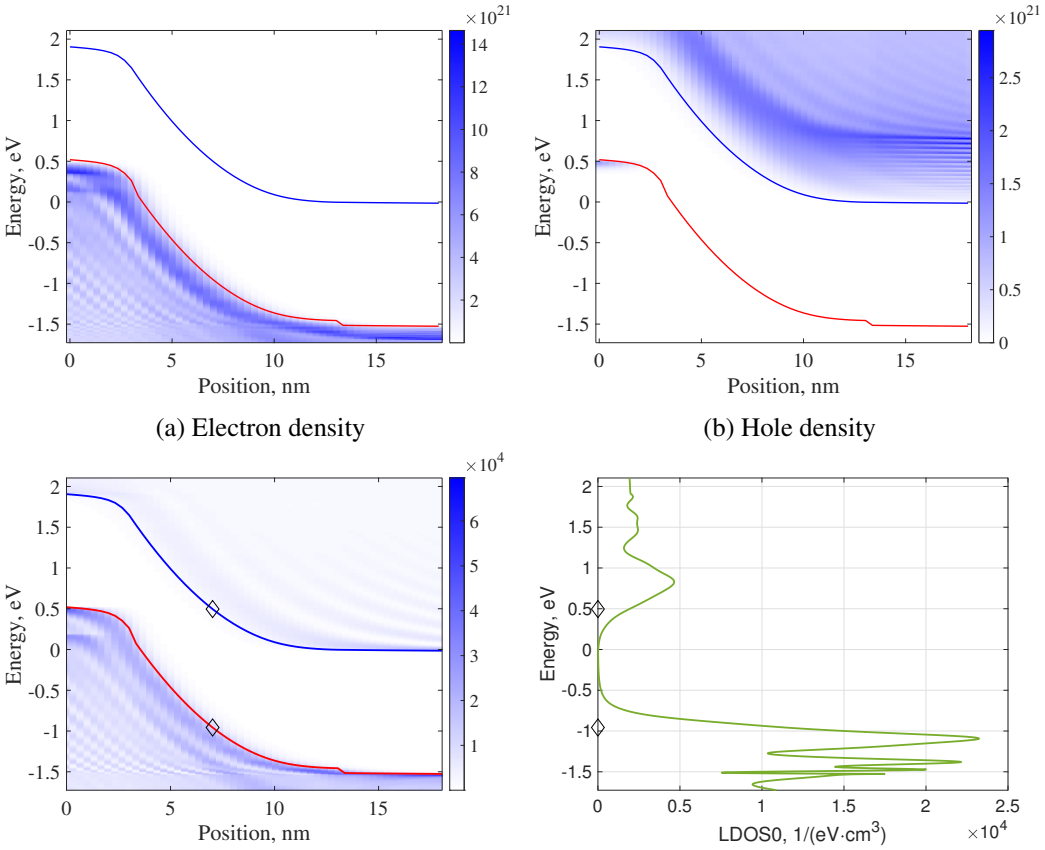

(a) Electron density

(b) Hole density

(c) LDOS0 at $k_{\parallel} = 0$

(d) LDOS0 cut at $z = 7$ nm

Fig. 2.5 Spectral distribution along the TJ of electron (**a**) and hole (**b**) densities, at $V_{\mathrm{TJ}} = 0.5$ V. (**c**) Local density of states in the ballistic limit. (**d**) Cut of the LDOS made at 7 nm, whose corresponding VB and CB edges are denoted by the black rhombuses. All these quantities, including the bar code scales, are expressed in 1/(eV·cm^3).

pattern induced by the injected wave functions at the contacts, that are partially reflected at the junction. Another direct result of NEGF is the spectral resolved local density of states (LDOS), terms of 1/(eV·cm^3). For sake of clarity, in Fig. 2.5c the LDOS is shown without the contribution of transverse wavevector ($k_{||} = 0$). The interference oscillations decreasing when approaching the continuum region are more clear from the cut of the same LDOS at 7 nm, reported in Fig. 2.5d.

2.1.3 Optical solver: VELM

Alongside the system (2.1)–(2.5), a set of photon rate equations is introduced to couple electrical and optical problems and treat lasing operation [66, 67]:

$$\frac{\partial P_{\mathrm{st},m}}{\partial t} = \Gamma_z \left(G_m - L_m\right) P_{\mathrm{st},m} + \Gamma_z S_m, \qquad m = 1, \ldots, N_{\mathrm{modes}} \tag{2.13}$$

Each equation expresses the steady-state photon balance between the modal gain G_m and the modal losses L_m, in the presence of a spontaneous emission rate S_m into the lasing mode m. Γ_z is the longitudinal optical confinement factor [106, 9]. The result from (2.13) is the output modal optical power $P_{\mathrm{st},m}$ (red block of Fig. 2.2). As the QCDD system, these are static equations, meaning that the time derivative of the stimulated modal power at the VCSEL output is equal to zero ($\partial P_{\mathrm{st},m}/\partial t = 0$).

All the parameters entering (2.13) are extracted with our in-house electromagnetic vectorial simulator VELM developed by Dr. P. Debernardi [107, 108], both in its three- and one-dimensional forms (normal incidence assumption [61]). VELM evaluates the optical modes by expanding the electromagnetic field $E(\rho, \phi, z)$ in terms of the complete basis of modes ν (including forward and backward propagation, field polarization and azimuthal variations [66]) of a reference medium in cylindrical coordinates $E_\nu(\rho, \phi)$, expressed in terms of Bessel functions of the first kind [109] as:

$$E(\rho, \phi, z) = \sum_{\nu'} dk A_{\nu'}(z) E_{\nu'}(\rho, \phi) \simeq \sum_{\nu} A_\nu(z) \Delta k E_\nu(\rho, \phi) \tag{2.14}$$

thus avoiding to impose the transverse boundary conditions explicitly. Δk comes from the approximation of the integral over the continuous radial component of the wave vector k into a discrete finite sum of terms, and A_ν is the amplitude of the mode ν. Longitudinal and transverse variations with respect to reference are treated by

coupled-mode theory, whose equation:

$$\frac{d\mathbf{A}}{dz} = (\mathbf{B} + K_{\nu\nu'}\Delta k)\,\mathbf{A} \tag{2.15}$$

relates the unknown mode amplitude vector $\mathbf{A} = \{A_\nu\}$ to those of the previous layers. $\mathbf{B}$ =diag$\{j\beta_\nu\}$ describes the free propagation in the reference material with propagation constant β_ν and K_ν describes the modes coupling as transverse integrals of Bessel functions. The modes amplitude in the $(i+1)^{th}$ layer coming from the solution of (2.15) layer can be expressed in an exponential matrix form:

$$\mathbf{A}_{i+1} = e^{(\mathbf{B}+K_i)z_i}\mathbf{A}_i = M_i\mathbf{A}_i \tag{2.16}$$

where M_i is a generalized transmission matrix of the layer z_i. To ensure the resonance condition of a supported mode in a semiconductor resonator, the expansion coefficients of waves propagating in forward and backward directions, perpendicular to the layers, need to replicate after a full round-trip. This condition is expressed using a generalized transfer-matrix approach and transformed into an ordinary eigenvalue problem, by linearizing the transmission matrix related to the AR layer (M_{act}) in terms of the unknown threshold gains, directly related to the eigenvalues. Their real and imaginary parts represent the resonance wavelengths λ_m and modal losses L_m, respectively. The eigenvectors correspond to the field expansion coefficients, and are used to calculate the optical modal field $\mathscr{E}_m(z,\rho)$ throughout the VCSEL. Other modal parameters, such as the far field angles and outcoupling efficiencies, are extracted to obtain a complete set of data useful to fully characterize VCSELs operation.

The modal wavelengths are used to extrapolate the corresponding QW gain $g(N^{2D},P^{2D},\lambda_m,T)$ and spontaneous emission rates $r_{\text{sp}}(N^{2D},P^{2D},\lambda_m,T)$ from the precomputed LUT mentioned in Section 2.1.1, as highlighted from the purple block in Fig. 2.2. The modal gain G_m comes from the overlap of $g(N^{2D},P^{2D},\lambda_m,T)$ with the optical field intensity radial profile taken at the QW node $\mathscr{E}_m(\rho)$:

$$G_m = \int_0^{2\pi}\int_0^{\rho_{\max}} g(N^{2D},P^{2D},\lambda_m,T)\,|\mathscr{E}_m(\rho)|^2\,\rho\,d\rho\,d\phi \tag{2.17}$$

where the radius $\rho_{\max}$ identifies the radial extension of the electrical domain. In a similar fashion the spontaneous emission rate S_m is computed by substituting g with

r_{sp} in (2.17). Eventually, gain and modal field serve as bridges between electrical (2.4)–(2.5) and optical (2.13) problems, which is realized through the stimulated emission rate $U_{\mathrm{st}}^{\mathrm{2D}}$, computed as [**?** 66]:

$$U_{\mathrm{st}}^{\mathrm{2D}} = R_{\mathrm{st},m} = \frac{g(N^{\mathrm{2D}}, P^{\mathrm{2D}}, \lambda_m, T)\,|\mathscr{E}_m(\rho)|^2}{\int_0^{2\pi}\int_0^{\rho_{\max}} |\mathscr{E}_{\mathrm{out},m}(\rho)|^2 \rho\, d\rho\, d\phi}\, \frac{P_{\mathrm{st},m}}{\hbar\omega_m} W_{\mathrm{QW}} \tag{2.18}$$

where $\mathscr{E}_m(\rho)$ is the aforementioned m-th modal field at the QW and $\mathscr{E}_{\mathrm{out},m}(\rho)$ the field at VCSEL output section. In practice, the unknown $P_{\mathrm{st},m}$ is converted into a recombination term entering the bound continuity equations.

Notice that in D1ANA, the 1D version of VELM works within a single-mode approximation. Higher order radial and azimuthal modes are neglected. Indeed, in VENUS a larger number of modes (depending on the radial size of oxide aperture and top metal ring) is taken into account, such that losses and emission wavelength of each one is extracted by VELM to provide a more accurate picture. Polarization is not investigated in this thesis, so VELM simulations are executed in its linearly polarized (LP) scalar approximation, without losing any relevant information for the VCSELs taken into account [107]. Notice that the fully vectorial version of VELM is capable of dealing with any kind of anisotropy, caused by material, geometry or gratings (including high-contrast gratings [110]). This makes VELM an instrument much more versatile than the QCDD solver, that is limited to axisymmetric structures, that anyway cover the majority of commercial VCSELs.

As a final remark, let's point out that VELM is not run at each bias point of VENUS and D1ANA simulations. As schematized in the yellow block in Fig. 2.2, VELM accepts as inputs from the DD solver the carrier densities and from the heat equation the VCSEL inner temperature map, needed to assess FCA and refractive index variations induced by charges and temperature. Below optical threshold, none of them changes significantly with respect to equilibrium. Therefore, we introduce a control parameter called T_{velm}, that checks if the maximum temperature variation coming from (2.19) is large enough to provoke relevant modifications in the VELM outputs. This is done in the perspective of enhancing the solver speed, without compromising the optical characteristics. In our simulations, we impose $T_{\mathrm{velm}} = 2^{\circ}\mathrm{C}$, large enough to avoid redundant VELM calls, in particular below threshold.

2.1.4 Thermal solver

A comprehensive VCSEL simulator must account for the self-heating effects, as they massively impact on the laser performance. As a matter of fact, the vast majority of AlGaAs material parameters are strongly temperature dependent, among which the most noticeable are the energy gap (according to Varshni model, [111]), the electrical mobility (Hilsum model, [112]) and the free-carrier absorption (Drude formula, [113, 114]). Furthermore, the rise of inner temperature induces the drop and quenching of optical gain. Ultimately, heat gives a stronger weight to the non-radiative recombinations (in particular to Auger recombination [67, 115, 116]) over the radiative counterpart. A direct consequence of self-heating is that VCSELs undergo a thermal roll-over at high current injection conditions, causing the reduction of the output power slope vs current characteristics. Such a phenomenon is responsible of limiting VCSEL operation in harsh environments (e.g. server racks) where high temperatures are reached. Heat effects also impact VELM simulations, as temperature modifies the refractive index profile according to (3.1), that enters the modal competition through thermal guiding effect.

VCSEL self-heating is evaluated in VENUS and D1ANA by implementing a static heat transport equation solver (represented as a gray block in Fig. 2.2):

$$\nabla \cdot (\kappa \nabla T) = \sigma^{-1} \left| J_{n/p}^{3\mathrm{D}} \right|^2 + \alpha W_{\mathrm{opt}} + q(U_{\mathrm{SRH}} + U_{\mathrm{Aug}}) E_{\mathrm{g}} + q C_{\mathrm{cap}} \Delta_{C/V} \qquad (2.19)$$

where T is the temperature increase from the heat sink temperature. (2.19) is solved on each point of a mesh grid refined with respect to the QCDD one. κ denotes the spatial-dependent thermal conductivity. The right hand side of (2.19) accounts for all the internal heat sources. The electrical conductivity is denoted by σ, whose reciprocal (the resistivity computed by microscopic Ohm's law) multiplies the current density squared to estimate the Joule effect. The heating related to the FCA losses is extracted by weighting the absorption coefficient profile $\alpha(z,\rho)$, that depends on doping type and level, with the stimulated optical power P_{st} and the corresponding optical standing wave (SW), *i.e.*, the normalized electric field related to the longitudinal mode sustained by the resonator AR, and the radial field intensity $|\mathscr{E}(\rho)|^2$: $W_{\mathrm{opt}} = P_{\mathrm{st}} \cdot \mathrm{SW}(z) \cdot |\mathscr{E}(\rho)|^2$. Non-radiative transitions across the energy gap E_{g} of both bulk and active material layers are included; in a similar fashion, phonon-assisted processes induced by the carrier capture/escape from quantum

barriers with $\Delta_{C/V}$ height are computed [67]. All these quantities are estimated from the results retrieved by the QCDD problem solution.

A major criticality of (2.19) comes from the thermal conductivity, that greatly changes across a VCSEL. The values of κ used for the various VCSEL regions, *i.e.*, substrate, passivations, mirrors, AR, contacts and air, are listed in 3.1. An anisotropy factor of 0.8 is used to account for the reduced thermal conductivity in the longitudinal direction z [67]. Besides, κ also depends non-linearly on temperature, demanding self-consistency between them. In VENUS, accurate results in the most critical VCSEL region (the MQW layers and their closest neighbors) are crucial to compute figures of merits coherent with experimental data. The typical finite-element method (FEM) relying on linear basis functions in its Galërkin formulation is unsuited to attack the problem efficiently. In fact, despite the advantages of FEM, mesh refining results to be scarcely effective in improving the solution of (2.19), unless huge amount of nodes are adopted. A powerful alternative involves the definition of higher order basis functions (such as Legendre polynomials) to approximate properly the solution in each VCSEL subdomain, where κ is piecewise constant. The main challenge is the imposition of boundary conditions at each interface, that are enforced through mortar method [67]. Such a numerical scheme is called mortar element method MEM [66, 117, 118], and it basically relies on more complex basis functions instead of strong mesh refinements.

In D1ANA, the lack of radial features authorizes to adopt a simpler 1D FEM approach, with homogeneous Dirichlet's boundary condition enforced at the bottom contact, corresponding to the substrate interface with the heat sink. At the top contact side, we keep the Neumann boundary condition naturally imposed by FEM scheme on the heat equation. Self-consistency between T and κ is ensured. A less accurate temperature increase profile is predicted with respect to the MEM. This will be further discussed in Section 3.1.

2.2 Discretization and system resolution

The DD system (2.1)–(2.5), together with the photon rate equation (2.13), consists of a set of partial differential equations (PDEs) that should be solved self-consistently at each bias point. Mathematical solvers available for computers cannot solve directly PDEs using analytical methods. The only way to tackle them is through iterative

schemes, required to solve numerically the equations. Furthermore, the mathematical problem becomes a system of linear equations when a proper spatial discretization scheme (3D or 1D) is defined, such that the unknowns are estimated only at the spatial grid nodes. Our in-house solvers are based on a *finite-box* discretization method, with the continuity equations (2.2)–(2.5) discretized following the Scharfetter-Gummel scheme to cure the well known advection-convection problems stability issues [119]. This is obtained by assuming a constant current density between two adjacent grid nodes.

In D1ANA, a non uniform one-dimensional grid refined in the cavity region is adopted. Typically, less than 400 points ($n_z < 400$) are included in the mesh. In VENUS, the axisymmetric feature of the treated VCSELs is exploited to define a 2D triangular mesh grid instead of a three-dimensional one. Such a grid is based on the Voronoi tessellation [120]. In this way, the amount of linear equations associated to the original system remains computationally sustainable by a standard personal computer. The longitudinal mesh is kept identical to D1ANA ($n_z \approx 400$); the radial direction is discretized with 40 to 50 points ($n_\rho \approx 40$), resulting in an overall mesh nodes $nn = n_z \cdot n_\rho$ varying from 15000 to 20000. The 3D features are recovered by introducing the cylindrical coordinates by means of corrections to each column weight [121]. Notice that the triangles used for the discretization are right-angled and no vertex is allowed to lay on another triangle side. This simplifies the identification of each node neighbor and to keep the matrices sparse, at the cost of a less versatile mesh. Both these features are grasped from Fig. 2.6, where the 2D spatial grid used for a typical VCSEL simulation is shown at different degrees of zoom, going from the full domain (a) to the most important regions (c), where a finer grid is adopted to avoid losing crucial details of carrier transport.

Without showing the full derivation, each equation of the QCDD model is integrated over the control box surrounding each mesh node. This results in a system written in a simple sparse matrix form, easily manageable by a software such as MATLAB. Both VENUS and D1ANA numerically solve the discretized system by means of a generalized Newton's method. In fact, if an exact solution would be available, the final system could be written in the following form:

$$\underline{\underline{L}}\,\underline{u} + \underline{t} = 0 \tag{2.20}$$

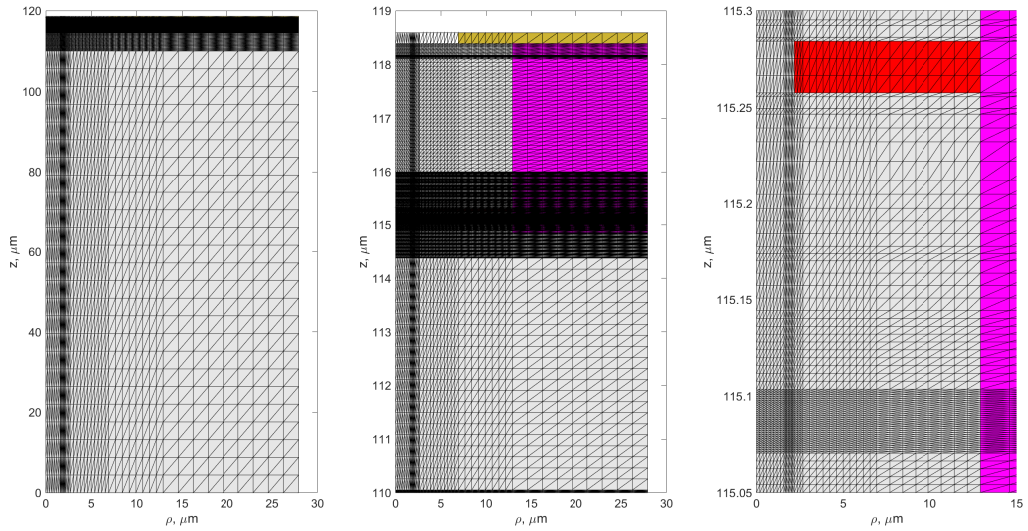

(a) Full domain (b) Substrate excluded (c) Proximity of oxide and AR

Fig. 2.6 Example of 2D spatial grid employed in a typical VCSEL simulation in VENUS. Different levels of zoom are provided. White regions: air; light gray: semiconductor; red: oxide; fuchsia: passivation; gold: top contact.

where the matrix $\underline{\underline{L}}$ contains the *linear* part of the *Jacobian* matrix, that directly multiplies the unknown terms (ϕ; n^{3D}, p^{3D}; N^{2D}, P^{2D}; $P_{st,m}$), contained in the vector $\underline{u}$. The $\underline{t}$ vector contains all the terms depending directly on the unknowns and the known terms such as the doping concentration. The dimension of these arrays depends on the number of mesh nodes (and thus the equations) used to discretize the VCSEL. The three bulk equations (2.1)–(2.3) introduce nn points in the vectors and $nn \times nn$ in the matrices. Additionally, each bound continuity equations (2.4)–(2.5) counts for $n_\rho \cdot N_{QW}$ points (N_{QW} being the number of QWs). The number of points related to the optical equation (2.13) is equal to the investigated modes N_{modes}. Lastly, two points are added for the circuit and current equations, discussed in Section 2.3. In summary, the total number of equations solved by the QCDD system is equal to $n_{tot} = 3nn + 2n_\rho \cdot N_{QW} + N_{modes} + 2$.

As mentioned, the system can only be solved in an approximated way, within a given tolerance. The system (2.20) must re-written by introducing a *residual* vector $\underline{r}$:

$$\underline{\underline{L}}\,\underline{u} + \underline{t} = \underline{r} \tag{2.21}$$

the ultimate goal of the Newton's scheme is the minimization of $\underline{r}$ with successive iterations. To this aim, the full *Jacobian* matrix must be assembled as $\underline{\underline{J}} = \underline{\underline{L}} + \underline{\underline{N}}$, where $\underline{\underline{N}}$ includes the *non-linear* derivatives of $\underline{t}$ with respect to each unknown. Fig. 2.7 (left) shows where the non-zero entries of $\underline{\underline{J}}$ are placed in D1ANA. The y-axis denotes the nodes index of the QCDD system of D1ANA. In VENUS is very similar, with additional filled diagonals due to the higher dimensionality of the domain. It is possible to identify various sub regions of $\underline{\underline{J}}$. Inside the orange dotted lines the derivatives of the bulk DD system (2.1)–(2.3), with the corresponding derivatives (on the x-axis) with respect to the bulk unknowns, are assembled in the $nn \times nn$ sub-matrix. Green dotted lines identify where bound carriers and their derivatives are inserted in the matrix. Inside the green circles there are the terms related to the QW capture (2.6)–(2.7). In the two figures on the right hand side of Fig. 2.7, we provide two zoom on the QW nodes of the electron continuity equation derivatives (top: derivative with respect to bulk electrons; bottom: with respect to bound electrons) - similar positions are taken by holes. The vertical sets of points correspond to the terms related to the capture (2.6), as they only depend on the quantities (quasi-Fermi levels, thermal voltage, bulk densities) taken at central node of each QW. The photon rate equations (2.13) add further rows and columns (N_{modes}), not highlighted in the figure for sake of plot clarity.

To work properly, the starting point of any Newton's scheme is a proper initial guess. At equilibrium, this is provided by computing a preliminary potential assuming it is pinned at neutrality at each mesh node. From this, Poisson equation (2.1) is solved. Afterwards, neutrality is only imposed at the contact boundary nodes. A reasonable guess for the successive bias points is ensured by the solution coming from the previous step. Below threshold voltage (~ 1.5 V in GaAs diodes), a 400 mV step can be used, that reduces to 50 mV (or 0.5 mA, depending on whether the VCSEL is voltage or current driven, as discussed in Section 2.3) when describing lasing operation. The Newton's scheme then proceeds iteratively by correcting and updating the initial guess of the unknowns:

$$\underline{u}^{(k+1)} = \underline{u}^{(k)} + \underline{\Delta u}^{(k+1)} \tag{2.22}$$

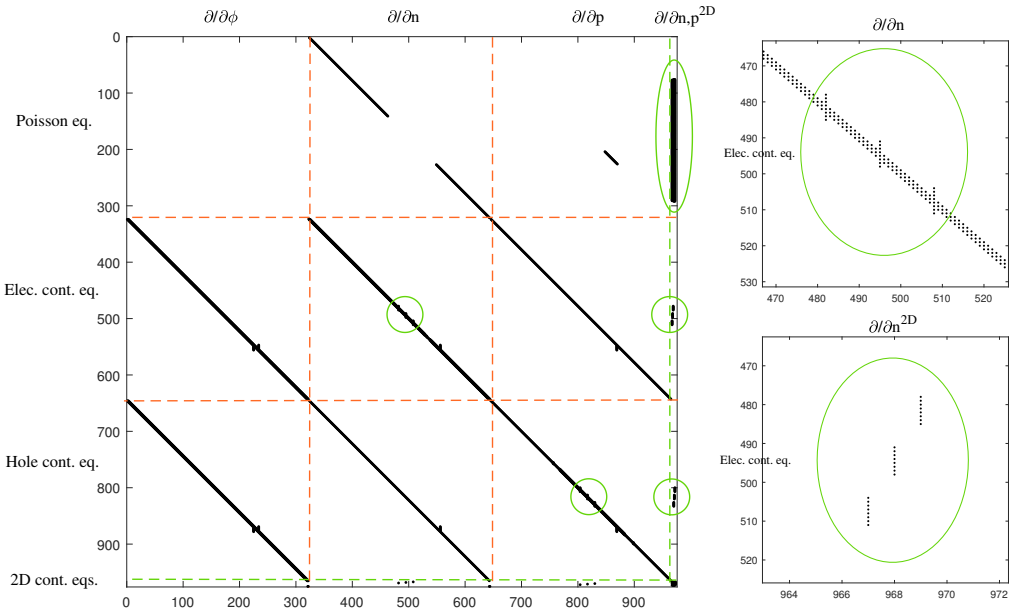

Fig. 2.7 $\underline{\underline{J}}$ non-zero entries position. On y-axis, the index related to each equation is reported; on x-axis, the partial derivatives related to each unknown is indexed. On the left, orange dotted lines are added to denote the bulk DD region and corresponding derivatives; green lines (and circles) identify the regions where bound carriers terms are assembled in the matrix. On the right, zoom on the electron continuity equation nodes related to the QWs. Top: derivatives with respect to bulk electron density; bottom: with respect to bound electrons.

where the superscripts denote the iteration indexes. The variation of the unknown vector $\underline{\Delta u}$ at $(k+1)^{th}$ iteration is determined by solving:

$$\underline{\underline{J}}\,\underline{\Delta u}^{(k+1)} = \underline{r} \tag{2.23}$$

Eq. (2.22) suggests that the Newton's scheme stopping criteria can be applied to the solution vector variation, other than the residual vector: the iterations stop when $\underline{\Delta u}^{(k+1)}$ is so small to produce a negligible variation to the solution vector $\underline{u}^{(k+1)}$.

At this juncture, it is worth commenting on the self-consistency of VENUS and D1ANA. In fact, while the NEGF-QCDD system (2.1)–(2.5) is solved self-consistently with the photon equation (2.13), the heat equation (2.19) is treated outside such an inner loop. The rationale behind this is associated with the huge degree of complexity entailed by resolving the full problem. Indeed, temperature enters in a plethora of material and model parameters, meaning that most of the zero entries in the *Jacobian* matrix would be substituted by partial derivatives of the QCDD equations with respect to temperature, and viceversa. Moreover, achieving temperature self-consistency would substantially escalate the number of iterations needed at every bias to meet the convergence standards of Newton's scheme, leading to considerably longer simulation duration. A straightforward workaround for the issue is to invoke the heat equation solver only upon QCDD system convergence. By doing so, the needed heat sources of (2.19) can be extracted at every bias and used to compute the temperature variation. Compensating for the absence of self-consistency is crucial to accurately forecast the operation of VCSEL. To this aim, we need to discuss a detail of our solvers. Some heat sources, such as the ones related to FCA, cannot be properly accounted within a microscopic view. At each bias point, VENUS and D1ANA check that the overall energy balance is ensured between dissipated thermal power P_{therm} (computed by integrating the heat sources in the VCSEL domain), input electrical power $P_{\text{elec}} = I \cdot V$ and output optical power $P_{\text{opt}} = P_{\text{st}} + P_{\text{sp}}$, which includes both stimulated P_{st} and spontaneous emission P_{sp} contributions:

$$P_{\text{therm}} = P_{\text{elec}} - P_{\text{opt}} \quad \rightarrow \quad f_{\text{corr}} = \frac{P_{\text{elec}} - P_{\text{opt}}}{P_{\text{therm}}} \tag{2.24}$$

If all the thermal sources would come directly from the QCDD, $f_{\text{corr}} = 1$. In our simulations, f_{corr} should account for any deviation from (2.24) left hand side relation. This is typically larger than 1, meaning that the thermal sources coming

from our self-consistent approach underestimate some terms. What f_{corr} does is to multiply all the sources of (2.19), to restore the balance imposed by (2.24). The issue of underestimating the thermal sources can be addressed by fitting the quantity $P_{\text{elec}} - P_{\text{opt}}$ and predicting what value will take at the successive bias point. This further increases f_{corr}, that is directly related to ΔT.

2.3 Voltage and current driving

A final point that must be mentioned concerns the external circuit supposed to drive out of equilibrium the VCSELs under test (see the corresponding block in Fig. 2.2). From a theoretical standpoint, the bias applied to an electronic device can be equivalently provided either by a voltage-controlled or by a current-controlled circuit. The mapping of one configuration into the other relies on the Thévenin and Norton equivalent circuit, as sketched in Fig. 2.8. On the contrary, in laboratories there is no doubt regarding the more convenient external circuit. In fact, imposing a bias current I_{bias} and measuring the voltage drop V_{cont} across the device under test is a much simpler operation, as it requires a voltmeter placed in parallel to it. Furthermore, driving an electronic device using current sources is safer, as some devices can be characterized by exponential IV relations, such that a small voltage variation leads to huge current rise possibly provoking damages. Related to this very practical reason, there is the possibility that the Newton's scheme implemented in our solvers fails to converge when the applied voltage step is large enough to produce a great current variation. On the other hand, the presented QCDD model includes the Poisson equation, whose unknown is the potential across the device. In our model it is straightforward to impose the applied bias to the mesh nodes supposed to be adjacent with metallic contacts, as a Dirichlet boundary condition at ohmic contacts:

$$V_{\text{cont}} = \phi - \phi_{bi} \tag{2.25}$$

where ϕ is the electrostatic potential at the contacts coming from (2.1) and ϕ_{bi} is the built-in potential given by:

$$\phi_{bi} = \pm \frac{k_{\text{B}} T}{q} \ln\left(\frac{|N_{\text{D}} - N_{\text{A}}|}{n_i}\right) \tag{2.26}$$

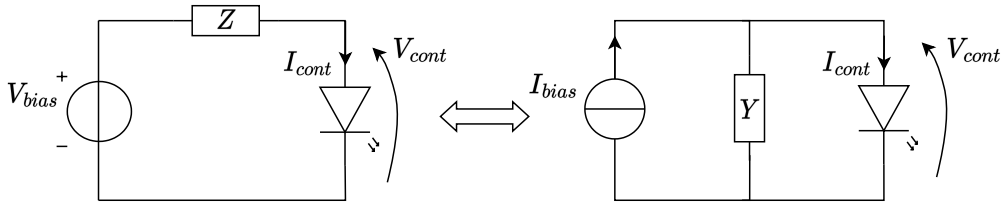

Fig. 2.8 Thévenin (left) and Norton (right) equivalent circuits, for voltage- and current-driven simulations. The voltage source providing V_{bias} and the impedance Z are related to Thévenin; current source providing I_{bias} and the admittance Y are related to Norton. I_{cont} and V_{cont} are current and voltage at VCSEL (represented as a diode) contacts.

where the sign depend on the ohmic contact doping type. From the DD standpoint, the convenient choice is the voltage-driving. To meet both real world schemes and implementation reasons, our solvers are capable of rump up both in bias (voltage-driven simulations) and current (current-driven simulations). These also permit to simulate non-ideal bias sources, taking into account both resistive and capacitive loads in the form of input impedance Z and admittance Y.

The possibility of choosing between voltage and current control is enabled by adding two further equations to the QCDD model (2.1)–(2.5), (2.13). One is the circuit equation [122]:

$$V_{\text{cont}} + ZI_{\text{cont}} = V_{\text{bias}} \quad \longleftrightarrow \quad V_{\text{cont}}Y + I_{\text{cont}} = I_{\text{bias}} \tag{2.27}$$

that relates the quantities depicted in Fig. 2.8. If the impedance Z or admittance Y are neglected, the external applied bias V_{bias} (I_{bias}) is equal to the one seen at the device contacts V_{cont} (I_{cont}). The left hand side of (2.27) refers to Thévenin equivalent, so to the voltage-controlled simulation: I_{cont} is the unknown quantity to be extracted from the DD simulation, whereas V_{cont} is imposed from (2.25). Conversely, the right hand side of (2.27) refers to Norton equivalent: V_{cont} in (2.25) is unknown and thus floating.

The second equation to be added is the current equation [122], whose unknown is I_{cont}, in both the simulation modes. This is readily extracted from the static DD simulation as follows:

$$I_{\text{cont}} = \oint_S (J_n + J_p) \cdot \hat{n} d\sigma \tag{2.28}$$

where $J_{n,p}$ are the current densities computed from (2.9)–(2.10), $\hat{n}$ is the normal unit vector to $J_{n,p}$ flow, and S is the area of the cross section where the flux integral has

to be evaluated, *i.e.*, the contacts. In case of current-driving simulations, I_{cont} is no more unknown, and V_{cont} is extracted from Poisson equation and (2.25). It is also to be remarked that voltage and current-driving simulations must return identical results, because there are no substantial differences in the DD model. On the contrary, convergence could be achieved at different number of iterations of Newton's scheme, depending on the device operating region. Despite the equivalency of the driving schemes, one should be aware that here the QCDD model is used to drive a *pin*-like junction out of equilibrium. This is substantially different from a resistor, that has a linear current-voltage characteristics. In fact, the current flowing inside a diode below electrical threshold is a badly defined quantity. Imposing current externally starting from equilibrium would pose serious convergence issues to the Newton's scheme. A smart choice consists in reaching threshold through voltage control, and then switch to current driving.

In this chapter, the workflow of D1ANA and VENUS is explained by showing one by one the solved equations of the various models. Electrical, optical and thermal problems are outlined, together with the details on how they are solved self-consistently. Some results from NEGF are shown on the TJ, to explain how its results are connected with our semiclassical QCDD solver. Then, some hints about the spatial discretization of the VCSEL adopted in the solvers are provided. Eventually, we illustrate the equations that bring the system out of thermodynamic equilibrium. This chapter represents the foundation for the simulation results presented in the following chapters about *pin* and TJ-VCSELs. We start from 1D simulations of a reference *pin* VCSEL to calibrate D1ANA (Chapter 3) and then move to the simulation of a TJ-VCSEL within our novel NEGF-DD scheme (Chapter 4). Finally, in Chapter 5, NEGF is introduced in VENUS, to assess the neglected radial features of the proposed AlGaAs TJ-VCSELs.

Chapter 3

D1ANA: a reduced model for *pin* VCSELs

The *pin* VCSEL simulations presented throughout the thesis deal with a fully characterized oxide-confined commercial device emitting at 850 nm, with measurements provided by Ulm University. The laser is a standard device based on $Al_xGa_{1-x}As$, with x denoting the Al molar fraction concentration. The VCSEL has been extensively investigated with VENUS in [67]. This reference device features a 1λ-optical cavity embedding three 8 nm GaAs QWs, defined by a couple of oppositely doped DBRs. In particular, the top outcoupling mirror is made of 21 pairs of p-doped layers, while the 36 pairs of the bottom DBR is n-doped. Both are composition and doping graded, to improve electrical conduction and minimize absorption losses [123]. The oxide layer is 30 nm thick to keep at minimum the scattering losses [124, 125] and has an aperture diameter of 4.35 μm, that provides both current and optical confinements. After thinning, the structure lies on a 110 μm thick n-type GaAs substrate. The top metallic contact consists of a metal ring (inner radius 6 μm) deposited on the topmost GaAs layer, where an ohmic contact is realized with a heavily p-doped GaAs layer with thickness 140 nm. After the metallic contact definition, the GaAs layer is etched down by 60 nm in the inner section of the metal ring. For a better understanding, please refer to the structure sketched in Fig. 1.2 of Section 1.1.

A key aspect of the proposed physics-based simulations is a proper choice for the material parameters. The set of parameters at 300 K used in VENUS and D1ANA is reported in [66, Table I] and summarized here in Table 3.1, with some modifications.

The meaning of some terms is explained throughout the chapter. Temperature dependencies are discussed in [126, 67]. As we work with III-V semiconductor alloys, a crucial resource is represented by the work done by Vurgaftman *et al.* in [104], even tough also other sources have been explored to retrieve all the material details, such as [127].

3.1 D1ANA calibration

The computational load associated with 3D solvers and even 2D solvers substantially restricts their usage in extensive optimization campaigns, which are of utmost significance for enhancing and testing novel designs. Taking this into consideration, we explore the feasibility of employing a multiphysics approach with reduced dimensionality to analyze the interrelated opto-electro-thermal operation of VCSEL [70]. In other words, we test how D1ANA performs in comparison with VENUS. The multiphysics version of D1ANA derives from an in-house 1D DD code [69], extended to couple optical and thermal solvers. It could be thought as an intermediate model between fully phenomenological rate equations and entirely physics-based 3D pictures (including VENUS), efficient enough to be employed in preliminary extended parametric studies and/or in optimization loops. The objective of this section is to examine which parameters need to be adjusted and assess the accuracy of the extracted features.

D1ANA operates on the vertical cut taken at the axis center of the axisymmetric 3D structure depicted in Fig. 3.1a. All the subproblems governing the VCSEL operation are reduced to one-dimensional problems in the longitudinal direction, that is the main direction of the current and heat flow and the photon emission. The DBRs are described including all the doping and compositional details only in the proximity of the active region (4 pairs on each side), while an electrically-equivalent medium is adopted elsewhere [69]. In 1D, the top contact position is by definition at the outcoupling optical section for the electrical problem, but it is instead eliminated in the 1D optical problem, otherwise the metal reflectivity would prevent photon emission. An important remark is that the one dimensional nature of D1ANA does not permit any inspection about the lateral confinement features of the VCSEL under investigation.A sketch of the domain simulated in D1ANA is represented in Fig. 3.1b, where a quasi 1D domain is actually depicted for an easier visualization.

Table 3.1 D1ANA and VENUS main $Al_xGa_{1-x}As$ parameters at $T = 300\,K$.

Parameter	Units	Value	Source
ε_r		$12.90 - 2.84x$	[104]
$E_{g0,\Gamma}$	eV	$1.519 + 1.155x + 0.37x^2$	[127]
$E_{g0,X}$	eV	$1.981 + 0.124x + 0.144x^2$	[127]
$E_{g0,L}$	eV	$1.815 + 0.69x$	[127]
$E_g(T)$	eV	$min(E_{g0,\Gamma,X,L}) - \alpha_{\Gamma,X,L}T^2/(\beta_g + T)$	[111]
$\alpha_{\Gamma,X,L}$	eV/K	$5.41(\Gamma), 4.6(X), 6.05(L) \cdot 10^{-4}$	[111]
β_g	K	204	[111]
χ	eV	$4.07 - 0.6(E_g(T) - E_{g,\mathrm{GaAs}}(T))$	[104]
ΔE_D, ΔE_A	meV	5, 26	[128]
$m^*_{n,\Gamma}/m_0$		$0.067 + 0.083x$	[129]
$m^*_{n,X}/m_0$		$0.850 - 0.140x$	[129]
$m^*_{n,L}/m_0$		$0.560 + 0.100x$	[129]
m^*_p/m_0		$0.55 + 0.26x$	[129]
μ_n	$cm^2/(s \cdot V)$	$8000 - 24000x + 13000x^2, \quad x \leq 0.45$ $1200(x - 0.45)^2 + 148, \quad x > 0.45$	[127]
μ_p	$cm^2/(s \cdot V)$	$400 - 775x + 535x^2$	[127]
$\tau^{\mathrm{SRH}}_{n/p}$	ns	10	[127]
$\tau^{\mathrm{SRH,QW}}_{n/p}$	ns	100	[127]
B^{rad}	cm^3/s	$1 \cdot 10^{-10}$	[127]
$C^{\mathrm{Aug}}_{n/p}$	cm^6/s	$5 \cdot 10^{-31}$	[115]
τ^{cap}_n, τ^{cap}_p	ps	10, 5	[82, 127]
κ_{air}	$W/(m \cdot K)$	0.025	[127]
κ_{metal}	$W/(m \cdot K)$	300	[127]
κ_{passiv}	$W/(m \cdot K)$	0.5	[127]
κ_{DBR}	$W/(m \cdot K)$	13.5	[130]
κ_{cavity}	$W/(m \cdot K)$	13.5	[130]
$\kappa_{\mathrm{substrate}}$	$W/(m \cdot K)$	41.5	[130]
β_T		1.20	[127]
dn/dT	1/K	$2.35 \cdot 10^{-4}$	[73]

As a consequence of dimensionality downscaling, D1ANA simulates VCSEL operation in about 80 s on an ordinary laptop (Intel Core i7-8550U, 1.80 GHz), which is about 30 times faster compared to VENUS, applying the same control parameters (voltage grid and convergence criteria for the Newton solver). Capitalizing on this enhanced computational efficiency, we utilize D1ANA to optimize the examined device for high-temperature operation. Nevertheless, it should be noted that the considerably faster code is meant for an initial and rough identification of the parameter space to meet given specifications. After being identified by D1ANA, VENUS should be applied for the final and finest details, including modal characteristics. Above all, these include the side-mode suppression ratio, in the case of typically desired single-mode operation. We foresee other interesting applications of the calibrated D1ANA. For example, in Chapter 4 it is used to test new hole injection schemes for next generation of near-IR VCSELs; in particular, to switch from oxide-confined VCSELs to TJ 850 nm devices [98, 131, 132]. Another possible application is to conduct quick assessments of critical parameters, like cavity length, doping levels, and etching of the topmost GaAs contact layer. In fact, this requires a multispace parameter analysis that is not conceivable with VENUS. D1ANA can also be extended to perform time-domain analysis, wherein the dynamical system of equations is solved instead of searching for its steady-state solution [133]. This would enable the examination of the impact of noise on VCSEL operation, as well as offer a fresh outlook for exploring complex modulation schemes like PAM4 (Pulse-Amplitude Modulation) or more advanced ones, by employing a highly accurate multiphysics approach, currently impractical to be implemented within a 3D framework due to computational power limitations.

3.1.1 Parameters alignment

As mentioned, our purpose is to isolate a subset of parameters taken from Table 3.1 that should be tuned to mimic the radial effects that are naturally neglected in a longitudinal solver. Some examples are the optical transverse features, the current crowding effects around the oxide aperture, and the radial heat dissipation outside the active volume. The work done in [70] has highlighted the following list of four parameters that must be determined:

- Rescaling of thermal conductivities $\kappa(z,T)$

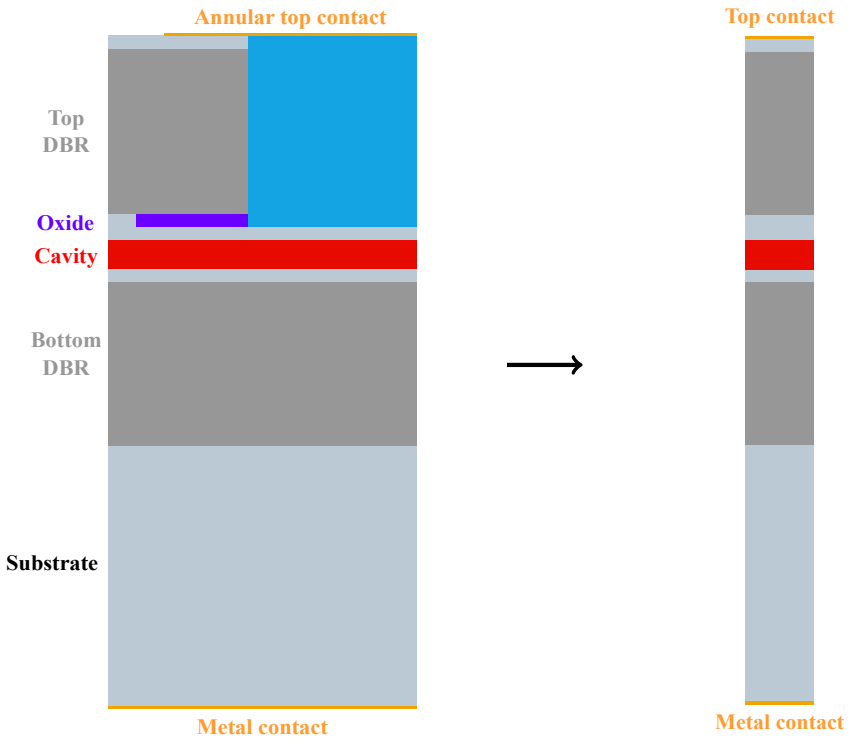

(a) VENUS (b) D1ANA

Fig. 3.1 (**a**): VCSEL 2D schematic and (**b**) 1D central cut simulated with D1ANA. In the electrical simulation, the top contact is vertically aligned to the bottom contact. Lateral confinement cannot be investigated.

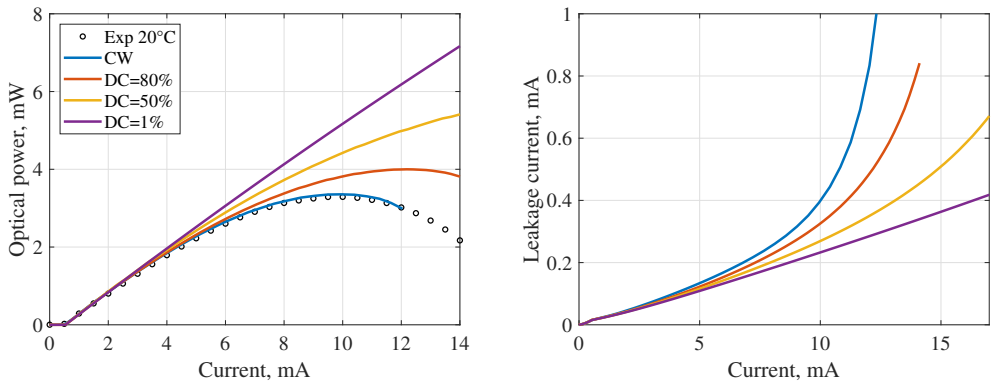

(a) *LI* (b) Leakage current

Fig. 3.2 Effect of heating in VCSEL operation (CW – continuous wave; DC – duty cycle) at 20°C. Output optical power (**a**) and leakage current (**b**) as functions of bias current, extracted from D1ANA.

- Temperature dependence of β_T
- Rescaling of dn/dT
- Definition of an effective size

Once these parameters are found, D1ANA can be extensively employed at a much lower computational cost compared to VENUS. With this work, the identification of the calibration parameters for different kind of VCSELs would be much faster.

Thermal conductivities

In D1ANA, it possible to mimic the effects of a pulsed operation regime by varying the duty cycle (from DC $= 10\%$ to continuous wave) of the injected current. The corresponding light-current *LI* characteristics are shown in Fig. 3.2a. This demonstrates that heat is the main performance killer in VCSELs, the responsible of power roll-over and degradation at high operating temperatures. Self-heating both shifts and quenches the optical gain spectrum (see Fig. 3.11), but it also impacts on the current leakage, as shown in Fig. 3.2b: larger current densities are needed to keep high optical powers.

As discussed in [66, 67], while optical and electrical domains can be much reduced compared to actual device size, the solution of the steady-state heat equation (2.19) should include the full actual domain (see Fig. 2.1). Let's recall that κ is

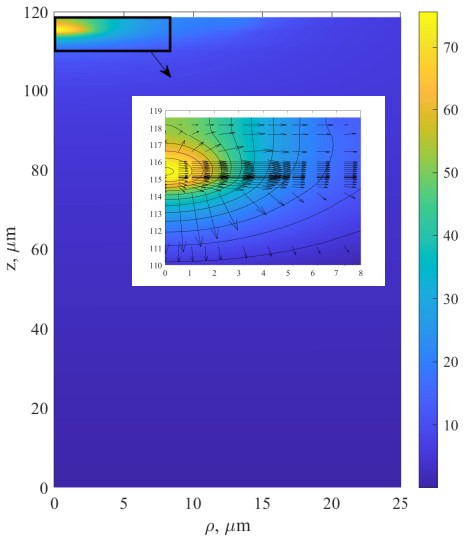

(a) Temperature rise map $\Delta T\,(z,\rho)$ on the "electrical domain", set as half of the thermal one. In the inset, a zoom of the VCSEL region (DBRs + cavity), with contour lines at 5°C steps and arrows indicating heat flow.

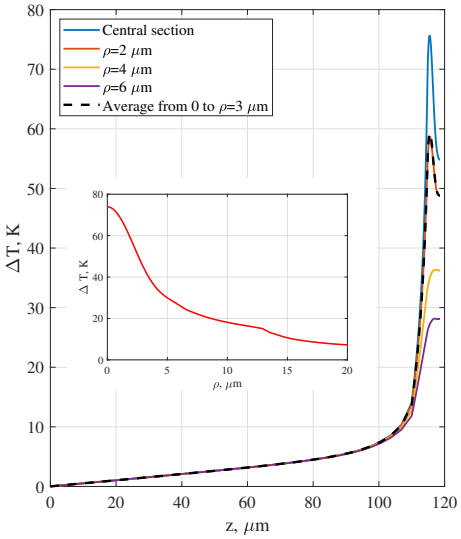

(b) Temperature profiles $\Delta T\,(z)$ cut at different radii (solid lines) and oxide aperture averaged temperature (black dotted line). The inset shows the radial temperature variation $\Delta T\,(\rho)$ at the central QW node.

Fig. 3.3 Temperature rise in our reference *pin* VCSEL, at $T_{\text{amb}} = 20°\text{C}$ and injected current of 10 mA, corresponding to the maximum optical power of about 3.3 mW. (**a**): $\Delta T\,(z,\rho)$ in the whole device; (**b**): longitudinal $\Delta T\,(z)$ from VENUS at varying radii.

the spatially-varying thermal conductivity (see Table 3.1). Therefore, stretching the actual thermal problem to a 1D longitudinal equation is the most challenging and demanding task in our investigation. To help the discussion, in Fig. 3.3a we show the actual 3D thermal profile from VENUS, at peak output power. The heat sources, apart from Joule heating, which is not dominating, are focused in the MQW region, *i.e.*, a tiny part of the whole device, about 50 nm in longitudinal direction and 4 μm in the transverse direction, accounting for carrier lateral diffusion compared to the 2.175 μm oxide aperture radius. This has to be compared with the 12 times larger transverse size of the VCSEL (radius 25 μm), that, in terms of area, translates into a factor of 144. This can be interpreted as a heat source filling factor of the thermal transverse domain. In a 1D perspective, (2.19) loses azimuthal and radial dependence (shown as an inset of Fig. 3.3b), and retains just the longitudinal variable z; the gradient operator reduces to a derivative along z.

Due to the much focused heat source, in VENUS the radial decay of temperature is steeper at the MQW section, as shown by the different longitudinal cuts in Fig. 3.3b (solid lines) and also by the black arrows in the inset of Fig. 3.3a, representing the heat flow. We must carefully investigate and discuss how to treat such a major difference. As said, optical and electrical environment are mainly developing at the structure axis. The oxide aperture serves as both current and optical confinement. Therefore, carriers also nearly follow the oxide aperture size, indeed allowing for some lateral spreading due to diffusion. Tightly connected to carriers is the gain profile, that consequently is similarly defined by the oxide aperture. The interaction with optical gain of the guided modes and, in particular, of the fundamental mode (crucial, as most of the relevant sensing and *datacom* applications are aiming at single mode operation) also completely occurs within the oxide aperture. Therefore, the temperature values relevant in VCSEL operation are those close to the axial region. The surface average of the transverse temperature profile over the oxide area is shown in Fig. 3.3b with a dashed black line, and it represents the target for the 1D fitting. In Fig. 3.4, such averages are reported for two currents (4 and 10 mA), together with the achieved reduced dimensionality fits. These are obtained by rescaling the temperature diffusion coefficients (corresponding to substrate and VCSEL layers) by factors related to the previously discussed transverse filling factor of the heat source compared to the thermal domain. In particular, equivalent one-dimensional thermal conductivities matching the best fit between the previously defined radial average of the 3D map and 1D longitudinal profiles are retrieved. In the substrate, the thermal conductivity is scaled by a factor 115 that accounts for the filling factor discussed above. Also, the thermal conductivity varies radially, especially in the mesa region where the filling factor is larger (passivation area almost does not contribute to heat dissipation). This results in a tiny scaling factor of 2.5 in the VCSEL region. In practice, the original values [67] of thermal conductivities $\kappa_{\text{substrate}} = 41.5$ W/m/K and $\kappa_{\text{DBR+AR}} = 13.5$ W/m/K are rescaled by a factor 115 in the substrate and 2.5 in the VCSEL region (DBRs + AR). The 1D and 3D results fit nicely in Fig. 3.4, especially in the most important section (the AR), and the major deviations are observed in the transition between substrate and mesa. In that region, 3D effects make the temperature profile smoother than in the 1D simulation, where a sharp slope change is observed. This is the consequence of the abrupt discontinuity in the values of thermal conductivities of the two thermal domains in the one-dimensional limit

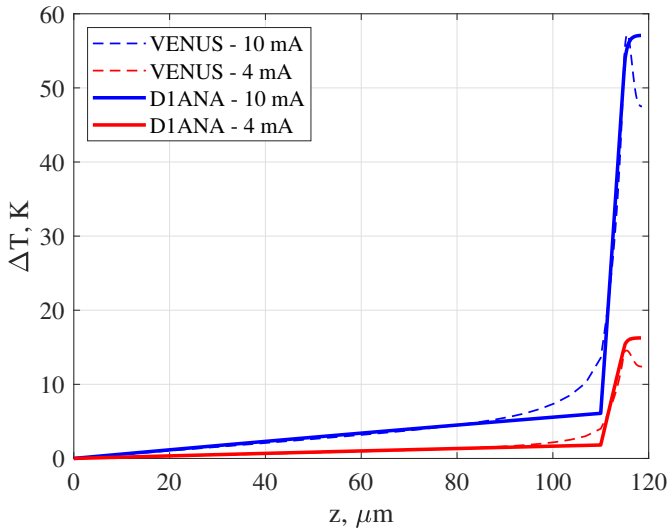

Fig. 3.4 Temperature variation ΔT along z direction. Dashed lines: oxide aperture averaged 3D temperature longitudinal cuts at 4 (in red) and 10 mA (in blue). Continuous lines: 1D approximation.

and to the mathematical methods adopted to solve the heat equation, as discussed in Section 2.1.4.

Refractive index temperature dependence

The only macroscopic observable quantity linked to temperature, even indirectly, is the emission wavelength λ [134], that varies during operation due to the temperature dependence of the semiconductor refractive index n_r, that can be linearized as follows [73, 135]:

$$n_r(T) = n_r(T = 300\,\mathrm{K}) + \frac{dn_r}{dT}(T - 300\,\mathrm{K}) \tag{3.1}$$

Such a change in refractive index modifies the resonance frequency of the optical resonator, and it can be measured by extracting $d\lambda/dT$ at different heat sink temperature and at small currents, where inner temperature rise is still small. Finally, dn_r/dT in (3.1) is evaluated as:

$$\frac{dn_r}{dT} = \frac{\bar{n}}{\lambda}\frac{d\lambda}{dT} \tag{3.2}$$

where $\bar{n} = 3.25$ is the VCSEL effective refractive index and λ is the emission wavelength [67]. Together with the FCA profile, the temperature dependent refractive

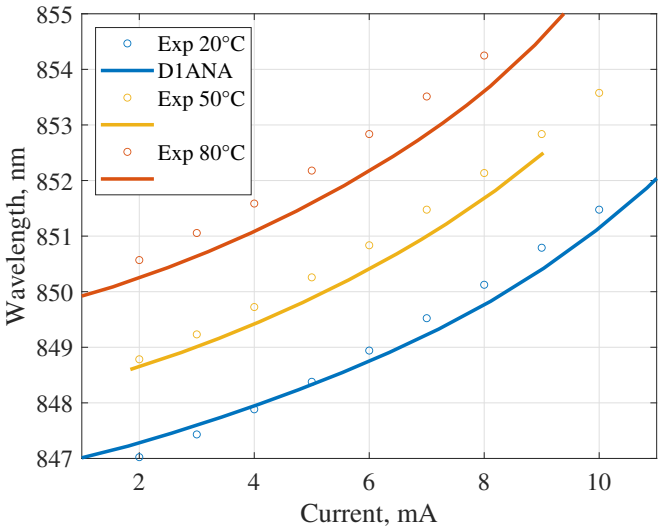

Fig. 3.5 Wavelength red shift vs. current, for different ambient temperatures (20, 50, 80°C). Experimental values (open circles) are compared to 1D computed values (solid lines).

index longitudinal profile causes the most important variation of the optical features during operation. In fact, λ position determines the spectral point where the gain must be evaluated. As shown in Fig 3.5, we have also carefully calibrated this parameter, so as to have a best fit with the experimental results. This requirement is explained by highlighting that the computed thermal profiles are averages across the inner area (see Fig. 3.3b); on the other hand, the actual profile at the center, where the fundamental mode is also peaked, is higher, resulting in a stronger effect on λ. The temperature rise must be compensated by a larger coefficient to match the experimental results. In the end, in D1ANA $dn_r/dT = 4 \cdot 10^{-4}\,\mathrm{K}^{-1}$, thus almost doubled with respect to the value used in VENUS of $2.35 \cdot 10^{-4}\,\mathrm{K}^{-1}$.

Effective oxide aperture size

An essential detail missing in D1ANA compared to VENUS is the lack of absolute current and optical power values; in fact, a 1D model delivers just densities per unit area. The best way to find this parameter is to introduce an effective area to fit the *LI* experimental curve [136]. The effective area is here assumed equal for optical power and current as oxide aperture provides confinement to both. Using the actual oxide aperture as a reference area, in Fig 3.6 we show the effect of different size factors (SF). A factor of 4 on the area (corresponding to a doubled radius) provides the

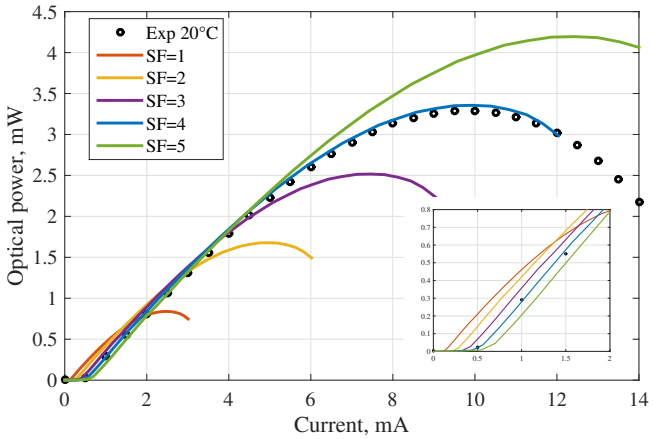

Fig. 3.6 Experimental *LI* characteristics ($T_{\text{amb}} = 20°\text{C}$) compared with the 1D model, with different size factors (SF). The inset shows the threshold behavior.

best fit on both threshold (and also roll-over) current and maximum optical power. For the electrical problem, this is best explained by current spreading beyond the oxide aperture (current crowding effects) and carrier lateral diffusion. For the optical problem, the wider area accounts for the larger transmission of a 3D mode compared to a 1D simulation (plane waves). In fact, as well known, 3D optical threshold gain is always larger than in a 1D simulation.

Optical performance at high ambient temperatures

In view of improving performance at high ambient temperatures, we must take the last step of testing our calibrated D1ANA model in those operating conditions. This is realized in Fig. 3.7, for three experimental ambient temperatures (namely $T_{\text{amb}} = 20$, 50, 80°C). It appears that a constant β_T of 1.2 [67], excellent at room temperature, results in an overshoot of temperature rise at higher ambient temperatures. We recall that this parameter rules the decrease of thermal conductivity with temperature, representing a nonlinear effect in the heat equation [137]:

$$\kappa = \kappa_{300\,\text{K}} \left(\frac{T}{300\,\text{K}} \right)^{-\beta_T} \tag{3.3}$$

Therefore, β_T is varied so as to achieve a good accordance between experimental and computed *LI* at $T_{\text{amb}} = 80°\text{C}$. A good match is obtained for $\beta_T = 0.55$. For

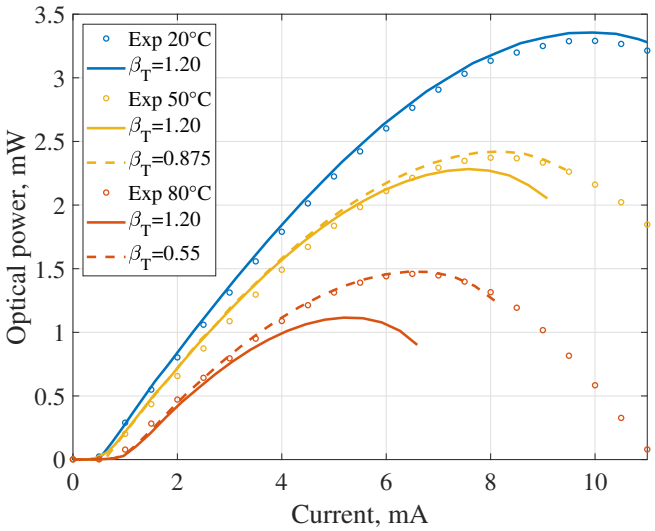

Fig. 3.7 *LI* characteristics of the *pin* VCSEL extracted with D1ANA at three different ambient temperatures (20, 50, 80°C). Open circles refer to experimental results, dashed lines to the proposed calibrated 1D model, eq. (3.4), solid lines to a constant $\beta_T = 1.2$.

intermediate temperature values, $\beta_T(T)$ is interpolated linearly, obtaining:

$$\beta_T(T) = 1.2 - 0.011 \cdot (T - 293\,\mathrm{K}) \tag{3.4}$$

This last adjustment matches also the *LI* curves obtained from the VCSEL measurement. D1ANA is ready to serve for our next purposes.

3.2 Small-signal analysis

An interesting application of D1ANA is the extraction of the small-signal parameters of the VCSEL under test. In particular, the latter analysis permits to evaluate the VCSEL amplitude modulation response as a function of frequency and bias condition, to extract the -3 dB cutoff frequency. A small-signal is a time-varying voltage or current with amplitude much smaller than the stationary (DC) bias point. The small-signal condition allows to treat the perturbation to the QCDD system as linear. From this, a further assumption consists in imposing that no harmonics can be generated (time-harmonic variation assumption), authorizing to express the signal in a simple phasor form. The unknowns of the DD model (2.1)–(2.5), (2.13) can be rewritten as

[138, 139]:

$$\begin{cases} \phi(t) \simeq & \phi_{\mathrm{DC}} + \hat{\phi}(t) = \phi_{\mathrm{DC}} + \tilde{\phi}\exp(j\omega t) \\ n(t) \simeq & n_{\mathrm{DC}} + \hat{n}(t) = n_{\mathrm{DC}} + \tilde{n}\exp(j\omega t) \\ p(t) \simeq & p_{\mathrm{DC}} + \hat{p}(t) = p_{\mathrm{DC}} + \tilde{p}\exp(j\omega t) \\ P_{\mathrm{st}}(t) \simeq & P_{\mathrm{st,DC}} + \hat{P}_{\mathrm{st}}(t) = P_{\mathrm{st,DC}} + \tilde{P}_{\mathrm{st}}\exp(j\omega t) \end{cases} \tag{3.5}$$

where the subscript DC denotes the DC working point and $\tilde{\phi}$, $\tilde{n}$, $\tilde{p}$ and $\tilde{P}_{\mathrm{st}}$ indicate the amplitude of the signal that enters in all the unknowns (including both 3D and 2D), with pulsation $\omega = 2\pi f$. By substituting (3.5) into (2.1)–(2.5) and (2.13), and linearizing the system around the DC bias point with a first-order Taylor expansion, some additional terms are added to the DC *Jacobian* matrix $\underline{\underline{J}}$. These are related to the carrier dynamics and to the displacement current derived from the Maxwell's equations.

As discussed in Section 2.2, $\underline{\underline{J_{\mathrm{DC}}}}$ is already computed as the major ingredient for the solution of the nonlinear DD system through the Newton's method. Therefore, at convergence of stationary condition, the AC analysis is readily available. Our approach is first validated by comparing the small-signal features of a trivial *pin* structure with a commercial simulator, as shown in Fig. 3.8 [136]. It is to be remarked that this validation is pertinent only to the electrical features (resistance and conductance), since, to the best of our knowledge, no commercial simulator implements both the AC analysis and quantum corrections/photon rate equations associated to a physics-based solver.

At present, the heat equation (2.19) is not self-consistent with the QCDD system (as explained in Section 2.1.4), *i.e.,* all the partial derivatives related to temperature are not included in $\underline{\underline{J_{\mathrm{DC}}}}$. For this reason, it is reasonable to test the model only in the linear part of the *LI* characteristic, that is the case for $I_{\mathrm{DC}} = 1$ and 2 mA, where temperature still plays a marginal role. This procedure only extracts the *intrinsic* VCSEL modulation response together with the contribution given by the chip parasitics. However, a major impact to modulation bandwidth also comes from the pad parasitics, that together with the chip determines the *extrinsic* laser response [140–144]. Parasitics should be minimized because they provide alternative paths to the modulated current, deteriorating the VCSEL response. Each contribution can be visualized in the schematics reported in Fig. 3.9. More into details, in Fig. 3.9a all the parasitic elements are reported. C_p and R_p are the pad capacitance and

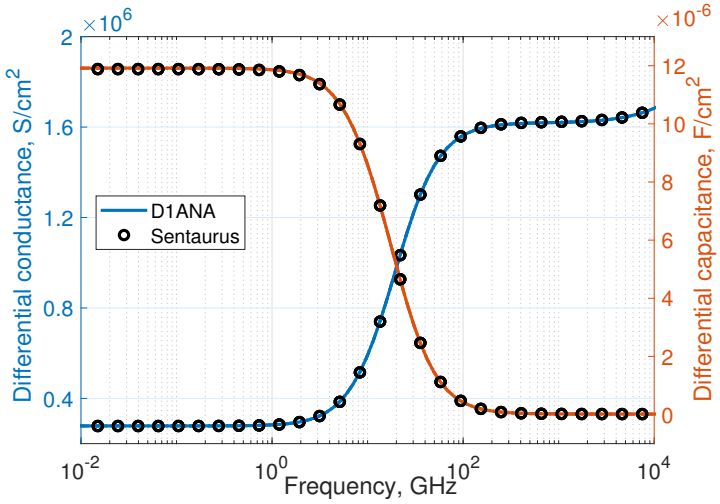

Fig. 3.8 Comparison of differential conductance and capacitance spectra of a *pin* diode (300 nm *p*-type, $N_A = 1 \cdot 10^{19}\,\mathrm{cm}^{-3}$; 10 nm intrinsic layer; 300 nm *n*-type $N_D = 1 \cdot 10^{19}\,\mathrm{cm}^{-3}$), computed by D1ANA and *Sentaurus Device*.

resistance between probe driver and metal contacts, while R_{cont} is the resistance of both metal contacts: R_p and R_{cont} are so small that can be neglected. Much more relevant is R_m, namely the resistance associated to the DBRs. Also the active region together with the oxide aperture introduce further elements. Capacitance C_a takes into account the oxide C_{ox} and the intrinsic region C_{int} capacitances, together with the diode junction capacitance C_j of the *pin* junction (typically dominated by a diffusion capacitance [9]). Similarly, the intrinsic laser is represented by the junction resistance $R_j = R_a$. In Fig. 3.9b, a simplified small-signal equivalent circuit is sketched, to better grasp the relevant contributions. Here, v_s denotes the signal source and Z_0 is a characteristic impedance, included to account for the RF power reflection due to impedance mismatch.

The modulation frequency response can be written as a product between intrinsic and extrinsic contributions:

$$H(\omega) \equiv |H_{\mathrm{ext}}(\omega) \cdot H_{\mathrm{int}}(\omega)|^2 = \left| \frac{i_a(\omega)}{v_s} \cdot \frac{p(\omega)}{i_a(\omega)} \right|^2 \tag{3.6}$$

where $H_{\mathrm{int}}(\omega)$ relates photon density fluctuations $p(\omega)$ to the injected modulating current $i_a(\omega)$ as a two-pole transfer function, and $H_{\mathrm{ext}}(\omega)$ is a single-pole low-pass filter function between the current flowing into the intrinsic diode and the voltage

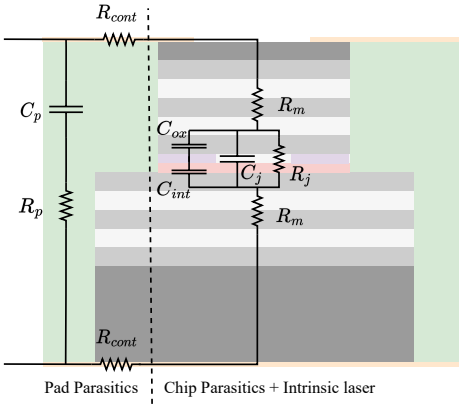

(a) Parasitic elements superimposed to a VCSEL schematic.

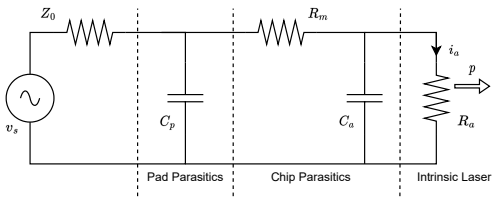

(b) Small-signal equivalent circuit, including the driving source.

Fig. 3.9 Oxide-confined VCSEL typical parasitics (**a**) and simplified equivalent circuit (**b**).

v_s. Overall, a VCSEL can be modeled with a three-pole equation, with a maximum bandwidth not exceeding 20 GHz.

The computed amplitude modulation (normalized) response of the device at room temperature is shown in Fig. 3.10 as continuous lines, together with the experimental curves (open circles), which display the well know oscillation relaxation peaks. As the current increases, the optical response of the VCSEL has a flatter peak shifted to higher frequency, and features higher speed. In fact, photon and carrier modulation follow current modulation for frequencies up to relaxation, which in turn depends on the bias current itself, and then drop at -60 dB/dec, according to (3.6). This is shown in the computed spectra superimposed to the experiments, in a range of currents from 1.2 to 3.2 mA. Both experimental data and D1ANA results predict a cutoff frequency at around 10 GHz, far from the 20 GHz limit. Even though the overall behavior is captured by D1ANA, still we do not have a satisfactory matching at equal current values. At smaller current, D1ANA result is far from experimental curve by approximately 20%. Conversely, the AM response at 2 mA is actually reproduced by a simulated current closer to 3 mA. Further works will address this issue, starting from thermal phenomena and a proper modeling of pad parasitics, that are promising candidates for the observed differences. A relevant phenomenon accounted in D1ANA small-signal analysis is the nonlinearity of gain, induced by spectral hole burning or carrier heating [9, 145]. In D1ANA this is modeled through the gain compression factor ε_{NL}, that reduces the gain (denoted by

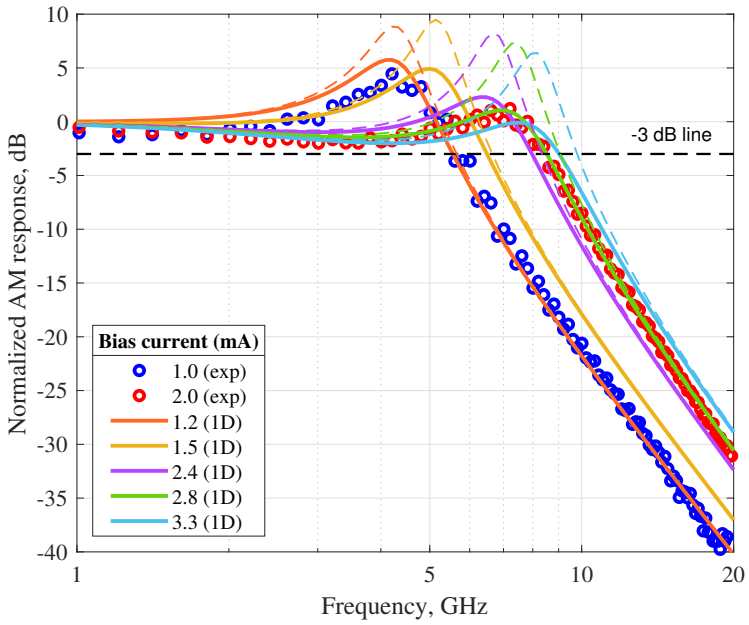

Fig. 3.10 AM response of the *pin* oxide-confined VCSEL. Open circles denotes the experimental data at 1 mA and 2 mA. Solid lines are the curves extracted from D1ANA at different injection conditions, with $\varepsilon_{NL} = 4 \cdot 10^{-17}$ cm^3; dashed lines have $\varepsilon_{NL} = 0$.

$g(N) = g(N^{2D}, P^{2D}, \lambda_m, T))$ coming from the QWs as follows:

$$g(N,S) = \frac{g(N)}{1 + \varepsilon_{NL} S} \tag{3.7}$$

with S denoting an equivalent photon density computed as:

$$S = \frac{|\mathscr{E}_m(\rho)|^2 P_{\mathrm{st},m}}{\int_0^{2\pi} \int_0^{\rho_{\max}} |\mathscr{E}_{\mathrm{out},m}(\rho)|^2 \rho d\rho d\phi} \frac{1}{\hbar \omega_m} \tag{3.8}$$

which also entered inside the stimulated recombination rate (2.18) in Section 2.1.3: refer to that equation for the description of all the (3.8) terms. In our simulations, $\varepsilon_{NL} = 4 \cdot 10^{-17}$ cm^3. The dashed AM responses are obtained with $\varepsilon_{NL} = 0$, demonstrating that this parameter does not significantly reduce the bandwidth (and the DC operating conditions) but mainly impacts on the oscillation relaxation peak damping. In fact, the relative amount of gain compression $\varepsilon_{NL} S$ is small also at high steady-state optical power [145].

From design considerations, the VCSEL under test is not fully oriented towards high-speed purposes. In fact, the AR is embedded in a 1λ-cavity. A sizable improvement would be offered by an anti-guiding design (A-VCSEL), with a $\lambda/2$ cavity centered on GaAs QWs included in AlAs-rich layers. This would increase the oscillator strength, enhancing the modulation bandwidth [8].

3.3 Oxide-confined VCSEL 1D optimization

Let's now employ the calibrated D1ANA suite to investigate possible improvements of the reference VCSEL structure. In the perspective of optimized high temperature operation, the cavity detuning ($\Delta\lambda$) serves as an indicator of a suitable design. $\Delta\lambda$ is defined as the wavelength difference between the maximum of the gain spectrum and the emission wavelength, as sketched in Fig. 3.11. As discussed in Section 2.1.1, $g(N^{2D}, P^{2D}, \lambda_m, T)$ at different operating conditions is extracted by applying the Fermi's golden rule. This is a preeminent parameter for optimized operation, as the gain spectrum red-shifts with T much faster than the emission wavelength [146], by about a factor of four. For instance, taking Fig. 3.5 as a reference, for a temperature rise of about 60 K inside the VCSEL, the wavelength shifts by 4 nm. Correspondingly, the gain spectrum moves by 15 nm (blue and yellow gain spectra in Fig. 3.11).

With D1ANA, a parametric simulation is carried out to find the optimal value of $\Delta\lambda$ at two temperatures. The results are reported in the top figures of Fig. 3.12. Fig. 3.12a proves that the device under test is already optimized for room temperature operation, with $\Delta\lambda = 0$ (blue curve). Different values would either increase the threshold current from 500 μA ($\Delta\lambda = -3$ nm) or reduce the maximum output power from 3.3 mW ($\Delta\lambda = +6, +10$ nm). On the contrary, at 80°C (see Fig. 3.12b) a similar analysis suggests that a $+15$ nm cavity detuning appears to be beneficial (purple curve). In fact, the maximum optical output power would increase by 1 mW, from 1.5 (blue curve, $\Delta\lambda = 0$) to 2.5 mW, yet leaving the threshold current almost unchanged at 1 mA. The behavior at the two temperatures can be understood from Fig. 3.11, by comparing the different interactions between the optical line with the gain spectrum in the two cases of the nominal design (λ_{nom}) and of the optimized one (λ_{opt}). At $T_{amb} = 20^{\circ}$ C (blue curve in Fig. 3.11), λ_{nom} has a proper distance from λ_{opt}, such that the self-heating brings the VCSEL in the optimal condition for gain. Changing

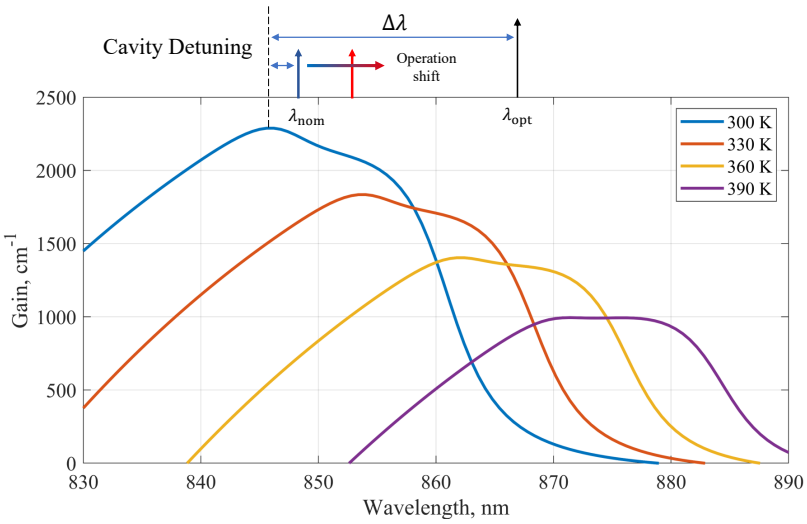

Fig. 3.11 Gain spectra at different ambient temperatures and typical carrier sheet densities of $4 \cdot 10^{12}\,\mathrm{cm}^{-2}$. The concept of cavity detuning $\Delta\lambda$ is sketched at the top of the figure.

$\Delta\lambda$ would lead to a reduced gain region. Conversely, at $T_{amb} = 80°$ C a $g(\lambda)$ curve between yellow and purple of Fig. 3.11 can be expected. This suggests that a larger detuning (*e.g.*, $\Delta\lambda = +15$ nm), is beneficial at high temperature conditions. If $\Delta\lambda$ becomes too large, only the threshold current is negatively affected, without any improvement to the maximum power. This is the case of $\Delta\lambda = +15$ nm, as shown in green in Fig. 3.12b.

Another detail that strongly impacts both on the output power and threshold current is the DBR radiation loss. The top DBR radiation losses are "useful losses", *i.e.*, the optical output power (instead, the radiation in the substrate is lost). However, one must not think that the stronger the bottom DBR reflection, the better. In fact, DBRs also induce absorption losses. Additionally, the bottom DBR is the main barrier for heat toward the heat sink. This is related to the worse thermal conductivity to the ternary (AlGaAs) DBRs compared to the binary GaAs substrate, by a factor of 3. In the bottom figures of Fig. 3.12, D1ANA is employed to examine the impact of altering the thickness of DBRs at two ambient temperatures of 20 and 80°C. At room temperature (Fig. 3.12c), the removal of two output pairs improves the maximum optical power up to 4.5 mW from 3.3 mW of the nominal VCSEL, with a minor change of the threshold current (solid red curve). A further reduction of two pairs (solid yellow curve) induces a maximum optical power of 5.5 mW, due to the *LI* slope enhancement. However, the threshold current would almost double from the original

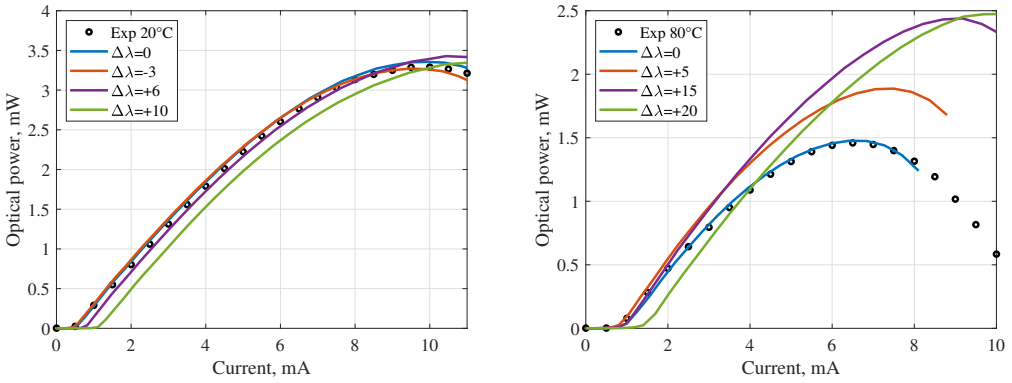

(a) $T_{amb} = 20°C$ - $\Delta\lambda$ optimization

(b) $T_{amb} = 80°C$ - $\Delta\lambda$ optimization

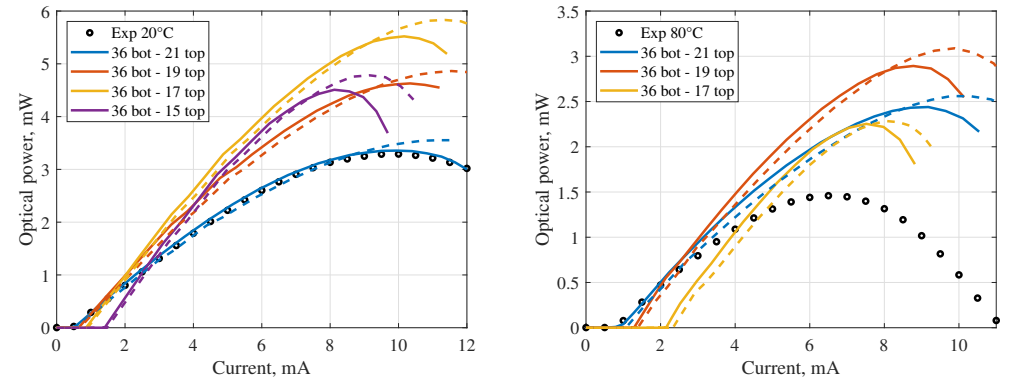

(c) $T_{amb} = 20°C$ - DBR optimization

(d) $T_{amb} = 80°C$ - DBR optimization

Fig. 3.12 Oxide-confined *LI* characteristics at 20°C (**a-c**) and 80°C (**b-d**) ambient temperatures. Cavity detuning optimization is shown in (**a-b**); top and bottom DBR optimization (**c-d**). In the latter, at 80°C (**d**), $\Delta\lambda = +15$ nm is used (**b**). Dashed lines refer to 31 pairs bottom DBR.

value of 0.5 mA. The best design depends on the final purpose of the VCSEL. For configurations just mentioned, the peak optical power is reached at 10 mA. D1ANA predicts that a thinner output DBR (15 pairs instead of 21, in purple) would cause a relevant deterioration of the threshold current (1.75 mA) with the maximum power smaller that the 17 and 19 pairs cases. This is related to the device self-heating increase, which deteriorates its performance also in terms of maximum output power, reached at a lower current (8 mA). On the same plots, with dashed lines, the case of a thinner bottom DBR is also reported. In particular, 5 pairs are removed, shortening the VCSEL of about 650 nm. The corresponding characteristics are fully in line with our previous comments. The thinner bottom DBR affects the optical losses, and thus the threshold slightly increases, and the *LI* curves are shifted to the right compared to the thicker mirror. The improved thermal performance results in a delayed thermal rollover, enabling a marginal enhancement of the maximum output power.

Coming back to Fig. 3.11, moving from 300 (in blue) to 390 K (in purple) the available gain more than halves (assuming fixed QW sheet carrier density levels) due to the larger broadening of the Fermi distributions. This is the main reason that eventually prevents VCSEL operation above certain temperatures. Essentially, the reduced gain should be compensated by a higher current density, that, in turn, is responsible for stronger recombinations. These are converted into heat, in a positive feedback loop that soon prevents lasing. Nonetheless, at 80°C, with the optimized cavity detuning of $\Delta\lambda = +15$ nm discussed in Fig. 3.12b and a DBR optimization (31 pairs in the bottom DBR, 19 in the top), it is possible to double the maximum output power with respect to the values measured during the experiments, from 1.5 to 3.1 mW, at a current of 10 mA (see red dashed curve in Fig. 3.12d). This is the same experimental value that provides the peak output power at room temperature. Therefore, the early rollover of the actual device at a higher temperature is related to its improper cavity detuning. Again, notice that the DBR modification shifts the threshold current from 1 mA to 1.6 mA. If a smaller value is preferred, one should keep the top DBR untouched (blue dashed curve), taking in mind that the peak power reduces from 3.1 to 2.6 mW.

To conclude, in this chapter we identify from the parameters list used in VENUS to simulate a reference commercial 850 nm AlGaAs VCSEL a subset that should be trimmed to calibrate a one dimensional version of the solver, called D1ANA (Section 3.1). D1ANA is enabled of returning static characteristics close to experimental data at heat sink temperatures ranging from 20 to 80°C. In Section 3.2, the same

solver is extended to perform a small-signal analysis of the *pin* VCSEL: the extracted amplitude modulation response is compared to experimental measurements. The model is also validated with results extracted on a *pin* junction simulated within Sentaurus Device. Section 3.3 is devoted to the application of D1ANA for fast parametric campaigns, needed to improve the longitudinal design of VCSELs. From this chapter we obtain a reliable 1D solver, used in the following chapter to test our NEGF-DD scheme on TJ-VCSEL simulations, which are the ultimate goal of the thesis.

Chapter 4

TJ-VCSELs 1D preliminary assessment

As discussed in Section 1.1, the TJ concept is a technological enabler for lasers emitting into UV and mid-IR wavelength windows. In this chapter, hole injection in 850 nm AlGaAs VCSEL AR from a TJ is first assessed within our one-dimensional NEGF-QCDD framework, as presented in Section 2.1.2. As mentioned at the beginning of Chapter 3, D1ANA is not capable of distinguishing between confinement coming from an oxide layer or from a radially structured index step above the TJ. Lateral optical and electrical confinement will later be discussed in Chapter 5, where the NEGF-DD scheme is applied to VENUS. Section 4.1 is devoted to the presentation of the test TJ-VCSEL structure, obtained from a reference device. Then, Section 4.2 compares the static electrical and optical characteristics to the *pin* VCSEL, at various temperatures. The most relevant differences between TJ and *pin* VCSELs are discussed. D1ANA is then used for a parametric study cavity detuning and DBR pairs, to get an optimal design of the TJ-VCSEL at 80°C.

4.1 TJ-VCSEL test structure

The purpose of this section is to highlight the advantages of AlGaAs TJ-VCSELs by providing a comparison with an equivalent *pin* device [132], within our one-dimensional framework. Again, the commercial *pin* VCSEL described at the beginning of Chapter 3 is taken as a reference. The test TJ-VCSEL is designed by us

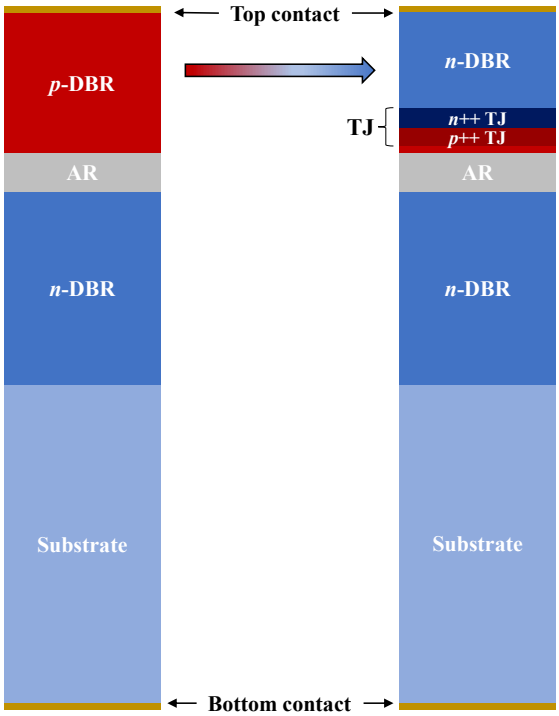

Fig. 4.1 Sketch of 1D approximation applied to the *pin* (left) and TJ-VCSEL (right). Blue regions denote *n*-doping; red regions are *p*-doped; in grey the undoped AR.

to be as close as possible to the *pin* VCSEL, in order to provide a fair comparison between the different hole injection schemes. This justifies the use of the same set of 3D to 1D trimming parameters discussed in Section 3.1.1, complemented with the interband generation rate introduced to treat the TJ, as presented in Section 2.1.2.

Let's start from the main differences arising between the two devices in our 1D approximation. From the sketch in Fig. 4.1, substrate, bottom *n*-DBR and active region remain unchanged, whereas the introduction of a TJ just above the AR significantly modifies the original *pin* structure. As discussed, this admits to exploit *n*-doping also in the top DBR. Hence, the TJ-VCSEL embeds a *pin* junction working in forward bias and a *pn* junction reverse bias condition. This setup can be thought of as two junctions connected in an anti-series configuration, which means that the current flowing through a TJ-VCSEL is determined by the TJ operation [98]. The characteristics of the bare TJ, extracted using our NEGF simulation, is illustrated in Fig. 2.3b of Section 2.1.2.

As mentioned, the adoption of D1ANA does not permit to investigate the lateral confinement features. In a 1D framework, when the confinement area is defined, it is equivalent to assume the presence of an oxide aperture layer or of a radial refractive index step induced by a epitaxial regrowth over a buried TJ. Therefore, a TJ should define an equivalent current and optical confinement with respect to the oxide-confined *pin* structures. Hence, the effective size estimated in the 1D analysis to fit the experimental results in [70] should mimic well also the lateral features of the BTJ-VCSEL, as it does for the oxide-confined one. In fact, by forcing the same transverse geometrical dimension of the annular contact ring, the current coming from the contacts should flow similarly across the two devices. In both cases, no current can flow aside the buried TJ or oxide aperture. Also the TJ-VCSEL should be affected by current crowding effects, but they are expected to be less severe due to the improved electrical conductivity of the top DBR. This could have an impact on transverse mode competition, which cannot be addressed using a one-dimensional approach. For this reason, the use of VENUS in Chapter 5 is crucial for a proper characterization of TJ-VCSELs.

A proper TJ placing inside the VCSEL should be aimed at limiting the impact of the strong FCA losses induced by high doping levels of the TJ. In particular, the TJ *n*-side is doped with tellurium [47, 147–149], to reach a high density level $N_{\mathrm{D}} = 3 \cdot 10^{19}\,\mathrm{cm}^{-3}$; *p*-side is C-doped, with density $N_{\mathrm{A}} = 2 \cdot 10^{20}\,\mathrm{cm}^{-3}$. An abrupt doping profile is assumed across the TJ, neglecting any dopant diffusion in such heavily doped regions. With this assumption, an absorption of $\alpha \approx 2500\,\mathrm{cm}^{-1}$ is computed for the TJ using the formula reported in [128, p. 175]:

$$\alpha = f_{\alpha}\left(\alpha_n \frac{n}{10^{18}\,\mathrm{cm}^{-3}} + \alpha_p \frac{p}{10^{18}\,\mathrm{cm}^{-3}}\right) \tag{4.1}$$

with coefficients $\alpha_{n,p}$ and fitting factor f_{α} extracted in [67] and equal to 3, 7 and 2.9 respectively. From (4.1), longitudinal absorption coefficient profiles including also the DBRs are extracted for the two structures and reported in Fig. 4.2 [150]. Light blue line refers to the TJ-VCSEL, showing the aforementioned strong absorption peak at TJ position at $z \approx 115.3\,\mu\mathrm{m}$. Yellow curve refers to the *pin* VCSEL. In the bottom DBR, that extends on the left starting before 115 μm, α_{pin} is superimposed to the TJ-VCSEL profile because the devices are identical. At the outcoupling side, the top DBR begins at $\approx 115.4\,\mu\mathrm{m}$ and the TJ-VCSEL displays a relevant absorption coefficient reduction, going from 40–60 cm^{-1} of the *p*-DBR to 5–20 cm^{-1} of the

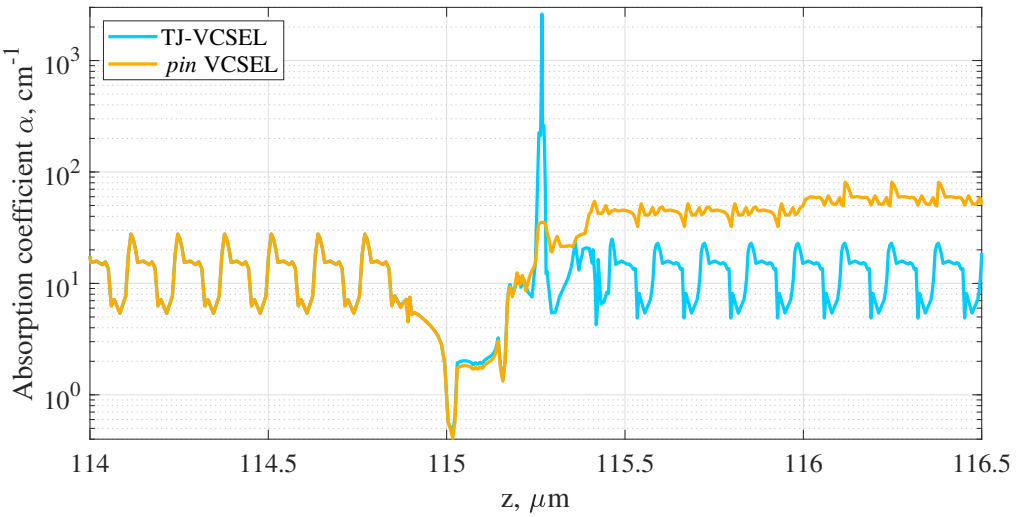

Fig. 4.2 Longitudinal absorption coefficient profile α. In the TJ-VCSEL (light blue line) there is a strong absorption in the TJ (at $z \approx 115.3\,\mu$m), whereas in the top DBR (right mirror) it is greatly reduced with respect to *pin* device (orange dashed line). In the bottom DBR, α are superimposed.

n-DBR, identical to the bottom DBR. Inside the 100 nm of the AR between 115 and 115.1 μm, very similar values of α are predicted by our model.

The switch of outcoupling mirror doping type allows to reduce by two the number of DBR pairs, to account for lower FCA losses in *n*-doped materials. As a result, VELM in its 1D form predicts matched threshold gain for the two structures, namely, $G_{\text{th}} = 1440\,\text{cm}^{-1}$ for the reference oxide-confined VCSEL, and $G_{\text{th}} = 1480\,\text{cm}^{-1}$ for the TJ-VCSEL. In Fig. 4.3, the optical SW along the longitudinal direction of the two devices coming from VELM are superimposed to the corresponding refractive index profiles. The VCSELs are identical up to the end of cavity. The central QW of both is centered in an optical SW antinode to maximize the gain enhancement factor. The TJ is placed in the first node of the SW after the AR, embedded in the top DBR first pair, in the same position of the oxide aperture of the *pin* VCSEL. Therefore, electrical and optical confinement position is assumed to be unchanged. Lateral confinement in TJ-VCSELs is further investigated with VENUS in Chapter 5.

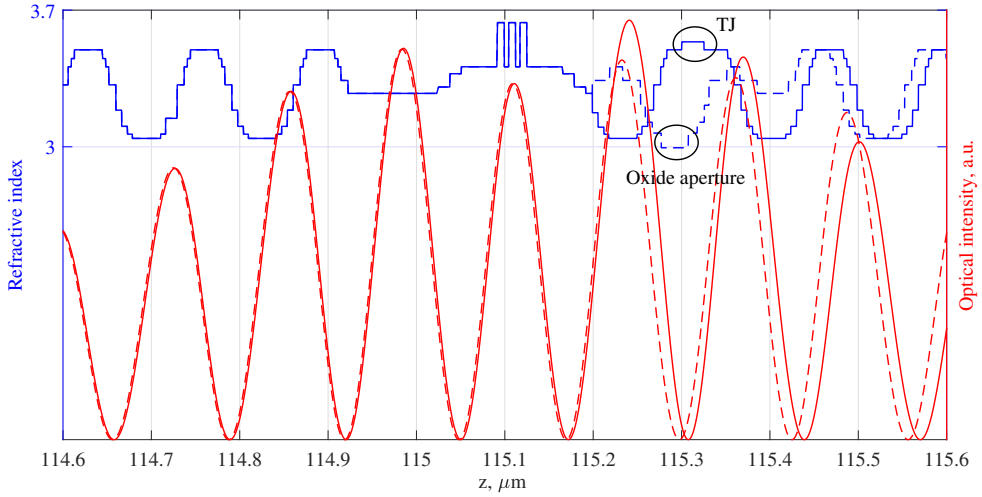

Fig. 4.3 Refractive index (in blue) and standing wave (in red, from VELM) for the two VCSELs: continuous lines - TJ; dashed - *pin*. Ground contact is placed at $z = 0\,\mu$m, output light is emitted at the right hand side. QWs are aligned; the TJ shifts SW and refractive index by 5 nm.

4.2 Static characteristics comparison

The TJ-VCSEL figures of merits are now assessed with the calibrated D1ANA and compared to the *pin* VCSEL, keeping in mind that a 1D approach cannot distinguish between confinement provided by an oxide aperture and by a lithographically defined refractive index step. Therefore, D1ANA only evaluates the benefits offered by a modified outcoupling mirror.

Typical quantities accessible through our physics-based approach are the energy band diagrams. In Fig. 4.4, they are reported for both the VCSELs, at a bias voltage of 2 V. It is worth noticing that the oxide-confined *pin* VCSEL has the typical band diagram of a *pin* junction in forward bias, almost in flatband conditions at the bias voltage considered in Fig. 4.4a. On the other hand, TJ-VCSEL band diagram displays the strongly-localized band bending needed to open a tunneling window, that enables an efficient injection of holes into the active region (Fig. 4.4b). This demonstrates the TJ-VCSEL working principle.

The static figures of merits are compared starting from Fig. 4.5a, where the *IV* characteristics of the oxide- and TJ-confined VCSELs (solid and dashed lines, respectively), computed at different ambient temperatures of $T_{\text{amb}} = 20$ and 80°C.

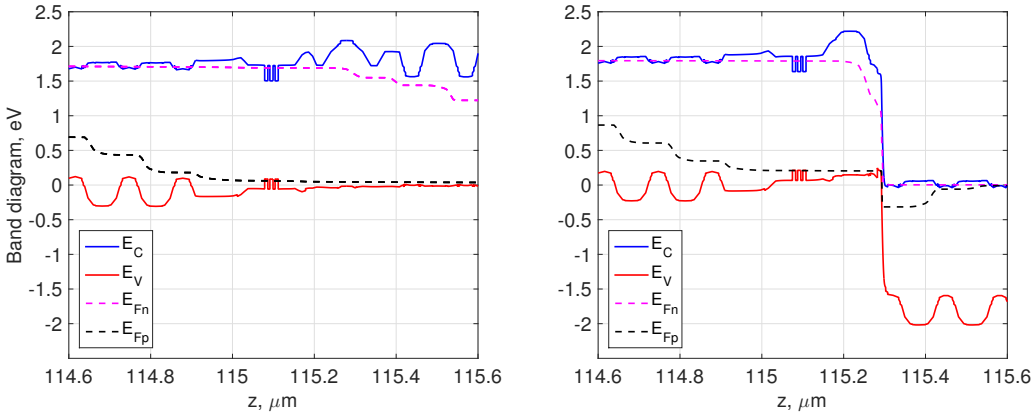

(a) *pin* VCSEL. (b) TJ-VCSEL.

Fig. 4.4 Band diagrams in the cavity proximity, extracted at 2 V bias from D1ANA.

Experimental values (circles) are also reported for the reference structure: as discussed in Section 3.1, D1ANA provides a good agreement with these results. In the whole bias window, the TJ-VCSEL simulations return lower currents at all temperatures. This is related to the series resistance introduced by the TJ. In fact, the voltage drop V_{TJ} across the TJ has an increasing behavior from 0 to 0.7 V, which translates in a voltage difference with respect to the reference structure. Nevertheless, the output power emitted by the TJ-VCSEL is almost doubled for all the investigated temperatures, as the *LI* characteristics reported in Fig. 4.5b shows. The improvement in the optical performance is related to the reduced number of pairs in the outcoupling DBR mirror needed to match the threshold gain of the reference VCSEL, or in other words, with the lower optical losses of the top DBR. This derives from reasoning explained during the *pin* DBR optimization presented in Section 3.3: the TJ makes it even more effective.

The well known phenomenon of the thermal rollover obviously occurs also in the TJ-VCSEL. At a certain bias current, the output power cannot grow anymore, and the VCSEL slowly approaches the turn-off. Thermal rollover is a consequence of VCSELs self-heating. To this aim, it is worth checking each thermal source contribution to the overall heating process. In Fig. 4.6a, temperature increase induced by every source (Joule – red, FCA – green, non-radiative recombinations – blue) are reported as function of the input electrical power $P_{\mathrm{elec}} = I \cdot V$ in both the structures. The curves demonstrate that recombinations play similar roles in *pin* (solid lines) and TJ-VCSEL (dashed lines). Joule heating curves are even closer, due to an

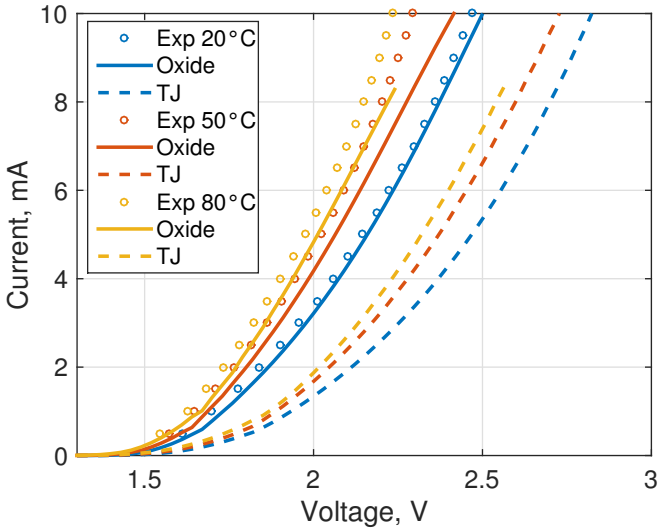

(a) *IV*

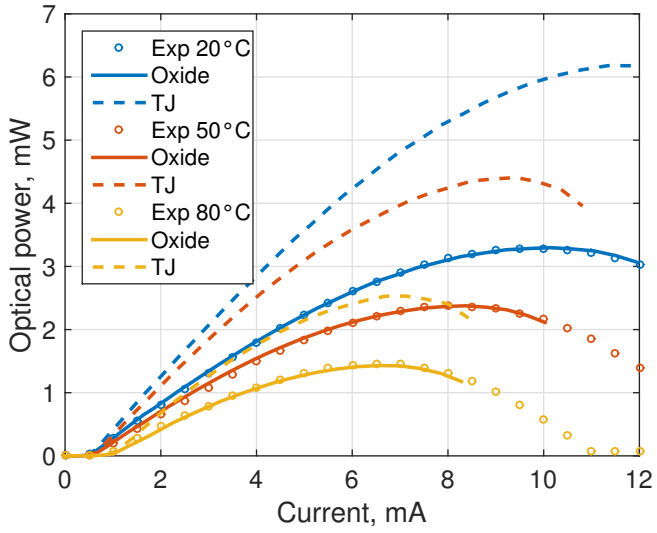

(b) *LI*

Fig. 4.5 Static *LIV* at 20, 50, 80°C, computed for the oxide-confined (solid lines) and TJ-VCSEL (dashed lines) with D1ANA. Reference VCSEL experimental results are marked with open circles.

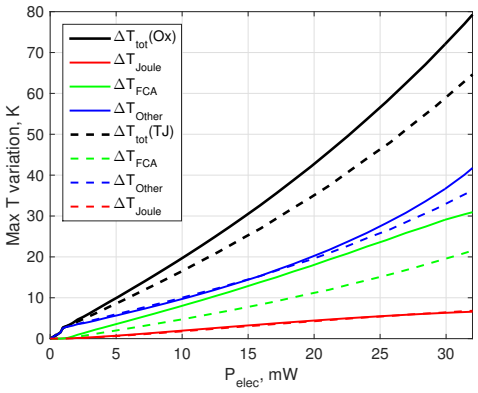

(a) Maximum temperature rise ΔT induced by each thermal source (Joule - red, FCA - green, GR processes - blue, total - black), vs. driving electrical power P_{elec} (solid: *pin*, dashed: TJ-VCSEL).

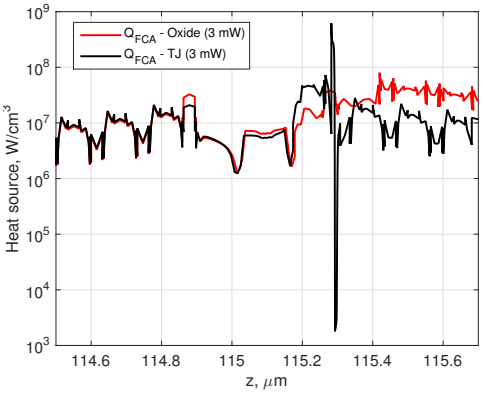

(b) Zoom in the cavity proximity of FCA heating sources at equal output optical power of 3 mW (red: *pin*, black: TJ-VCSEL).

Fig. 4.6 Heat sources insights from D1ANA across the *pin* and TJ-VCSEL. (**a**): maximum ΔT as a function of driving power $P_{\text{elec}} = V \cdot I$ and (**b**): FCA heating source in the longitudinal direction.

improved conductivity compensated by the aforementioned voltage penalty. A strong discrepancy comes from the temperature rise coming from FCA, that is greatly reduced in TJ-VCSEL. Therefore, higher optical powers are sustained before the critical temperature of the thermal rollover are reached. Fig. 4.6b shows the FCA heat source profiles in the oxide- and TJ-devices at equal output power (3 mW). In the bottom DBR they are nearly identical, while in the TJ-VCSEL top *n*-DBR, the losses are significantly reduced, as expected from (4.1).

In Fig. 4.7a the emission wavelength red shifts are compared. The $\lambda(I)$ characteristics are comparable in the two devices confirming that, despite the much higher output optical power provided by the TJ-VCSEL, the self-heating effects remain comparable to the reference structure at equal electrical power. To conclude the static figures of merits discussion, in Fig. 4.7b the wall-plug efficiencies (WPEs) are shown. WPE (η_{WP}) can be seen as a summary of electrical and optical performances, since $\eta_{\text{WP}} = P_{\text{opt}}/P_{\text{elec}}$. At all the simulated temperatures, the TJ-VCSEL displays larger WPEs: at 20°C, the peak value of η_{WP} rises from 23% to 31%; at 50°C, from 20% to 28%; at 80°C, from 15% to 20%, *i.e.,* an improvement in the range of 20-30% is achieved. Although the electrical penalty due to the TJ injection scheme, the enhancement in the optical power largely compensates it in terms of efficiency, thus

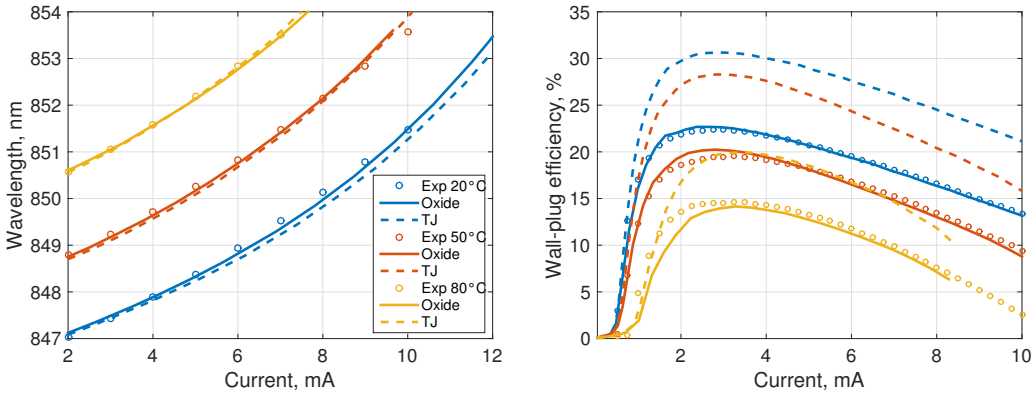

(a) $\lambda(I)$ (b) η_{WP}

Fig. 4.7 (**a**) Emission wavelength and (**b**) wall-plug efficiency (η_{WP}) vs. current, at different temperatures (20, 50, 80°C), computed for the oxide-confined (solid lines) and TJ-VCSEL (dashed lines) with D1ANA. Reference VCSEL experimental results are marked with open circles.

suggesting that the TJ design may represent the right direction towards optimized 850 nm VCSELs for optical interconnects.

4.3 VCSEL optimization for datacenter communications

Near-IR VCSELs are primarily employed in short-range interconnects in hyperscale datacenters, such as server racks, where ambient temperatures up to 80°C are reached. Here we present a process of optimization similar to the one performed at the end of Section 3.3 for the *pin* VCSEL. The analysis is performed with the same parametric studies. First, the optimal cavity detuning, is retrieved; then, the DBR thickness is investigated to reach the best performances.

Fig. 4.8a shows *LI* characteristics of VCSELs simulated at 80°C, for different values of $\Delta\lambda$. The black open circles indicate the experimental *LI* characteristics of the reference device, already reported in Fig. 4.5b. The best trade-off between maximum optical power and minimum threshold current is reached imposing $\Delta\lambda = +15$ nm, reported in purple. This is the same value retrieved for the oxide-confined VCSEL in Fig. 3.12b, here reported as a solid black line. This outcome is reasonable considering our efforts in changing as few layers as possible across the two structures. Higher val-

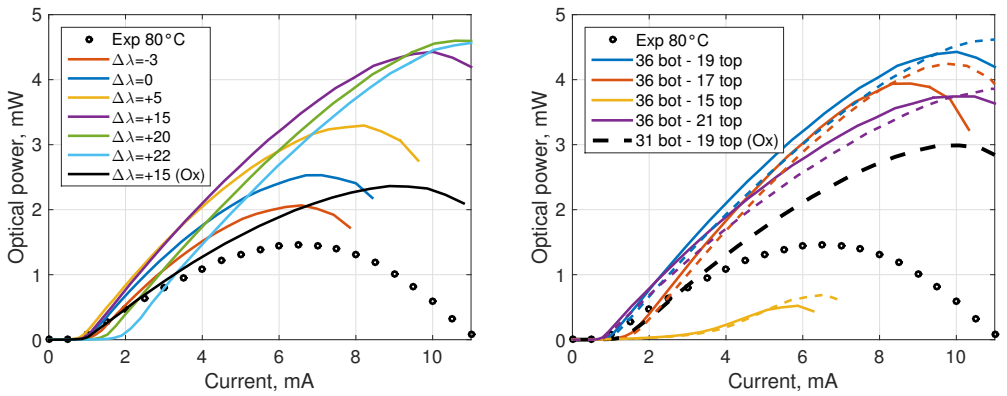

(a) $\Delta\lambda$ optimization. Black solid line corresponds to the oxide-confined VCSEL with $\Delta\lambda = +15$ nm.

(b) DBR optimization, with $\Delta\lambda = +15$ nm. Black dashed line corresponds to the oxide-confined VCSEL, with 31 bottom and 19 top DBR pairs.

Fig. 4.8 TJ-VCSEL optimization of *LI* at 80°C. Black open circles represent the experimental results for the reference device. Colors indicate different (**a**) values of $\Delta\lambda$ or (**b**) numbers of pairs in the top DBR.

ues of $\Delta\lambda$ do not bring any substantial advantage to the optical characteristic. Thus, it is important to underlining that the optimization on the TJ-VCSEL moves the peak optical output power from 2.4 (coming from the optimized *pin* VCSEL) to 4.5 mW, without introducing any penalty on the threshold current, which demonstrates the potential of TJ-VCSELs for high-temperature operation.

Following the same path of the *pin* VCSEL, the second parametric analysis determines the optimal number of DBR pairs in the mirrors, keeping fixed $\Delta\lambda = +15$ nm. Purple, red, blue and orange lines in Fig. 4.8b have been obtained with 21, 19, 17 and 15 pairs in the outcoupling DBR, respectively. Solid and dashed lines are used to distinguish results obtained with substrate DBRs with 36 and 31 pairs, respectively. The best choice for the outcoupling mirror is 19 pairs, that is the value that matches the losses of the reference *pin* device at 20°C and it guarantees the highest output power without impacting on the threshold current. In fact, if the number of pairs is increased to 21, the threshold current is slightly affected, but radiation losses are reduced. On the other hand, if the number of pairs is decreased to 17, the optical threshold gain increases, and self-heating mediated by recombination processes anticipates the thermal rollover. When the number of pairs in the outcoupling mirror is further decreased to 15, the maximum power is reduced to 0.7 mW (yellow curves). The dashed lines in the same figure show that a thinner

bottom DBR (5 pairs shorter) gives some advantages. Indeed, the better thermal management results in a retarded rollover, which extends the current operation range and guarantees a marginal improvement of the maximum output power. Finally, the black dashed line shows the *LI* characteristics of the optimal oxide-confined VCSEL, displaying how the TJ-VCSEL enables an overall 30% improvement of the maximum output power, and a 30% reduction of the threshold current.

Chapter 4 represents our first step toward the modeling of AlGaAs TJ-VCSELs within our in-house NEGF-DD solvers. D1ANA serves the scope by simulating only the central section of a test device, adopting the same parameters listed in Chapter 3. The differences between our test TJ-VCSEL and the *pin* design are outlined in Section 4.1: the absorption coefficients are superimposed to appreciate the benefits of a *n*-doped top DBR. The SWs of both designs are provided to show the placement of the TJ inside the VCSEL structure. The band diagrams at the beginning of Section 4.2 help to understand why the electrical characteristics differ. The predicted enhancement of the optical features are also confirmed by improved efficiencies, in the whole investigated temperature range. Similarly to the last section of Chapter 3, in Section 4.3 we exploit D1ANA to improve the design the test TJ-VCSEL at 80°C. After having tested the NEGF-DD scheme in D1ANA, in Chapter 5 we deploy it in VENUS to ensure that our prediction are confirmed within a solver involving also the radial features.

Chapter 5

VENUS TJ-VCSEL analysis

In the thesis, the ultimate stage involves migrating the NEGF-DD concept presented in Section 2.1.2 and introduced in D1ANA in Chapter 4 to VENUS. In previous works [66–68], our group has extensively exploited VENUS to investigate standard AlGaAs oxide-confined *pin* VCSELs, with an oxide aperture diameter of 4.35 μm and thickness of 30 nm. In this section, VENUS is used to fulfill the final goal of the thesis, namely the complete investigation of a test AlGaAs TJ-VCSEL. The designs of two oxide-confined TJ-VCSELs discussed in Section 5.1 are conceived by introducing the TJ proposed in [98] inside the commercial *pin* VCSELs that our group has already investigated in past works. Actual AlGaAs TJ-VCSELs may possibly differ from these configurations. Here we want to assess the advantages of introducing a TJ in conventional oxide-confined short-wavelength AlGaAs VCSELs and prove the effectiveness of VENUS in treating TJ-VCSELs. The analyzed designs involve the presence of an oxide aperture placed in the proximity of a planar TJ radially extended from the VCSEL center to the mesa end. In Section 5.1.1, VENUS simulations at 20°C permit to identify a preferred position of the TJ and oxide aperture, that is not feasible in D1ANA. The inner quantities extracted by our physics-based approach are exploited to justify the differences between the proposed configurations. For a list of the main material parameters used in VENUS, refer again to Table 3.1.

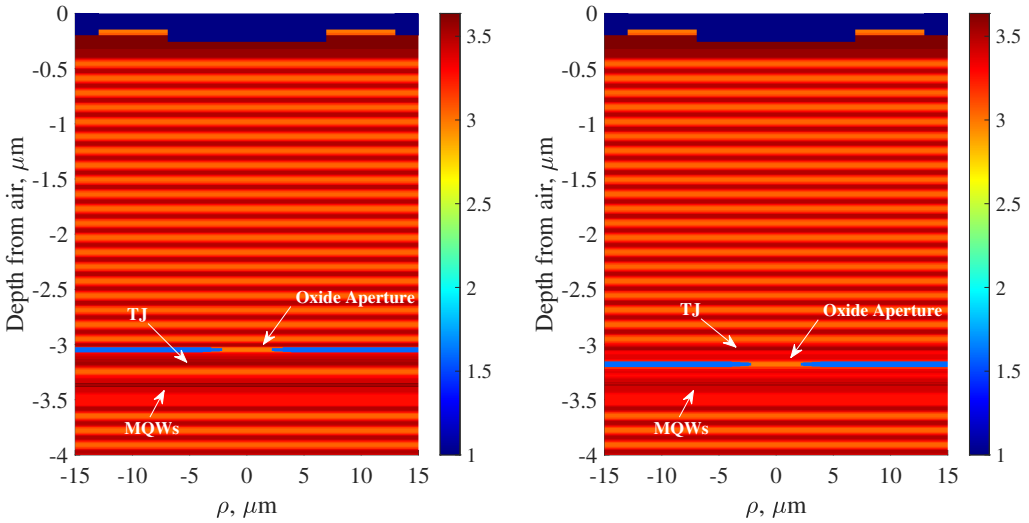

(a) Oxide **above** the TJ (A-TJ-VCSEL). (b) Oxide **below** the TJ (B-TJ-VCSEL).

Fig. 5.1 Refractive index profiles of the oxide-confined TJ-VCSELs, from the topmost bottom DBR layers to the output facet. The radially graded oxide aperture is surrounded by the oxidized region (light blue). In the two configurations, oxide aperture and TJ positions are switched, to place both in SW nodes.

5.1 Oxide-confined TJ-VCSEL

Oxide-confined TJ-VCSELs configuration relies on the presence of the oxide aperture for confinement purposes, with same diameter of the reference *pin* VCSEL. Keeping the TJ-VCSEL design as similar as possible to the reference device allows a direct and detailed comparison of the two hole injection schemes (from *p*-DBR or from TJ). The great advantage of such an approach is the technological compatibility with state-of-the-art VCSEL growing techniques. In fact, the only relevant difference between a *pin* and a TJ device would be the different dopant species (Te instead of Si) needed to reach high doping levels required in the n^{++} TJ side. Nevertheless, the TJ layers would extend radially across the whole VCSEL mesa, meaning that an oxide-confined TJ-VCSEL would still suffer of the technological limitations from the aluminum wet oxidation process. The TJ-VCSELs mesa has the same radius of the reference VCSEL, namely 13 μm, that is technologically required to reach the quasi-AlAs layers to be oxidized. In the end, the mesa is passivated with an insulator to reduce the related parasitic capacitance.

Within a design of this kind, particular attention must be devoted to the position of the oxide aperture, that has the same features described for the reference *pin* VCSEL. Surely, it must be inserted in the outcoupling mirror, in proximity of the active region [68]. Nevertheless, it could be still placed either above or below the TJ, that in turn has to be placed in a SW node above the AR for the reasons explained in section 4.1. In Figures 5.1, two alternatives configurations are sketched in terms of refractive index two-dimensional profiles. Notice that the substrate and the majority of the bottom DBR are not showed here, as they are identical. The relevant difference lies in the reciprocal position of oxide aperture and TJ. In fact, both require to be placed in the closest SW node (minimum) with respect to the AR. When the oxide aperture is placed **above** the TJ, the latter lies in the first node and the oxide is grown in the very next one (see Fig. 5.1a), hereinafter referred to as **A-TJ-VCSEL**. Conversely, in case of oxide aperture **below** the TJ (between the latter and the AR), the position of the two elements is switched (see Fig. 5.1b), hereinafter referred to as **B-TJ-VCSEL**. This simultaneously guarantees a reduction of the FCA losses introduced by the tunnel junction, and a weak transverse mode guiding, ensured by the oxide aperture in a SW node [151, 152].

5.1.1 Assessment of oxide and TJ reciprocal position

The TJ-VCSEL structures simulated in this section embed the same TJ discussed in Section 4.1. The benefits provided by a TJ-VCSEL, such as the removal of two pairs from the top DBR to match the gain at threshold and the top DBR doping switching, are indeed preserved also in a 3D framework. The comparisons are realized adopting a spatial grid as similar as possible to the reference structure, that is modified the least possible in the two TJ-VCSELs. The radial mesh has the same number of points; longitudinally, slight differences only arise in the proximity of TJ and oxide aperture. VENUS settings and material parameters are never changed across the simulations. This is the only chance to ensure a fair comparison between the two injections techniques.

Let's start from the static electrical characteristics at room temperature of Fig. 5.2, to identify the best TJ-VCSEL design. The *IV* computed by VENUS are reported as continuous lines in Fig. 5.2a. Red dots come from measurements provided by University of Ulm on the reference *pin* VCSEL: VENUS results on this structure are in great accordance with them. These are compared to our two oxide-confined

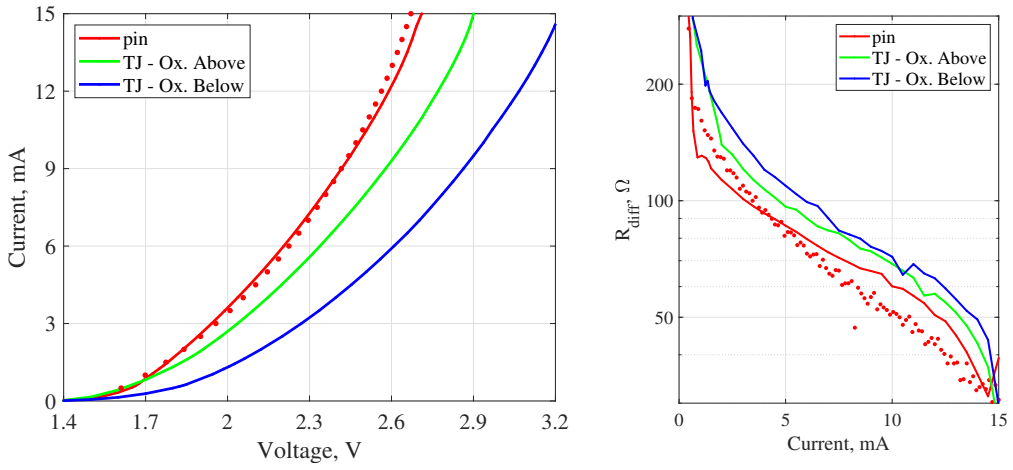

(a) *IV* (b) Differential resistance

Fig. 5.2 Static electrical *IV* characteristics (**a**) and corresponding differential resistances (**b**) at 20°C, of reference *pin* (red line) and oxide-confined TJ-VCSELs (green: A-TJ; blue: B-TJ) from VENUS. Reference VCSEL experimental results are marked as red dots.

TJ-VCSELs. In green we denote the A-TJ-VCSEL, whereas blue curves denote the B-TJ-VCSEL. The latter result confirm D1ANA predictions presented in Fig. 4.5a. In fact, the introduction of a planar TJ causes a voltage penalty. What D1ANA could not grasp is that it depends on the TJ position. From the differential resistance $R_{\text{diff}} = dV/dI$ curves in Fig. 5.2b, R_{diff} at 5 mA increases from 85 Ω for the *pin* to $R_{\text{diff}} = 95\,\Omega$ in the A-TJ-VCSEL and 110 Ω in the B-TJ-VCSEL. Going up in current the discrepancies reduce, with *pin* VCSEL always favored in the whole bias window.

Our physics-based in-house solver allows to go deep into the details of each device operation, and explain the differences between the tested devices. In Figures 5.3, V_{TJ} is reported as a function of the VCSEL radius (Fig. 5.3a) at different current values, and as a function of current (Fig. 5.3b), at different radial cuts. These include a central cut, the oxide edge radius $\rho_{\text{ox}} = 2.175\,\mu$m, the overall mesa $\rho_{\text{mesa}} = 13\,\mu$m, and some radii in between. In the simulated bias range, V_{TJ} is comprised between 0 and 0.7 V. Solid lines correspond to the A-TJ-VCSEL. At both 1 and 10 mA, V_{TJ} is smaller for $\rho < \rho_{\text{ox}}$ with respect to the B-TJ-VCSEL (dashed lines). From ρ_{ox} to ρ_{mesa}, V_{TJ} decreases less steeply, and sustains greater tunneling currents. As a consequence, current confinement worsens. TJ position determines the overall *IV*. Qualitatively, this can be grasped from the arrow (whose normalized length is proportional to the current intensity in that mesh point) plots shown in Fig. 5.4, where the

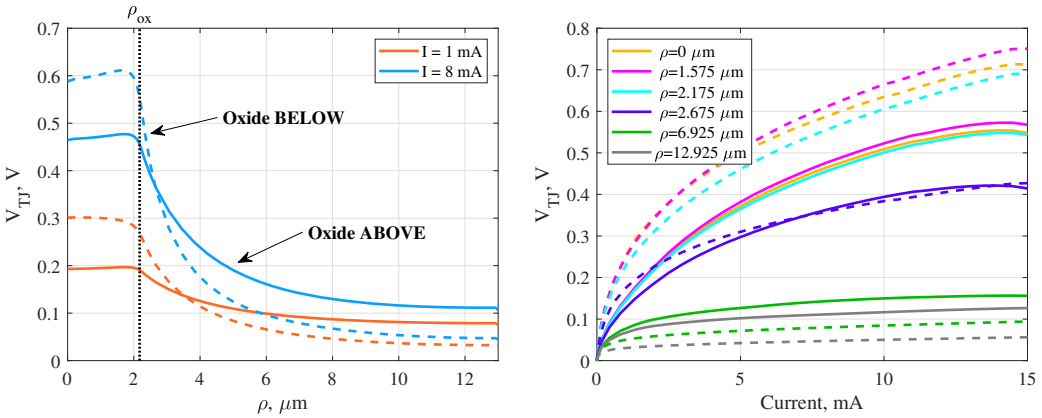

(a) $V_{TJ}(\rho)$ at different currents.

(b) $V_{TJ}(I)$ at different ρ.

Fig. 5.3 TJ voltage drop V_{TJ} as a function of (**a**) radius ρ and (**b**) current. Solid lines: A-TJ-VCSEL; dashed lines: B-TJ-VCSEL.

flow of current densities is superimposed to the 2D VCSEL scheme, at a bias current of 4 mA. Notice that, in the *pin* VCSEL in Fig. 5.4a, above oxide and AR (denoted as red and light blue blocks, respectively) the overall current density is dominated by *p*-current (represented in red), as injection is demanded to hole transport across a *p*-DBR. Quantitatively, at the same bias point we check in Fig. 5.4b that the sum of radial integral of the electron and hole current densities is conserved along the longitudinal direction of the VCSELs and continuity equations are satisfied. The "exchange" of carrier current density in the light blue rectangle is due to the strong radiative recombination in the QWs. On the other hand, as remarked several times throughout the thesis, the TJ (yellow rectangles in Figures 5.4c–5.4e) injects holes into the cavity through tunneling, allowing to use a *n*-DBR as outcoupling mirror. When the oxide is placed below the TJ (see Figures 5.4e and 5.4f), the VCSEL has a configuration similar to its *pin* counterpart. In fact, electrons from the top contact reach the planar TJ and are "converted" into holes. Thus, current crowding is still experienced by holes, just like in *pin*. As a consequence, the electrical penalty in the *IV* is almost equal to the voltage drop across the TJ itself, as predicted by D1ANA. Conversely, when oxide and TJ position is switched in the A-TJ-VCSEL (Fig. 5.4c), electron current is confined by the aperture. After having overcome it (see the blue arrows pointing toward left), electrons reach the TJ, where the aforementioned doping level induces a relevant diffusion current that makes the blue arrows change their orientation. Current spreading increases below the oxide, counteracting the

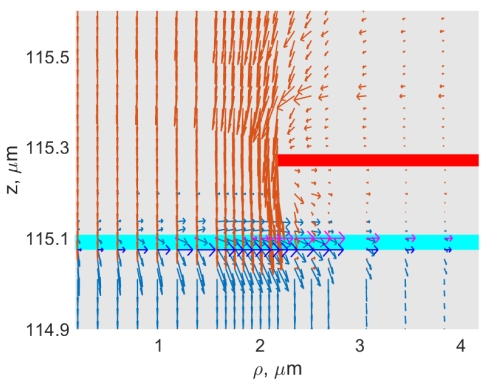

(a) Reference *pin* VCSEL

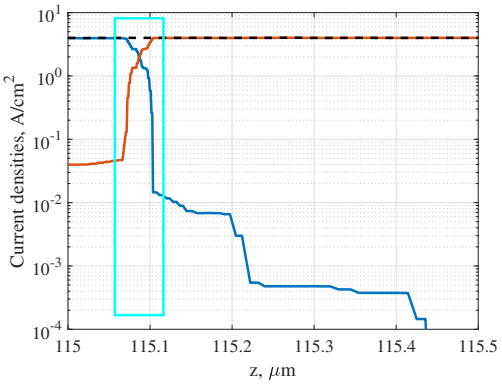

(b)

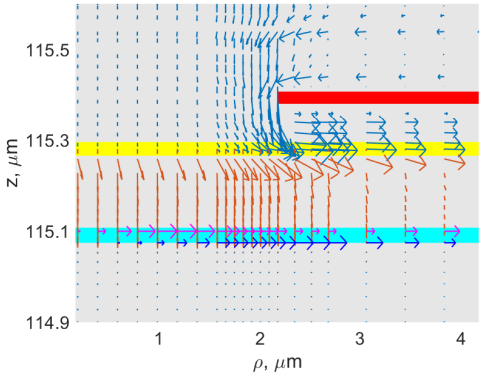

(c) Oxide aperture **above** the TJ

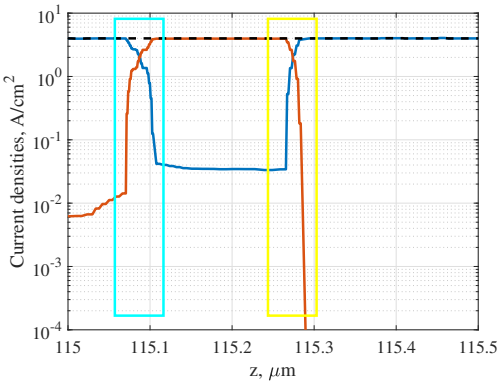

(d)

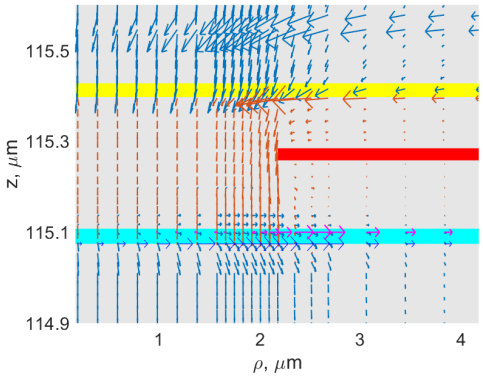

(e) Oxide aperture **below** the TJ

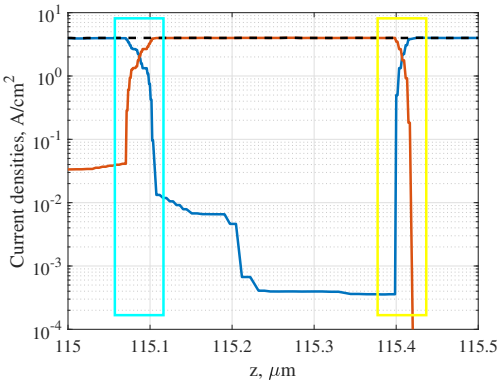

(f)

Fig. 5.4 Electron (blue) and hole (red) current densities in *pin* (**a-b**), A-TJ-VCSEL (**c-d**) and B-TJ-VCSEL (**e-f**), at injection current 4 mA. (**a-c-e**): carrier current densities arrow plots to grasp qualitatively the flow direction. The length of each arrow is proportional to the current intensity in that mesh node. (**b-d-f**): corresponding radial integrals, as functions of the longitudinal direction z. Black dotted line is their sum. Light blue regions: AR; yellow: TJ; red: oxide aperture.

electrical confinement. The impact of this difference will be assessed during the presentation of the optical characteristics.

Before discussing the *LI* curves reported in Fig. 5.5, let's remark once again that these simulations are performed assuming an ideal circular shape both for the oxide aperture and for the top annular contact, even though actual devices can show slightly rhomboidal shapes [153], that affect the polarization features of the output beam. Furthermore, the investigated VCSELs do not include any grating. This means that an investigation on the polarization is not needed, and thus VELM is run in its scalar version, allowing a faster simulation runtime without losing any relevant detail. The LP notation is used to denote the sustained modes: LP_{01} for the fundamental, Gaussian-like mode; LP_{02} for the second radial mode with no azimuthal variations; LP_{11} for the first-order mode. In Fig. 5.5, these are reported as $\circ$, $*$ and $\triangledown$, respectively. In the reference VCSEL, a threshold current of $I_{th} \approx 500\,\mu A$ is predicted. Fundamental LP_{01} mode is the first to reach lasing condition. At 2 mA, LP_{11} turns on and becomes dominant at 4 mA. Only when the VCSEL is entering in its roll-over condition, LP_{02} becomes to lase at 11 mA. Such a modal stability is ensured by the position of the oxide, in the first SW node after the AR. The overall output optical power, reported as a continuous red line, is in good accordance with experimental result (red dots). The maximum total output power $P_{max} = 3.3$ mW is reached at a bias current slightly smaller than 10 mA.

Similar considerations can be associated to the B-TJ-VCSEL *LI* curve, represented in blue. As discussed for the electrical characteristics, the oxide confinement is introduced in a similar position, inducing a modal separation closer to the reference case: the threshold of all the modes is comparable. Nevertheless, it is worth noticing that LP_{11} (blue $\triangledown$) mode now lases earlier in current (3.5 mA instead of 4 mA), thus slightly narrowing the monomodal bias window. However, the thinner outcoupling mirror improves the optical slope dL/dI, that brings P_{max} to 6 mW at a similar current than in the *pin* VCSEL. P_{max} is almost doubled. Also, in the B-TJ-VCSEL LP_{02} (blue $*$) reaches threshold 1 mA later than in the *pin* device, and just after the begin of the thermal roll-over. As a final remark, the overall optical characteristics computed by VENUS for B-TJ-VCSEL are compatible with D1ANA results (Fig. 4.5b) taking in mind that VELM in 1D does not include any transverse mode feature, becoming three times lighter.

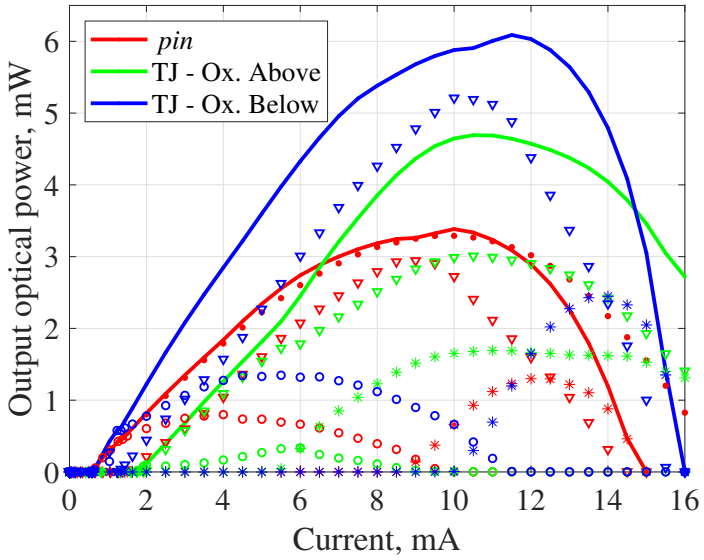

Fig. 5.5 Static optical *LI* characteristics at 20°C, of reference *pin* VCSEL (red line) and TJ-VCSELs (green: A-TJ-VCSEL; blue: B-TJ-VCSEL) with VENUS. Reference VCSEL experimental results are marked with red dots. LP_{01}, LP_{11} and LP_{02} modes are referred to as $\circ$, $\triangledown$ and $*$ symbols, respectively.

The accordance between VENUS and D1ANA fails when oxide aperture and TJ position is switched from B to A, resulting in different performances, as shown by the green curves. The optical threshold current, which coincides with the LP_{01} threshold in *pin* and B-TJ-VCSEL, now refers to LP_{11}, reported as green $\triangledown$. Moreover, it triples (1.7 mA). The dL/dI slope remains similar to the B-TJ-VCSEL, but P_{max} is reduced to 4.7 mA at 10.5 mA. As highlighted by the symbols, the A-TJ-VCSEL has a completely different modal distribution. The fundamental mode struggles to reach threshold, and it can just deliver a power smaller than 0.5 mW (see the green $\circ$). Conversely, the threshold current of LP_{02} (green $*$) is diminished to 5.5 mA, from 11 mA of the B-TJ-VCSEL. Even though it never becomes dominant, it increases the overall dL/dI and provides a robust contribution to the *LI*, also beyond thermal roll-over, suggesting that thermal guiding improves the LP_{02} mode for a wide current range. The assessment of its optical power performance with a substantial reduction of P_{max} compared to B-TJ-VCSEL, indicates that the oxide aperture should not be placed above the TJ.

In the followings, we provide the reasons of that different optical behavior, strictly related to the previously discussed electrical properties. From these, it is easier to

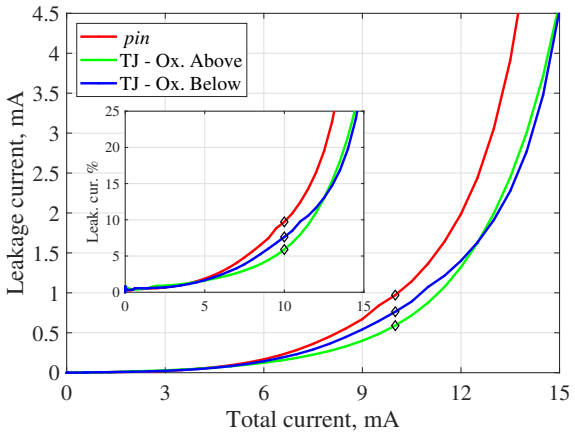

Fig. 5.6 *pin* and TJ-VCSELs leakage currents as functions of injection current (inset: corresponding percentage). Black diamonds denote the P_{max} current.

understand and evaluate the hole injection efficiency, the leakage from the MQW region, and the modal features. Let's first consider the charge injection efficiency inside the MQW. This is related to the leakage current I_{leak}, which is extracted at any injection current from the current density profiles (similar to the ones reported in Figures 5.4b, 5.4d, 5.4f), at the AR extreme points. Ideally, each current density should be converted into the other through stimulated recombination into the MQW, resulting in zero leakage current condition. In real devices, thermal effects have a strong impact on material parameters, including the band diagrams, which makes I_{leak} drift away from ideality. In Fig. 5.6, I_{leak} is reported as a function of the injection current for the three VCSELs under investigation. It remains below 1 mA up to the maximum power current, *i.e.*, 10 mA marked as black diamonds in the plots. After that point, when thermal roll-over becomes strong, I_{leak} rises up to 4.5 mA as the VCSELs approach their turn-off. The impact of leakage is also shown as a percentage of the total injection current in the inset of Fig. 5.6, highlighting that it displays comparable values between *pin* (in red) and TJ-VCSELs (in green and blue). Its weight remains below 10 % up to thermal roll-over, and it rumps up to 25 % in the reference device and to slightly lower values at equal currents in the TJ-VCSELs.

Spatial hole-burning governs the mode competition, as a lower hole mobility determines the radial gain profile inside the QWs. Each optical transverse mode radially digs the carrier distribution in a different way, depending on its shape. If the hole re-filling by QW diffusion is not fast enough, higher order modes begin to prevail as the overall flowing current increases. This mechanism depends on the

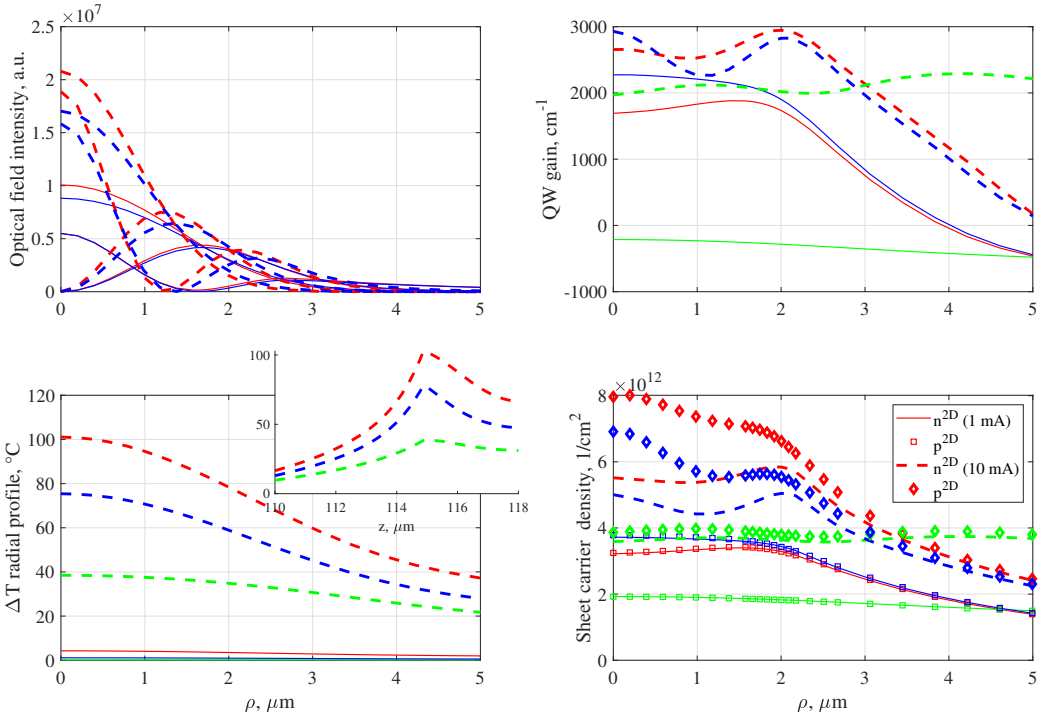

Fig. 5.7 Modal distribution assessment, with quantities taken at 1 (thin continuous lines) and 10 mA (thick dashed lines) for *pin* (in red), A-TJ- (in green) and B-TJ-VCSEL (in blue). Top left: transverse optical fields intensity. Top right: radial QW gain. Bottom left: radial temperature profiles (inset: longitudinal variation in the AR proximity). Bottom right: sheet carrier densities.

2D continuity equations (2.4)–(2.5), and particularly on the adopted mobility of carriers. In the presented results, QW mobility is assumed to be less than halved with respect to the bulk value [67]. The role of spatial hole-burning and thermal effects as fundamental mechanisms selecting the dominant lasing mode is discussed in Figure 5.7. These are only some of a plethora of quantities that can be extracted from the thermal, optical and electrical solver for *pin* (in red) and TJ-VCSELs (in green and blue). In particular, the ones reported here are radial cuts in the central QW, at 1 and 10 mA. The top left curves show the optical field intensity transverse profiles of LP_{01}, LP_{11} and LP_{02} modes for *pin* (in red) and B-TJ-VCSEL (in blue). A-TJ-VCSEL profiles do not add relevant information. Continuous thin lines are the intensities at 1 mA, thick dashed lines are taken at 10 mA, where peak output power is reached. The only relevant difference here resides in higher and more peaks of the *pin* VCSEL (red curves). At the same values of currents, in the bottom left figure the radial profile of temperature is reported, while the longitudinal temperature variation at 10 mA is shown in the inset, where the substrate is excluded. The squeezed transverse field profiles towards the central axis in the top right figure are explained by stronger thermal lensing effect at high injection, responsible of a significant radial-dependent refractive index variation. In the *pin* device, higher temperatures are reached at equal current values. This induces a strong lateral index guiding that impacts on the optical fields, alongside the QW carrier distribution. The latter has a varying shape, that depends on the injection condition: see the bottom right plot of Fig. 5.7. Here, the sheet carrier densities are reported (see legend for further details). These populations are the ones actually recombining through stimulated emission (2.18) in the MQW and "consumed" during the lasing operation. This plot explains the modal distribution of the three devices. Notice that at 1 mA, electrons and holes reach same levels and are superimposed. Furthermore, both *pin* and B-TJ-VCSEL 2D carriers are large up to the oxide aperture radius of 2.175 μm, and decrease for larger radii: electrical confinement is realized. Conversely, the A-TJ-VCSEL displays a halved level of carriers: threshold condition has not been reached yet. This is reflected in the QW gain profiles, in the top right plot: the negative gain of the A-TJ-VCSEL means that the material is not pumped enough and is still absorbing. Moving to 10 mA (thicker symbols and lines), densities of *pin* and B-TJ-VCSEL holes (red and blue diamonds) have been dug by LP_{11} mode, that being peaked at 1 μm "consumes" carriers around that radius. Electrons (red and blue dashed lines) have a flatter profile, due to their greater mobility, which leads a faster redistribution.

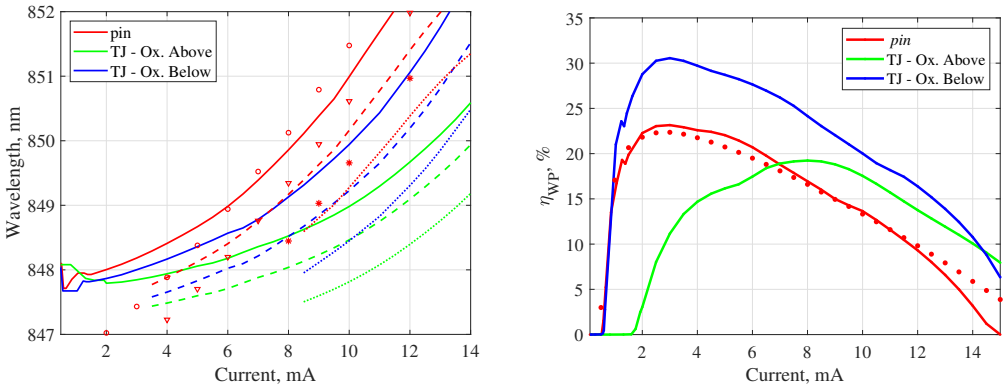

(a) $\lambda(I)$ (b) External wall-plug efficiency

Fig. 5.8 Wavelength red shift and η_{WP} vs current at 20°C, computed for the *pin* (red line) and TJ-VCSELs (green: A-TJ-VCSEL; blue: B-TJ-VCSEL). Reference VCSEL experimental results are reported in red with the same symbols used in Fig. 5.5. LP_{01}, LP_{11} and LP_{02} from VENUS are denoted by continuous, dashed and dotted lines, respectively.

This translates in a more concentrated carriers distribution at the edge of the oxide aperture and at the VCSEL axis. The gain profiles makes this concept even clearer. Therefore, LP_{02} starts lasing, as its field intensity is zero where LP_{11} is peaked, and has a peak where LP_{11} is minimum. Meanwhile, also the A-TJ-VCSEL reaches the level of carriers required to lase. Despite this, from their radial distribution we can notice that current confinement is not good in A-TJ-VCSEL. This can be explained by referring to the arrow plots discussed in Fig. 5.4c. The presence of the TJ below the oxide aperture lets the carrier diffuse stronger in the radial direction. In this configuration the oxide aperture just provides the optical confinement, not enough to select the fundamental mode as the emitting one.

Other relevant figures of merits are the wavelength red shift, *i.e.*, the VCSEL "thermometer", and the wall-plug efficiency as functions of the driving currents, grouped together in Fig. 5.8. The output wavelength λ of each mode reported in Fig. 5.8a has different slopes in the three structures. The measurements on the reference VCSELs are denoted by the same symbols used in Fig. 5.5. Relating these curves to (3.1), we conclude that the overall inner temperature increase is more pronounced in the *pin* VCSEL. This is further confirmed by the bottom left curves of Fig. 5.7. As discussed in the 1D preliminary treatment of Section 3.1, this is related to the reduced Joule effect and FCA losses in the TJ-VCSEL. In fact, equal temperature increase occurs at a higher output optical power with respect to the *pin*

counterpart. This explains the reduced λ of the B-TJ-VCSEL (blue curves), but not the A-TJ-VCSEL, in green, whose wavelength red-shifts for less than 2 nm in the operating region. This is related to the smaller output optical powers below 6 mA (that affects the relevance of FCA losses), and to the reduced Joule effect, which is limited with respect to the *pin* for a twofold reason. First, the adoption of a top *n*-DBR (that is the effect also observed in the B-TJ-VCSEL); then, the current spreading below the oxide, that makes the thermal source less focused radially and mitigates self-heating. For what concerns the external efficiency curves in Fig. 5.8b, it is worth noticing that the B-TJ-VCSEL shows a comparable improvement with respect to the predictions of D1ANA that were sketched in Fig. 4.7b. Also there a η_{WP} exceeding 30% is computed, at 20°C. This gives further support to our hypotheses regarding the validity of our reduced dimensionality solver. More importantly, the improved efficiency of the B-TJ-VCSEL demonstrated also by VENUS confirms that the observed electrical penalty induced by the TJ is overcome by the benefits introduced in the optical characteristics. Nevertheless, this is not applicable to the A-TJ-VCSEL (in green). The postponed threshold lets the corresponding η_{WP} curve reach its peak only at 8 mA, staying below 20%. Notice that above 7 mA, it overtakes the commercial device, and gets closer to its dual design. Also this curve induces to discard the A-TJ-VCSEL.

5.2 Harsh temperature analysis

The room temperature analysis of the previous section demonstrates that the preferred design has the oxide in the same position of the *pin* VCSEL, with the TJ just above it (B-TJ-VCSEL). As mentioned in the introduction of the thesis, VCSELs operating in harsh environments such as server racks often work at ambient temperatures of 80°C. Here we compare a set of simulations performed on the B-TJ-VCSEL, at heat sink temperatures higher than 20°C, with the reference device. The results obtained from VENUS about the *pin* VCSEL are presented in Figures 5.9 as solid lines, at 50, 80 and 110°C. These show good agreement with the experimental results, again reported as dots.

As already appreciated from the room temperature simulations in Fig. 5.2a, the B-TJ-VCSEL (dashed lines) introduces the usual electrical penalty at all temperatures (see Section 5.1.1): the corresponding *IV* are reported in Fig. 5.9a. The *LI*

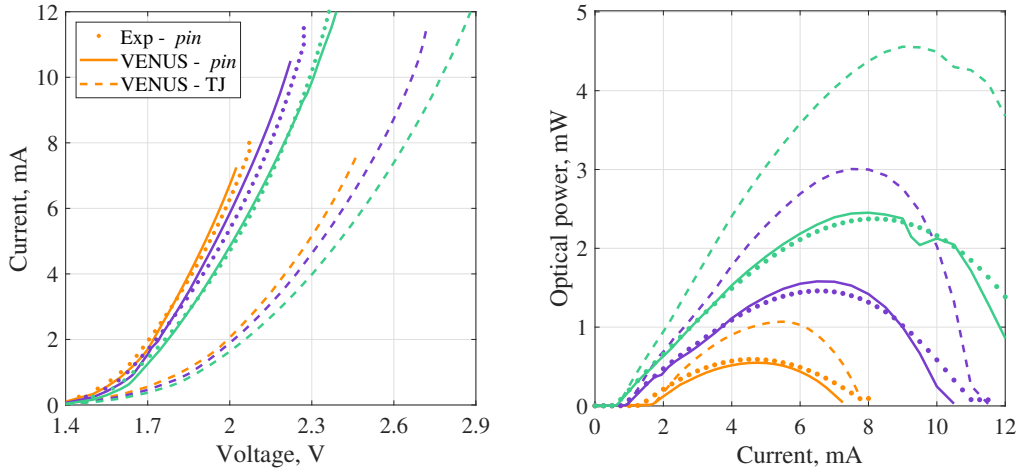

(a) *IV* (b) *LI*

(c) $\lambda(I)$ (d) External wall-plug efficiency

Fig. 5.9 (**a**) *IV*, (**b**) *LI*, (**c**) wavelength, and (**d**) WPE at 50 (green), 80 (purple), 110°C (yellow), computed for *pin* VCSEL (solid lines) and B-TJ-VCSELs (dashed lines). Reference VCSEL experimental results are marked with dots.

characteristics of the TJ-VCSEL in Fig. 5.9b predict an almost doubling trend for $P_{\max}$, at all the temperatures: from 2.4 to 4.5 mW at 50°C (green curves), from 1.6 to 3 mW at 80°C (purple curves), and from 0.5 to 1 mW at 110°C (yellow curves). At the investigated temperatures, the peak power is reached at similar currents by the two devices (5, 7, 8 mA, respectively). Let's now consider the "thermometer" of the VCSEL: the emission wavelength as a function of bias current. In Fig. 5.9c, the curves corresponding to LP_{01} are represented. Experimental data are satisfactorily reproduced by VENUS, meaning that the $dn/dT = 2.35\,\mathrm{K}^{-1}$ used in our simulations predicts well the actual device inner temperature rise. Of course, for the B-TJ-VCSEL the same value is adopted. At low currents, *i.e.*, low temperatures, wavelength initially shows similar values with respect to the *pin* case. As already observed at 20°C in Fig. 5.8a, at increasing bias currents the emission wavelength remains below the *pin* VCSEL results, in particular at 50 and 80°C. At 110° the inner temperature rise is slightly stronger, inducing a more intense red shift (yellow curves). Overall, the B-TJ-VCSEL provides an improved thermal behavior, for the reasons discussed at the end of Section 5.1.1. Also the wall-plug efficiency curves, displayed in Fig. 5.9d, demonstrate that the TJ-VCSEL has an improved WPE across the whole bias window, as predicted by D1ANA. At 50°C (green curves), the WPE peak moves from 20% to 26%; at 80°C, $\eta_{WP}^{\mathrm{TJ}} \approx 20\% > \eta_{WP}^{pin} \approx 15\%$; at 110°C, $\eta_{WP}^{\mathrm{TJ}} \approx 10\% > \eta_{WP}^{pin} \approx 7\%$. The peaks are reached at equal current values, proving that the discussed voltage penalty is compensated by the *LI* enhancement. Again, the macroscopic results at different ambient temperatures push in favor of placing the oxide as close as possible to the AR.

5.3 Insights on TJ heating

Accounting properly for the TJ heating sources is not trivial. As mentioned, carrier transport across the TJ is dominated by ballistic BTBT, which occurs within few nanometers. In principle, ballistic transport by definition is not affected by any scattering event, that would make carrier relax through carrier-phonon processes. This is indeed true also in TJs. Nevertheless, one should consider that the TJ is not a standalone element, being sandwiched between a number of layers, where transport is surely not ballistic. According to NEGF approach, the extreme points of the TJ can be seen as contacts in quasi-equilibrium condition, and the related

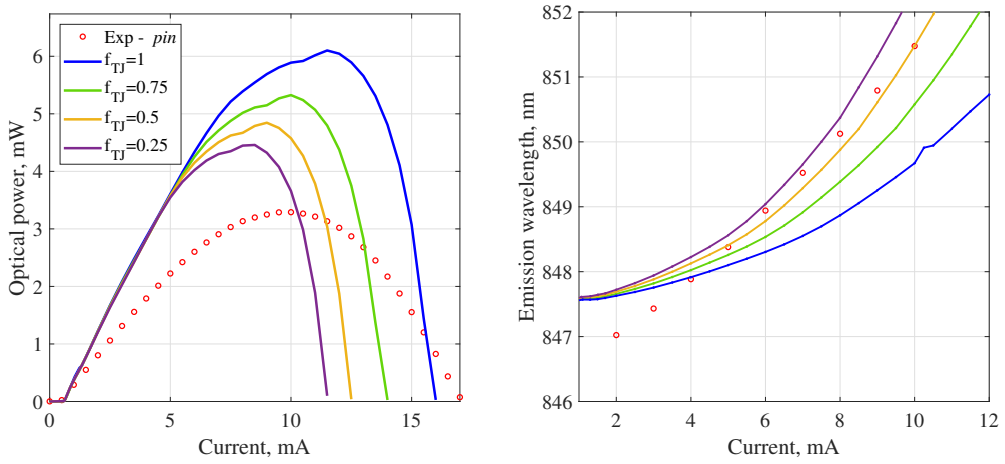

(a) *LI* (b) $\lambda(I)$

Fig. 5.10 Impact of f_{TJ} on optical characteristics (**a**) and wavelength red shift (**b**) of the B-TJ-VCSEL, at 20°C. Reference VCSEL experimental results are marked with red dots.

boundary problem is treated through the boundary self-energies (see Section 2.1.2). What matters here is how carriers behave once they undergo BTBT and reach the TJ boundaries, entering the bulk domains. Due to the lack of scattering, one may assume that electrons tunneling from VB to CB retain their energies. In our semiclassical approach, the carrier energy is assumed to be the edge of the corresponding band. As depicted in the electron spectral current of Fig. 2.4a, NEGF accounts for tunneling in a wider energy spectrum. The red band in that figure shows how electrons of different energies contribute to the overall interband current. Therefore, after tunneling, each carrier population thermalizes in the bulk layers, losing an energy related to the energy gap of the layers surrounding the TJ, which is then converted into heat. A fitting factor f_{TJ} can be associated to this conversion.

To explain where f_{TJ} is introduced, we need to remind the discussion at the end of Section 2.2, about f_{corr}. In fact, this method works well in the *pin* VCSEL, where carrier transport relies on the DD model. However, the presence of the TJ introduces the voltage drop V_{TJ} diffusely discussed in this Chapter. Hence, P_{elec} should increase by a factor close to $I \cdot V_{\mathrm{TJ}}$. The ballistic nature of BTBT does not consent to introduce a thermal source related to the external G_{BTBT}, similar to the other recombinations terms in (2.19). According to (2.24) right hand side, f_{corr} is expected to grow as well. Consequently, in the case of TJ-VCSELs, one may think to reformulate the

expression at right in (2.24) by introducing f_{TJ}:

$$f_{\mathrm{corr}} = \frac{\left(P_{\mathrm{elec}} - P_{\mathrm{elec}}^{TJ}\right) - P_{\mathrm{opt}}}{P_{\mathrm{therm}}} = \frac{\left(I \cdot (V - f_{\mathrm{TJ}} V_{\mathrm{TJ}})\right) - P_{\mathrm{opt}}}{P_{\mathrm{therm}}} \tag{5.1}$$

The final step regarding f_{TJ} is related to the aforementioned thermalization of carriers in the TJ proximity. In the TJ nodes, P_{therm} is retrieved as:

$$P_{\mathrm{therm}}^{\mathrm{TJ}} = \int_0^{L_{\mathrm{TJ}}} \int_0^{\rho_{\mathrm{mesa}}} Q_{\mathrm{TJ}}(z,\rho)\rho d\rho dz \tag{5.2}$$

where $Q_{\mathrm{TJ}}(z,\rho)$ are the heat sources in the TJ related to Joule effect and non-radiative recombination processes, which enter into the heat equation. A smart choice is to treat the heat sources in that region as a separate block. $Q_{\mathrm{TJ}}(z,\rho)$ can be replaced by a simplified expression, where f_{TJ} can be inserted:

$$Q_{\mathrm{TJ}}(\rho) \approx (1 - f_{\mathrm{TJ}}) \frac{V_{\mathrm{TJ}}(\rho) \cdot J_{\mathrm{TJ}}(\rho)}{L_{\mathrm{TJ}}} \tag{5.3}$$

that is constant along z, just like G_{BTBT}. Radially, Q_{TJ} depends on ρ, as V_{TJ} is not constant, as seen in Fig. 5.3. In conclusion, using equations (5.1) and (5.3), the TJ contribution to the overall self-heating is investigated. In Fig. 5.10, a campaign of simulations with f_{TJ} varied from 1 to 0.25 is presented. When $f_{\mathrm{TJ}} = 1$, $Q_{\mathrm{TJ}} = 0$ and any contribution from the TJ is removed from the electrical power. Conversely, for $f_{\mathrm{TJ}} = 0$, P_{elec} returns to its original expression $I \cdot V$ and the TJ sources are computed as $Q_{\mathrm{TJ}}(\rho) = V_{\mathrm{TJ}}(\rho) \cdot J_{\mathrm{TJ}}(\rho)/L_{\mathrm{TJ}}$. From the *LI* curves in Fig. 5.10a, P_{max} and thermal roll-over are reached earlier when f_{TJ} decreases. In fact, the correction factor (2.24) increases accordingly. Again, one should keep in mind that f_{corr} acts on the sources across the whole device: if the source at one point are significantly underestimated, it heavily modifies the thermal behavior of the simulated VCSEL. As a consequence, also the $d\lambda/dI$ of Fig. 5.10b are affected. In future, we plan to investigate this issue more in details, to address in a formal way the TJ heat sources problem.

This chapter demonstrates that VENUS is capable of dealing with AlGaAs oxide-confined TJ-VCSELs, and also confirms the validity of D1ANA presented in the previous chapters. In Section 5.1.1, the inclusion of all the radial features is required to highlights that the reciprocal position of oxide aperture and TJ is crucial to the TJ-VCSEL operation. A preferred design is determined, resembling the *pin* VCSEL confinement scheme. Some insights about the current flow and

the voltage drops inside the investigated devices is shown to help the discussion. Optical features, carrier distribution and thermal profiles are presented to understand the modal competition. In Section 5.2, static simulations at heat sink temperatures ranging from 50 to 110°C compare the electrical and optical characteristics to the *pin* VCSELs, confirming quantitatively the results coming from D1ANA of Chapter 4. Section 5.3 deals with a discussion about the heating sources inside the TJ, which still lack of a proper modeling.

Chapter 6

Conclusions

The purpose of this thesis is to pave the way for next generation VCSELs, able to overcome the state-of-the-art of near-IR oxide-confined AlGaAs devices. The *pin* VCSELs market pervasion makes the main producers hesitating with revolutionary designs, as they require extensive prototyping campaigns. In the view of preventing the consequent time and money waste, this work is purely based on a TCAD approach, that adopts two existing in-house solvers (D1ANA and VENUS), with different degrees of numerical efficiency and predictivity. Both are quantum-corrected drift-diffusion solvers, specifically tailored for VCSELs simulations, capable of dealing self-consistently also with the entangled optical and thermal problems.

The power of VENUS and D1ANA resides in being physics-based tools. They allow to go beyond the phenomenological rate-equations model, a very popular tool to interpret results of any laser, which fails to predict with accuracy the effectiveness of new concepts. Our approach gives a wide range of advantages with respect to commercial software. In fact, other than extracting the relevant macroscopic figures of merits, D1ANA and VENUS give us access to all the inner simulated quantities during VCSELs operation, such as energy band diagrams, carrier densities, current distributions, optical field profiles. These are fundamental to explain in details the obtained results, and to address issues and evaluate merits of the proposed ideas. Furthermore, being in-house solvers, we have full control over all the material parameters, models and structure details, so that modifications of them are immediately available. A detailed discussion of the equation implemented in our solvers has been provided in Chapter 2, and also in Appendix A.

In this work, we assess the advantages coming by hole injection in the AR through quantum BTBT across a TJ in AlGaAs VCSELs. TJ-VCSELs are technological enablers for III-nitride VCSELs for UV emission and InP and GaSb-based systems for mid-infrared applications. In these devices, TJ mitigates the issues related to tricky acceptor doping in nitride alloys and transverse confinement of current and optical field, that is not feasible through wet oxidation of Al-rich layers. Therefore, the question we tried to answer is: does the benefits provided by the TJ apply also to near-IR AlGaAs VCSELs? To this aim, we started from a fully characterized state-of-the-art *pin* VCSEL, already investigated in deep by VENUS, and we inserted a planar TJ in the AR proximity, modifying the least possible the *pin* VCSEL layers. Electrical and optical confinement is still demanded to the oxide aperture. Our idea is to compare the performances of holes injection by a TJ that allows to replace the top *p*-DBR with an *n*-DBR. This should lower the losses related to FCA and Joule effects, induced by the *p*-doping. However, the TJ treatment cannot rely on the semiclassical QCDD exploited for the reference VCSEL. Therefore, a genuine quantum approach is introduced to model properly interband tunneling across the TJ: namely the non-equilibrium Green's function (NEGF), applied just to the TJ region. From NEGF, we extract an interband current, that is treated as a further quantum correction, to the same extent as the corrections dealing with the QWs in the already existing QCDD framework. In particular, NEGF current is converted into a net generation process G_{BTBT}, introduced in the TJ nodes alongside the already implemented GR rates. The insights of our NEGF-DD model are provided in section 2.1.2 and in Appendix B.

The complexity of the procedure requires an intermediate step, before its full deployment in VENUS. The idea is to start from D1ANA, a 1D version of the DD model used in VENUS, extend it with the optical and thermal models, and then calibrate its parameters to reproduce VENUS results. The downscaling process of VENUS to D1ANA, a 1D version inherently quicker and less predictive, with the corresponding set of fitting parameters, is described throughout Chapter 3. The static figures of merits extracted by D1ANA are shown in the same chapter and compared to experimental results. D1ANA is then used for a fast parametric study of cavity detuning and DBR thickness to define an optimal design at 20 and 80°C. The QCDD 1D model is extended to perform also small-signal analysis. This is validated with the results extracted from Sentaurus Device on a *pin* junction. Then, the VCSEL amplitude modulation response is compared to experiments.

Chapter 4 illustrates the modifications realized on the reference *pin* device to obtain a test TJ-VCSEL. In this chapter, we use D1ANA to introduce the tunneling generation rate G_{BTBT} for the first time in our solver. The novel NEGF-DD approach is exploited on the test TJ-VCSEL structure. The comparison with the reference VCSEL are discussed. D1ANA predicts a significant improvement of the optical characteristics, despite a worse differential resistance due to the TJ presence. The benefits of the TJ-VCSEL are underlined by the enhanced WPEs at all the investigated temperatures. A parametric simulation similar to the *pin* concludes the chapter.

Finally, in Chapter 5, VENUS is extended with the aforementioned NEGF treatment of the TJ. Here we analyze two distinct configurations, with oxide aperture and TJ reciprocal positions switched, to investigate the effect of the TJ strong doping on the electrical confinement. The design with the oxide closer to the AR reveals to be optimal (B-TJ-VCSEL). The extracted static and electrical characteristics confirm D1ANA results presented in the previous chapter. A wide temperature range is explored, to assess the performance improvements of the TJ-VCSEL also in harsh environments, which are the more interesting ones from the application standpoint. Several internal parameters are shown and discussed, to understand in deep the differences between *pin* and TJ-VCSELs. The different internal heating and corresponding wavelength red shift predicted by VENUS for the TJ-VCSEL, with respect to D1ANA, is addressed at the end of the chapter, where the heat sources in the TJ are also discussed.

To conclude, the most important goals reached within the thesis are:

- Extension of an existing one dimensional carrier transport solver D1ANA, based on DD, to multiphysics (electro-thermal-optical) and multiscale (quantum corrections) simulations (Chapter 3)
- Calibration of D1ANA on a fully characterized *pin* AlGaAs VCSELs through a set of identified trimming parameters (Chapter 3)
- Introduction of small-signal analysis in D1ANA (Chapter 3)
- TJ operation modeling through a NEGF approach (Chapter 2 and 4)
- Introduction of a self-consistent NEGF-DD scheme to treat AlGaAs TJ-VCSELs in D1ANA (Chapter 4)

- Inclusion of the NEGF-DD scheme in VENUS: lateral features neglected or mimicked in D1ANA are explored into details for two TJ-VCSELs with varying reciprocal position of TJ and oxide aperture (Chapter 5)

- Definition of an optimal TJ-VCSEL design, with TJ placed above the oxide aperture, ensuring a current confinement comparable to the *pin* device. The TJ induces an electrical penalty, related to the voltage drop across it and to its position. Nonetheless, the results are promising: optical characteristics are enhanced at temperatures from 20 to 110°C. The maximum output powers are almost doubled, while keeping the threshold current and the modal spectrum unchanged, thanks to lower self-heating and top DBR doping conversion. In future, we will also investigate the small-signal features of TJ-VCSELs, following the approach presented in Section 3.2 (Chapter 5)

This thesis represents the beginning of the work on AlGaAs TJ-VCSELs. In fact, ongoing efforts are now focused to the assessment of buried TJ-VCSELs, where the TJ is radially defined by a photolithographic process. In this way, electrical confinement relies on the low-resistance path within the TJ radius, laterally surrounded by a blocking region. Optical confinement is obtained through successive epitaxial regrowth above the buried TJ, that determines a central refractive index step [20]. The clear advantage of BTJ-VCSELs is that lithographic processing gives the ability to reach smaller sizes that are hard to achieve with high reliability for oxide-confined VCSELs. The demonstration of BTJ-VCSELs with good scaling properties could be an important step toward producing ultra-small size laser diodes with good size control, manufacturability and high die yield, not to mention the possibility of lithographically controlling polarization in the same fabrication step used to form the TJ [21].

Appendix A

Drift-diffusion model insights

In this appendix, some of the main QCDD model ingredients are extensively presented. The goal here is to show in more details the Fermi-Dirac statistics, the dopants incomplete ionization and the implemented generation/recombination models for bulk processes.

A.1 Fermi-Dirac Statistics

As mentioned, all the carrier densities included in the Poisson equation (2.1) are treated with the Fermi-Dirac statistics. Hence, densities are described by the Fermi distribution:

$$n = N_{\mathrm{C}} \mathscr{F}_{\frac{1}{2}} \left(\frac{E_{Fn} - E_{\mathrm{C}}}{k_{\mathrm{B}} T} \right) \tag{A.1}$$

$$p = N_{\mathrm{V}} \mathscr{F}_{\frac{1}{2}} \left(\frac{E_{\mathrm{V}} - E_{Fp}}{k_{\mathrm{B}} T} \right) \tag{A.2}$$

where $\mathscr{F}_{\frac{1}{2}}$ is the "Fermi function", integral of order $1/2$ of the Fermi-Dirac statistics [154, 155] computed on the difference between quasi-Fermi levels $E_{Fn,p}$ and conduction and valence band edges $E_{\mathrm{C,V}}$, divided by the thermal voltage $V_T = k_{\mathrm{B}} T$. $N_{\mathrm{C,V}}$ is the conduction and valence band effective density of states.

Conduction and valence band edges are computed from the potential ϕ:

$$E_{\mathrm{C}} = -\phi + \frac{E_g}{2} - \frac{V_T}{2} \log \left(\frac{N_{\mathrm{V}}}{N_{\mathrm{C}}} \right) + \phi_r, \quad E_{\mathrm{V}} = E_{\mathrm{C}} - E_g \tag{A.3}$$

involving also a reference potential ϕ_r and the energy band gap E_g. Eq. (A.1)–(A.2) link carrier densities to potential, and the following inverse formulas ensure consistency:

$$E_{Fn} = E_{\mathrm{C}} + V_T \mathscr{F}^{-1}\left(\frac{n}{N_{\mathrm{C}}}\right) \tag{A.4}$$

$$E_{Fp} = E_{\mathrm{V}} - V_T \mathscr{F}^{-1}\left(\frac{p}{N_{\mathrm{V}}}\right) \tag{A.5}$$

Maxwell-Boltzmann Statistics is not adopted in VENUS and D1ANA because the non-degeneracy of semiconductor ($n < N_{\mathrm{C}}$, $p < N_{\mathrm{V}}$) cannot be assumed in these devices. At equilibrium, the *mass action law* holds true:

$$np = n_i^2 \tag{A.6}$$

where n_i represents the intrinsic carrier concentration of the semiconductor.

A.2 Incomplete ionization

Doping is obtained by introducing atoms into semiconductor vacancy defects. Ideally, all the implanted or diffused dopants species occupy a vacancy and provide effectively the extra charges that enhance the semiconductor electrical conductivity. This is the full ionization of dopants, where $N_{\mathrm{D}}^{+} = N_{\mathrm{D}}$ and $N_{\mathrm{A}}^{-} = N_{\mathrm{A}}$. Besides the technological limitations that will not be discussed here, from the physics standpoint not all the dopants are activated once they enter the semiconductor. A realistic model should account for the incomplete ionization of dopants, to consider that implanted/diffused atoms must generate a *substitutional* impurity to be effective for doping purposes.

A simple way to model the incomplete ionization is to introduce the donor and acceptor activation energies ΔE_{D} and ΔE_{A}, whose values are material and dopant dependent [156]. In this view, the effective doping levels are given by:

$$N_{\mathrm{D}}^{+} = \frac{N_{\mathrm{D}}}{1 + \frac{2}{n_1}} \tag{A.7}$$

$$N_{\mathrm{A}}^{-} = \frac{N_{\mathrm{A}}}{1 + \frac{4}{p_1}} \tag{A.8}$$

where n_1 and p_1 are defined as:

$$n_1 = N_{\mathrm{C}} \exp\left(-\frac{\Delta E_{\mathrm{D}}}{k_{\mathrm{B}} T}\right) \tag{A.9}$$

$$p_1 = N_{\mathrm{V}} \exp\left(-\frac{\Delta E_{\mathrm{A}}}{k_{\mathrm{B}} T}\right) \tag{A.10}$$

Both the dopants activation energies and the thermal voltage $V_T = k_{\mathrm{B}} T$ are on the order of magnitude of few tens meV.

A.3 Generation-Recombination processes

A brief recap of the bulk GR processes included in our QCDD model is presented here. The BTBT rate is not described as it is extensively discussed in the next Appendix. The net recombination rate $U_{n/p}$ comes from the difference between generation and recombination rates, and it approximates the collision term of the Boltzmann transport equation (BTE). Clearly, a generation event accounts for the creation of a *e-h* pair, *i.e.*, when an electron (hole) is promoted from the valence (conduction) band to the conduction (valence) band, starting to play a role in the transport mechanisms. Conversely, recombination is the reverse process: an electron (hole) in the conduction (valence) band fills an empty state in the valence (conduction) band. As a consequence, the e-h pair is annihilated and energy is released in the form of phonons or photons. Both these process can be phonon-assisted (thermal), photon-assisted (optical) or assisted by other electrons or holes (Auger). Furthermore, GR transitions can be either interband (direct) or assisted by intermediate trap levels in the forbidden band (indirect or Shockley-Read-Hall mechanisms). In stationary conditions $U_{\mathrm{n}} = U_{\mathrm{p}}$, while the same does always not hold true in case of time-varying conditions. The main GR mechanisms that occur in bulk regions of the device are spontaneous emission, Auger, and Shockley-Read-Hall (SRH), each of them characterized by a specific rate U_{sp}, U_{Aug}, U_{SRH} [157] in turn included in (2.2)-(2.5).

In a QW, similar processes occur, even though with different time constants, and with the addition of the stimulated emission in case of lasers. The formulas presented in the following sections are written for bulk continuity equations. The same expression can be used for bound case, keeping in mind that a division by the

QW width is required:

$$U_{n/p}^{2D} = U_{n/p}^{3D} \cdot W_{QW} \tag{A.11}$$

A.3.1 Spontaneous emission

Spontaneous emission is the radiative recombination actually exploited to generate photons in a semiconductor. In a VCSEL, the QWs in the active region are designed to obtain a high rate of spontaneous emission: electrons and holes are injected in the QWs to radiatively recombine, transferring their energy to a photon, whose energy depends on the energy band diagram of the quantum well itself. In this way, gain is obtained and lasing condition is reached when current injection is strong enough. Spontaneous emission rate is modeled by the following:

$$U_{sp} = B^{rad}(np - n_i^2) \tag{A.12}$$

where B^{rad} is the radiative recombination coefficient (cm^3/s) and n_i is the intrinsic carrier concentration of the semiconductor; n and p are the usual carrier densities. Of course, at equilibrium conditions U_{sp} is equal to zero, due to (A.6).

A.3.2 Auger recombination

Radiative recombination has an unwanted competitor when a device works in high injection condition: the Auger recombination. This is an electron or hole-assisted (three particles) process which involves an *e-h* pair and an additional electron or hole. The expression describing it is:

$$U_{Aug} = (C_n^{Aug} n + C_p^{Aug} p)(np - n_i^2) \tag{A.13}$$

where C_n^{Aug} and C_p^{Aug} are the Auger coefficients for electrons and holes (cm^6/s). It is worth noticing that (A.13) takes into account the third particle by including the Auger coefficients which in turn are multiplied by the populations ($\propto n^2 p$ or np^2). In fact, the Auger recombination rate proportionality on the carrier densities is related to both their collisions and their energies, since they supply some energy to the process. Notice that the inverse of the Auger recombination is the generation by impact ionization, and is not taken into account in VENUS/D1ANA simulations.

A.3.3 Shockley-Read-Hall recombination

As mentioned, SRH recombination deals with the trap-assisted processes. These are possible when a semiconductor has some traps that introduce a discrete energy level in the forbidden band. The latter increases the probability of a interband transition, because the energetic "jump" a carrier has to face becomes smaller. The net trap-assisted recombination rate can be expressed as follows:

$$U_{\mathrm{SRH}} = \frac{np - n_i^2}{\tau_p^{\mathrm{SRH}}(n + n_t) + \tau_n^{\mathrm{SRH}}(p + p_t)} \tag{A.14}$$

where τ_n and τ_n are the average carrier lifetimes, independent from doping level; $n_t = n_i \exp(E_{\mathrm{trap}}/k_{\mathrm{B}}T)$, and $p_t = n_i \exp(E_{\mathrm{trap}}/k_{\mathrm{B}}T)$ are the trap level population densities (E_{trap} is the difference in energy between the trap level and the intrinsic level; particularly important are the recombination centers, *i.e.*, midgap traps that maximize the SRH rate).

Appendix B

NEGF-DD implementation

The implementation of the NEGF-DD scheme requires a proper treatment of the result coming from NEGF. First, putting together formulas (2.11) and (2.12), the following expression for the generation rate due to BTBT is obtained:

$$G_{\mathrm{BTBT}}(z,V) = \frac{1}{q}\frac{J_{\mathrm{TJ}}(V)}{L_{\mathrm{TJ}}} = \begin{cases} \dfrac{1}{qL_{\mathrm{TJ}}} 10^{\left(\beta_0+\beta_1 V+\beta_2 V^2+\beta_3 V^3+\ldots\right)}, & \text{if } z \in \mathrm{TJ} \\ 0, & \text{elsewhere} \end{cases} \tag{B.1}$$

with β_i coefficient of the exponential fit and L_{TJ} longitudinal extension of the TJ. This expression gives $G_{\mathrm{BTBT}}(V)$ a rectangular shape similar to the sketch shown Fig. B.1, equal to 0 outside the TJ region investigated with NEGF. Despite this, the rate is treated similarly to the other GR mechanisms described in Appendix A. It is to be remarked that inside the TJ nodes z(TJ), the value of the rate only depends on the voltage drop $V = V_{\mathrm{TJ}}$ across the TJ itself. In our DD solver, V_{TJ} is defined as the difference between the quasi-Fermi levels at the extreme points of the TJ domain:

$$V_{\mathrm{TJ}} = E_{Fp}(z_L) - E_{Fn}(z_R) \tag{B.2}$$

where $z_L = z(\mathrm{TJ}_L)$ and $z_R = z(\mathrm{TJ}_R)$ denote the two extreme sides (p^{++} and n^{++}, respectively) of the TJ. Therefore, the NEGF-DD scheme is realized by extracting a $G_{\mathrm{BTBT}}(V)$ fitted from the NEGF interband current with (B.1), adopting the quasi-Fermi levels difference as DD interpolating quantity for bridging quantum and semiclassical simulations.

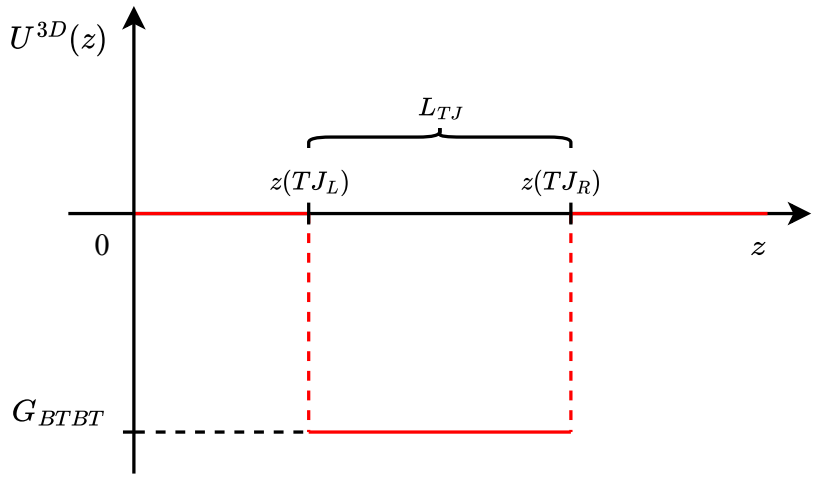

Fig. B.1 Sketch of $G_{\mathrm{BTBT}}(V)$ shape. The TJ extends longitudinally from $z(\mathrm{TJ}_L)$ to $z(\mathrm{TJ}_R)$, and is L_{TJ} long. $G_{\mathrm{BTBT}}(V)$ is negative, denoting a net generation rate; outside the TJ nodes $G_{\mathrm{BTBT}}(V) = 0$.

B.1 BTBT rate derivatives

NEGF-DD self-consistency and convergence of the Newton's scheme are ultimately ensured by computing the derivatives of $G_{\mathrm{BTBT}}(V)$ with respect to the DD unknowns (ϕ, n, p), namely $\partial G_{\mathrm{BTBT}}/\partial\phi$, $\partial G_{\mathrm{BTBT}}/\partial n$, $\partial G_{\mathrm{BTBT}}/\partial p$ and assembling them properly inside the *Jacobian* matrix presented in Section 2.2. The easiest choice to compute them is through the chain rule:

$$\frac{\partial G_{\mathrm{BTBT}}}{\partial \phi, n, p} = \frac{\partial G_{\mathrm{BTBT}}}{\partial V}\frac{\partial V}{\partial \phi, n, p} \tag{B.3}$$

Let's start from the $\partial/\partial V$ term of (B.3) right hand side, which is shared by all the derivatives. Keeping in mind (B.1), an equivalent expression is given by:

$$\frac{\partial G_{\mathrm{BTBT}}}{\partial V} = \frac{1}{qL_{\mathrm{TJ}}}\frac{\partial J_{\mathrm{TJ}}(V)}{\partial V} \tag{B.4}$$

where $\partial J_{\mathrm{TJ}}/\partial V$ is analytically computed from (2.12):

$$\frac{\partial J_{\mathrm{TJ}}(V)}{\partial V} = \ln(10)\cdot 10^{\left(\beta_0+\beta_1 V+\beta_2 V^2+\beta_3 V^3+\ldots\right)}\left(\beta_1+2\beta_2 V+3\beta_3 V^2+\ldots\right) \tag{B.5}$$

Then, the computation of the partial derivatives of V in (B.3) completes the terms inserted in $\underline{\underline{J}}$:

- Derivative with respect to the potential ϕ:

$$\frac{\partial V}{\partial \phi} = \frac{\partial V}{\partial E_{Fn,p}} \frac{\partial E_{Fn,p}}{\partial \phi} = \begin{cases} +1, & \text{if } E_{Fn} \\ -1, & \text{if } E_{Fp} \end{cases} \tag{B.6}$$

  recalling (B.2) and that Fermi-Dirac statistics is adopted in our solvers, as shown in Appendix A, with quasi-Fermi levels computed according to equations (A.4)–(A.5).

- Derivative with respect to the electron density n:

$$\frac{\partial V}{\partial n} = \left(\frac{\partial n}{\partial V}\right)^{-1} = \left(\frac{\partial n}{\partial E_{Fn}}\right)^{-1} = \frac{1}{\frac{\partial n}{\partial E_{Fn}}} = \frac{k_\mathrm{B}T}{N_\mathrm{C}} \frac{1}{\mathscr{F}_{\frac{1}{2}}\left(\frac{E_{Fn}-E_\mathrm{C}}{k_\mathrm{B}T}\right)} \tag{B.7}$$

  Recalling again (B.2) and that Fermi-Dirac Statistics (A.1) is adopted for n.

- Derivative with respect to the hole density p, similar to electron case:

$$\frac{\partial V}{\partial p} = \left(\frac{\partial p}{\partial V}\right)^{-1} = \left(\frac{\partial p}{\partial E_{Fp}}\right)^{-1} = \frac{1}{\frac{\partial p}{\partial E_{Fp}}} = \frac{k_\mathrm{B}T}{N_\mathrm{V}} \frac{1}{\mathscr{F}_{\frac{1}{2}}\left(\frac{E_\mathrm{V}-E_{Fp}}{k_\mathrm{B}T}\right)} \tag{B.8}$$

  that exploits (A.2) to evaluate p.

Eventually, the expressions just derived for (B.3) must be assembled in the correct positions of the *Jacobian* matrix. A proper filling of $\underline{\underline{J}}$ becomes easier by realizing that G_BTBT magnitude only depends on the quasi-Fermi levels at the extreme points of the TJ, as shown by (B.2). As a consequence, the derivatives (B.3) are assembled only in the columns of $\underline{\underline{J}}$ corresponding to the ϕ, n and p mesh nodes of z_L and z_R. Since G_BTBT enters in the bulk continuity equations as a semiclassical GR mechanism, only the $\underline{\underline{J}}$ rows corresponding to them are affected. In Fig. B.2, the map of $\underline{\underline{J}}$ non-zero entries is reported again, with a focus on the terms related to G_BTBT (highlighted by the blue circles). Notice that they are out of the main diagonals, because the BTBT rate does not depend on the inner TJ nodes, but only on its extreme points.

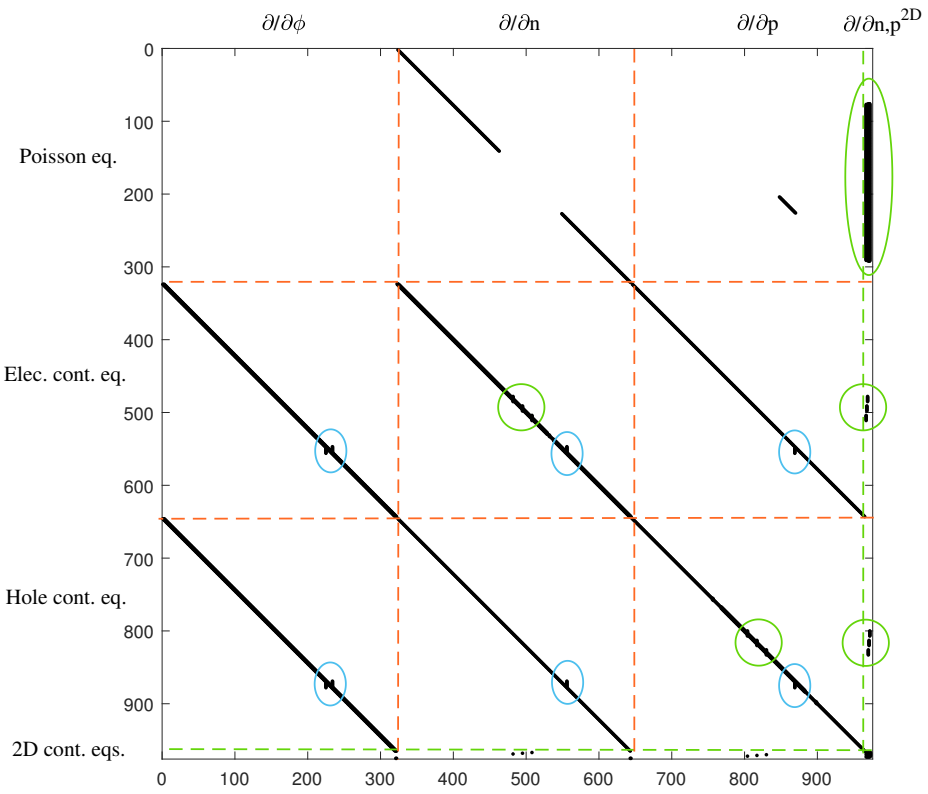

Fig. B.2 Jacobian matrix non-zero entries position, already presented in Fig. 2.7. Here BTBT rate derivatives are assembled inside the regions highlighted by the blue circles.

References

[1] R. Puerta, M. Agustin, L. Chorchos, J. Tonski, J.-R. Kropp, N. Ledentsov, V. A. Shchukin, N. N. Ledentsov, R. Henker, I. Tafur Monroy, J. J. Vegas Olmos, and J. P. Turkiewicz. 107.5 Gb/s 850 nm multi- and single-mode VCSEL transmission over 10 and 100 m of multi-mode fiber. In *2016 Optical Fiber Communications Conference and Exhibition (OFC)*, pages 1–3, 2016.

[2] H. Soda, K.-I. Iga, C. Kitahara, and Y. Suematsu. GaInAsP/InP surface emitting injection lasers. *Japan. J. Appl. Phys.*, 18(12):2329, 1979.

[3] J. A. Tatum, D. Gazula, L. A. Graham, J. K. Guenter, R. H. Johnson, J. King, C. Kocot, G. D. Landry, I. Lyubomirsky, A. N. MacInnes, E. M. Shaw, K. Balemarthy, R. Shubochkin, D. Vaidya, M. Yan, and F. Tang. VCSEL-based interconnects for current and future data centers. *J. Lightwave Technol.*, 33(4):727–732, 2015.

[4] C.-T. Tsai, C.-Y. Peng, C.-Y. Wu, S.-F. Leong, H.-Y. Kao, H.-Y. Wang, Y.-W. Chen, Z.-K. Weng, Y.-C. Chi, H.-C. Kuo, J.J. Huang, T.-C. Lee, T.-T. Shih, J.-J. Jou, W.-H. Cheng, C.-H. Wu, and G.-R. Lin. Multi-mode VCSEL chip with high-indium-density InGaAs/AlGaAs quantum-well pairs for QAM-OFDM in multi-mode fiber. *IEEE J. Select. Topics Quantum Electron.*, 53(4):1–8, 2017.

[5] N. Ledentsov Jr., M. Agustin, L. Chorchos, N. N. Ledentsov, and J. P. Turkiewicz. 25.78 Gbit/s data transmission over 2 km multi-mode-fibre with 850 and 910 nm single-mode VCSELs and a commercial quad small form-factor pluggable transceiver. *Electron. Lett.*, 54(12):774–775, 2018.

[6] G. Kanakis, N. Iliadis, W. Soenen, B. Moeneclaey, N. Argyris, D. Kalavrouziotis, S. Spiga, P. Bakopoulos, and H. Avramopoulos. High-speed VCSEL-based transceiver for 200 GbE short-reach intra-datacenter optical interconnects. *MDPI Appl. Sci.*, 9(12), 2019.

[7] A. Larsson, J. S. Gustavsson, A. Fülöp, E. Haglund, E. P. Haglund, and A. Kelkkanen. The future of VCSELs: Dynamics and speed limitations. In *2020 IEEE Photonics Conference (IPC)*, pages 1–2, 2020.

[8] N. N. Ledentsov, O. Yu. Makarov, V. A. Shchukin, V. P. Kalosha, N. Ledentsov, L. Chrochos, M. Bou Sanayeh, and J. P. Turkiewicz. High speed vcsel technology and applications. *J. Lightwave Technol.*, 40(6):1749–1763, 2022.

[9] R. Michalzik, editor. *VCSELs: Fundamentals, Technology and Applications of Vertical-Cavity Surface-Emitting Lasers*. Springer-Verlag, Berlin, 2013.

[10] D. L. Perry. Low-loss multilayer dielectric mirrors. *Appl. Opt.*, 4(8):987–991, Aug 1965.

[11] N. Nishiyama, C. Caneau, B. Hall, G. Guryanov, M. H. Hu, X.S. Liu, M.J. Li, R. Bhat, and C. Zah. Long-wavelength Vertical-Cavity Surface-Emitting Lasers on InP with lattice matched AlGaInAs-InP DBR grown by MOCVD. *IEEE J. Select. Topics Quantum Electron.*, 11-5:990 – 998, 10 2005.

[12] C. Zhang, R. ElAfandy, and J. Han. Distributed bragg reflectors for GaN-based Vertical-Cavity Surface-Emitting Lasers. *MDPI Appl. Sci.*, 9(8), 2019.

[13] R. P. Schneider and J. A. Lott. InAIP/InAlGaP distributed Bragg reflectors for visible Vertical-Cavity Surface-Emitting Lasers. *Appl. Phys. Lett.*, 62(22):2748–2750, 1993.

[14] M. Ogura, T. Hata, N.J. Kawai, and T. Yao. GaAs/$Al_xGa_{1-x}As$ multilayer reflector for Surface-Emitting Lasers diode. *Japan. J. Appl. Phys.*, 22(2A):L112, feb 1983.

[15] K. L. Lear, K. D. Choquette, R.P. Schneider, S. P. Kilcoyne, and K. M. Geib. Selectively oxidised vertical cavity surface emitting lasers with 50% power conversion efficiency. *Electron. Lett.*, 31:208–209(1), February 1995.

[16] J. R. Kropp, G. Steinle, G. Schäfer, V. A. Shchukin, N. N. Ledentsov, J. P. Turkiewicz, and M. Zoldak. Accelerated aging of 28 $Gb{\cdot}s^{-1}$ 850 nm Vertical-Cavity Surface-Emitting Laser with multiple thick oxide apertures. *Semiconductor Sci. Technol.*, 30(4):045001, February 2015.

[17] F.A.I. Chaqmaqchee and J.A. Lott. Impact of oxide aperture diameter on optical output power, spectral emission, and bandwidth for 980 nm VCSELs. *OSA Continuum*, 3(9):2602–2613, 2020.

[18] L. Esaki. New phenomenon in narrow germanium *p-n* junctions. *Phys. Rev.*, 109(2):603–604, January 1958.

[19] L. Esaki. Long journey into tunneling. *Science*, 183(4130):1149–1155, 1974.

[20] J. Ahn, D. Lu, and D. G. Deppe. All-epitaxial, lithographically defined, current- and mode-confined vertical-cavity surface-emitting laser based on selective interfacial Fermi-level pinning. *Appl. Phys. Lett.*, 86(2):021106, January 2005.

[21] A. Demir, G. Zhao, S. Freisem, X. Liu, and D. Deppe. Scaling properties of lithographic VCSELs. *Proceedings of SPIE - The International Society for Optical Engineering*, 7952, 02 2011.

[22] M. Ortsiefer, R. Shau, G. Böhm, F. Köhler, G. Abstreiter, and M.-C. Amann. Low-resistance InGa(Al)As tunnel junctions for long wavelength vertical-cavity surface-emitting lasers. *Japan. J. Appl. Phys.*, 39(Part 1, No. 4A):1727–1729, apr 2000.

[23] W. Hofmann, M. Muller, G. Bohm, M. Ortsiefer, and M.-C. Amann. 1.55-μm VCSEL with enhanced modulation bandwidth and temperature range. *IEEE Photon. Technol. Lett.*, 21(13):923–925, 2009.

[24] J. M. Lamy, S. Boyer-Richard, C. Levallois, C. Paranthoën, H. Foillot, N. Chevalier, A. Le Corre, and S. Loualiche. Design of an InGaAs/InP 1.55 μm electrically pumped VCSEL. *Opt. Quantum Electron.*, 40:1193–1998, June 2009.

[25] A. Bachmann, Kaveh K.-S., S. Arafin, and M.-C. Amann. GaSb-based VCSEL with buried tunnel junction for emission around 2.3 μm. *IEEE J. Select. Topics Quantum Electron.*, 15:933–940, 2009.

[26] A. Andrejew, S. Sprengel, and M.-C. Amann. GaSb-based vertical-cavity surface-emitting lasers with an emission wavelength at 3 μm. *Opt. Lett.*, 41(12):2799–2802, 2016.

[27] G. K. Veerabathran, S. Sprengel, A. Andrejew, and M.-C. Amann. Room-temperature vertical-cavity surface-emitting lasers at 4 μm with GaSb-based type-II quantum wells. *Appl. Phys. Lett.*, 110:071104–1–5, 2017.

[28] A. Haug. Free-carrier absorption in semiconductor lasers. *SST*, 7(3):373, mar 1992.

[29] J. Ch. Garcia, E. Rosencher, Ph. Collot, N. Laurent, J. L. Guyaux, B. Vinter, and J. Nagle. Epitaxially stacked lasers with Esaki junctions: A bipolar cascade laser. *APL*, 71(26):3752–3754, 12 1997.

[30] J. K. Kim, S. Nakagawa, E. Hall, and L. A. Coldren. Near-room-temperature continuous-wave operation of multiple-active-region 1.55 *mu*m vertical-cavity lasers with high differential efficiency. *APL*, 77(20):3137–3139, 11 2000.

[31] J. T. Leonard, E. C. Young, B. P. Yonkee, D. A. Cohen, T. Margalith, S. P. DenBaars, J. S. Speck, and S. Nakamura. Demonstration of a III-nitride vertical-cavity surface-emitting laser with a III-nitride tunnel junction intracavity contact. *Appl. Phys. Lett.*, 107(9):091105, 2015.

[32] S.-G. Lee, C. A. Forman, J. Kearns, J. T. Leonard, D. A. Cohen, S. Nakamura, and S. P. Den-Baars. Demonstration of GaN-based vertical-cavity surface-emitting lasers with buried tunnel junction contacts. *Opt. Express*, 27(22):31621–31628, October 2019.

[33] Y. Zhang, Zane J.-E., and S. Rajan. Recent progress of tunnel junction-based ultra-violet light emitting diodes. *Japan. J. Appl. Phys.*, 58:SC0805, May 2019.

[34] M. Żak, G. Muziol, H. Turski, M. Siekacz, K. Nowakowski-Szkudlarek, A. Feduniewicz-Żmuda, M. Chlipała, A. Lachowski, and C. Skierbiszewski. Tunnel junctions with a doped (In,Ga)N quantum well for vertical integration of III-nitride optoelectronic devices. *Phys. Rev. Appl.*, 15(2):024046, February 2021.

[35] G. Almuneau, R. Bossuyt, P. Collière, L. Bouscayrol, M. Condé, I. Suarez, V. Bardinal, and C. Fontaine. Real-time in situ monitoring of wet thermal oxidation for precise confinement in VCSELs. *Semiconductor Sci. Technol.*, 23(10):105021, sep 2008.

[36] W. Hofmann. High-speed buried tunnel junction vertical-cavity surface-emitting lasers. *IEEE Photon. J.*, 2(5):802–815, October 2010.

[37] G. Lafleur, G. Almuneau, A. Arnoult, H. Camon, and S. Calvez. Anisotropy in the wet thermal oxidation of AlGaAs: influence of process parameters. *Opt. Mater. Express*, 8(7):1788–1795, Jul 2018.

[38] X. Yang, M. Li, G. Zhao, Y. Zhang, S. Freisem, and D.G. Deppe. Oxide-free Vertical-Cavity Surface-Emitting Lasers with low junction temperature and high drive level. *Electron. Lett.*, 50(20):1474–1475, 2014.

[39] T. Knödl, R. Jager, M. Grabherr, R. King, M. Kicherer, M. Miller, F. Mederer, and K.J. Ebeling. CW room temperature operation of a diode cascade InGaAs-AlGaAs quantum well VCSEL. In *1999 IEEE LEOS Annual Meeting Conference Proceedings. LEOS'99. 12th Annual Meeting. IEEE Lasers and Electro-Optics Society 1999 Annual Meeting (Cat. No.99CH37009)*, volume 1, pages 143–144 vol.1, 1999.

[40] T. Knödl, M. Golling, A. Straub, and K. J. Ebeling. Multi-diode cascade VCSEL with 130% differential quantum efficiency at CW room temperature operation. *Electron. Lett.*, 37:31–33(2), January 2001.

[41] T. Knödl, R. Michalzik, M. Golling, and K.J. Ebeling. Current-spreading-induced bistability in bipolar cascade Vertical-Cavity Surface-Emitting Lasers. *Appl. Phys. Lett.*, 81(4):583–585, 2002.

[42] T. Knödl, M. Golling, A. Straub, R. Jager, R. Michalzik, and K.J. Ebeling. Multistage bipolar cascade Vertical-Cavity Surface-Emitting Lasers: theory and experiment. *IEEE J. Select. Topics Quantum Electron.*, 9(5):1406–1414, 2003.

[43] M. Dummer, K. Johnson, S. Rothwell, K. Tatah, and M. Hibbs-Brenner. The role of VCSELs in 3D sensing and LiDAR. In Henning Schröder and Ray T. Chen, editors, *Optical Interconnects XXI*, volume 11692, page 116920C. International Society for Optics and Photonics, SPIE, 2021.

[44] Guanzhong P., Meng X., Zhuangzhuang Z., Yun S., Jingtao Z., and Dexin W. High slope efficiency bipolar cascade 905 nm Vertical-Cavity Surface-Emitting Laser. *IEEE Electron Device Lett.*, 42(9):1342–1345, 2021.

[45] G. Zhao, J. Yang, E. Hegblom, A. Barve, B. Kesler, M. Tashima, Z. Bian, S. Xie, A. Robit, M. Peters, and J. Skidmore. Multi-junction VCSEL arrays with high performance and reliability for mobile and automotive 3D sensing applications. In Chun Lei and Kent D. Choquette, editors, *Vertical-Cavity Surface-Emitting Lasers XXV*, volume 11704. International Society for Optics and Photonics, SPIE, 2021.

[46] W. J. Siskaninetz, J. E. Ehret, J. D. Albrecht, R. G. Bedford, Jr. T. R. Nelson, and J. A. Lott. Gigahertz modulation of GaAs-based bipolar cascade vertical cavity surface-emitting lasers. *Opt. Lett.*, 32(2):136–138, Jan 2007.

[47] P. S. Wong, J. Yan, T. C. Wu, W. Kyi, J. Pao, and M. Riaziat. Tunnel junction 850-nm VCSEL for aperture uniformity and reliability. In Kent D. Choquette and Chun Lei, editors, *Vertical-Cavity Surface-Emitting Lasers XXI*, volume 10122, pages 72 – 76. International Society for Optics and Photonics, SPIE, 2017.

[48] H. Moench, M. Carpaij, P. Gerlach, S. Gronenborn, R. Gudde, J. Hellmig, J. Kolb, and A. van der Lee. VCSEL-based sensors for distance and velocity. In Kent D. Choquette and James K. Guenter, editors, *Vertical-Cavity Surface-Emitting Lasers XX*, volume 9766, page 97660A. International Society for Optics and Photonics, SPIE, 2016.

[49] S. Donati. Developing self-mixing interferometry for instrumentation and measurements. *Laser & Photon. Rev.*, 6(3):393–417, 2012.

[50] Y. L. Lim, R. Kliese, K. Bertling, K. Tanimizu, P. A. Jacobs, and A. D. Rakić. Self-mixing flow sensor using a monolithic vcsel array with parallel readout. *Opt. Express*, 18(11):11720–11727, May 2010.

[51] P.A. Porta, D.P. Curtin, and J.G. McInerney. Laser doppler velocimetry by optical self-mixing in vertical-cavity surface-emitting lasers. *IEEE Photon. Technol. Lett.*, 14(12):1719–1721, 2002.

[52] A. Quirce, P. Perez, A. Valle, L. Pesquera, I. Esquivias, K. Panajotov, and H. Thienpont. Free space ranging based on a chaotic long-wavelength VCSEL with optical feedback. In Bernd Witzigmann, Marek Osinski, Fritz Henneberger, and Yasuhiko Arakawa, editors, *Physics and Simulation of Optoelectronic Devices XXIII*, volume 9357, page 935703. International Society for Optics and Photonics, SPIE, 2015.

[53] M. Grabherr, R. King, R. Jäger, D. Wiedenmann, P. Gerlach, D. Duckeck, and C. Wimmer. Volume production of polarization controlled single-mode VCSELs. In Chun Lei and James K. Guenter, editors, *Vertical-Cavity Surface-Emitting Lasers XII*, volume 6908, page 690803. International Society for Optics and Photonics, SPIE, 2008.

[54] J.-F. Seurin, D. Zhou, G. Xu, A. Miglo, D. Li, T. Chen, B. Guo, and C. Ghosh. High-efficiency VCSEL arrays for illumination and sensing in consumer

applications. In Kent D. Choquette and James K. Guenter, editors, *Vertical-Cavity Surface-Emitting Lasers XX*, volume 9766, page 97660D. International Society for Optics and Photonics, SPIE, 2016.

[55] A. Breitbarth, T. Schardt, C. Kind, J. Brinkmann, P.-G. Dittrich, and G. Notni. Measurement accuracy and dependence on external influences of the iPhone X TrueDepth sensor. In Maik Rosenberger, Paul-Gerald Dittrich, and Bernhard Zagar, editors, *Photonics and Education in Measurement Science 2019*, volume 11144, page 1114407. International Society for Optics and Photonics, SPIE, 2019.

[56] D. K. Serkland, G. M. Peake, K. M. Geib, R. Lutwak, R. M. Garvey, M. Varghese, and M. Mescher. VCSELs for atomic clocks. In Chun Lei and Kent D. Choquette, editors, *Vertical-Cavity Surface-Emitting Lasers X*, volume 6132, page 613208. International Society for Optics and Photonics, SPIE, 2006.

[57] A. Lytkine, W. Jaeger, and J. Tulip. Multi-species gas detection with long-wavelength VCSEL. In Joachim Piprek, editor, *Physics and Applications of Optoelectronic Devices*, volume 5594, pages 155–163. International Society for Optics and Photonics, SPIE, 2004.

[58] S. Vasilchenko, M. Konefal, D. Mondelain, S. Kassi, P. Čermák, S. A. Tashkun, V. I. Perevalov, and A. Campargue. The co_2 absorption spectrum in the 2.3 μm transparency window by high sensitivity crds: (i) rovibrational lines. *J. Quant. Spectrosc. Radiat. Transf.*, 184:233–240, 2016.

[59] M. Ghysels, D. Mondelain, S. Kassi, A.V. Nikitin, M. Rey, and A. Campargue. The methane absorption spectrum near 1.73 μm (5695–5850 cm^{-1}): Empirical line lists at 80 k and 296 k and rovibrational assignments. *J. Quant. Spectrosc. Radiat. Transf.*, 213:169–177, 2018.

[60] C. Gierl, T. Gruendl, P. Debernardi, K. Zogal, C. Grasse, H. A. Davani, G. Böhm, S. Jatta, F. Küppers, P. Meißner, and M.-C. Amann. Surface micromachined tunable 1.55 μm-VCSEL with 102 nm continuous single-mode tuning. *Opt. Express*, 19(18):17336–17343, August 2011.

[61] P. Debernardi, A. Simaz, A. Tibaldi, B. Boisnard, T. Camps, F. Bertazzi, M. Goano, B. Reig, J.-B. Doucet, and V. Bardinal. Anisotropic transverse confinement design for electrically pumped 850 nm VCSELs tuned by an intra cavity liquid-crystal cell. *IEEE J. Select. Topics Quantum Electron.*, 28(1):1700111, January/February 2022.

[62] M. Streiff, A. Witzig, M. Pfeiffer, P. Royo, and W. Fichtner. A comprehensive VCSEL device simulator. *IEEE J. Select. Topics Quantum Electron.*, 9(3):879–891, 2003.

[63] K. Mehta, Y.-S. Liu, J. Wang, H. Jeong, T. Detchprohm, Y. J. Park, S. R. Alugubelli, S. Wang, F. A. Ponce, S.-C. Shen, R. D. Dupuis, and P. D. Yoder. Lateral current spreading in III-N ultraviolet vertical-cavity surface-emitting

lasers using modulation-doped short period superlattices. *IEEE J. Quantum Electron.*, 54(4):2400507, August 2018.

[64] Crosslight Software Inc., Vancouver, BC, Canada. *Crosslight Device Simulation Software. General Manual*, September 2014.

[65] Synopsys, Inc., Optical Solutions Group, Ossining, NY. *RSoft LaserMOD User Guide, v2018.03*, 2018.

[66] A. Tibaldi, F. Bertazzi, M. Goano, R. Michalzik, and P. Debernardi. VENUS: a Vertical-cavity surface-emitting laser Electro-opto-thermal NUmerical Simulator. *IEEE J. Select. Topics Quantum Electron.*, 25(6):1500212, November/December 2019.

[67] P. Debernardi, A. Tibaldi, M. Daubenschüz, R. Michalzik, M. Goano, and F. Bertazzi. Probing thermal effects in VCSELs by experiment-driven multiphysics modeling. *IEEE J. Select. Topics Quantum Electron.*, 25(6):1700914, November/December 2019.

[68] A. Tibaldi, Jesus A. Gonzalez Montoya, F. Bertazzi, M. Goano, M. Daubenschüz, R. Michalzik, and P. Debernardi. Bridging scales in multiphysics VCSEL modeling. *Opt. Quantum Electron.*, 51(7):231, July 2019.

[69] M. Calciati, A. Tibaldi, F. Bertazzi, M. Goano, and P. Debernardi. Many-valley electron transport in AlGaAs VCSELs. *Semiconductor Sci. Technol.*, 32(5):055007, 2017.

[70] A. Gullino, A. Tibaldi, F. Bertazzi, M. Goano, and P. Debernardi. Reduced dimensionality multiphysics model for efficient VCSEL optimization. *MDPI Appl. Sci.*, 11(15):6908, 2021.

[71] J. W. Scott, R. S. Geels, S. W. Corzine, and L. A. Coldren. Modeling temperature effects and spatial hole burning to optimize vertical-cavity surface-emitting laser performance. *IEEE J. Quantum Electron.*, 29(5):1295–1308, 1993.

[72] G. R. Hadley, K. L. Lear, M. E. Warren, K. D. Choquette, J. W. Scott, and S. W. Corzine. Comprehensive numerical modeling of vertical-cavity surface-emitting lasers. *IEEE J. Quantum Electron.*, 32(4):607–616, 1996.

[73] J. S. Gustavsson, J. A. Vukusic, J. Bengtsson, and A. Larsson. A comprehensive model for the modal dynamics of vertical-cavity surface-emitting lasers. *IEEE J. Quantum Electron.*, 38(2):203–212, 2002.

[74] R. P. Sarzała, P. Mendla, M. Wasiak, P. Maćkowiak, M. Bugajski, and W. Nakwaski. Comprehensive self-consistent three-dimensional simulation of an operation of the GaAs-based oxide-confined 1.3-μm quantum-dot (InGa)As/GaAs vertical-cavity surface-emitting lasers. *Opt. Quantum Electron.*, 36(4):331–347, 2004.

[75] P. Nyakas, G. Varga, Z. Puskás, N. Hashizume, T. Kárpáti, T .Veszprémi, and G. Zsombok. Self-consistent real three-dimensional simulation of vertical-cavity surface-emitting lasers. *J. Opt. Soc. Amer. B*, 23(9):1761–1769, 2006.

[76] M. Grupen and K. Hess. Simulation of carrier transport and nonlinearities in quantum-well laser diodes. *IEEE J. Quantum Electron.*, 34(1):120–140, January 1998.

[77] C. de Falco, E. Gatti, A. L. Lacaita, and R. Sacco. Quantum-corrected drift-diffusion models for transport in semiconductor devices. *J. Comp. Phys.*, 204(2):533–561, 2005.

[78] U. Aeberhard. Photovoltaics at the mesoscale: insights from quantum-kinetic simulation. *J. Phys. D*, 51(32):323002, 2018.

[79] C. Jacoboni. *Theory of Electron Transport in Semiconductors. A Pathway from Elementary Physics to Nonequilibrium Green Functions*. Springer-Verlag, Berlin, 2010.

[80] M. Lades, W. Kaindl, N. Kaminski, E. Niemann, and G. Wachutka. Dynamics and incomplete ionized dopants and their impact on 4H/6H–SiC devices. *IEEE Trans. Electron Devices*, 46(3):598–604, 1999.

[81] R. Heilman and G. Oelgart. Ionization energy of the carbon acceptor in $Al_xGa_{1-x}As$. *Semiconductor Sci. Technol.*, 5:1040–1045, 1990.

[82] B. Deveaud, A. Chomette, D. Morris, and A. Regreny. Carrier capture in quantum wells. *Solid State Commun.*, 85(4):367–371, 1993.

[83] P. Blom, J. Claes, J.E.M. Haverkort, and J. Wolter. Experimental and theoretical study of the carrier capture time. *Opt. Quantum Electron.*, 26:S667–S677, 07 1994.

[84] R. Paiella, G. Hunziker, and K. J. Vahala. TOPICAL REVIEW: Quantum-well capture and interwell transport in semiconductor active layers. *Semiconductor Sci. Technol.*, 14(5):R17–R25, May
1999.

[85] A. Grabowski, J. S. Gustavsson, and A. Larsson. Impact of carrier transport and capture on vcsel dynamics. *IEEE J. Quantum Electron.*, 59(1):1–6, 2023.

[86] S. L. Chuang. *Physics of Photonic Devices*. John Wiley & Sons, Hoboken, 2009.

[87] R. Adar. Spatial integration of direct band-to-band tunneling currents in general device structures. *IEEE Trans. Electron Devices*, 39(4):976–981, April 1992.

[88] R. H. Fowler and L. W. Nordheim. Electron emission in intense electric fields. *Proceedings of The Royal Society A: Mathematical, Physical and Engineering Sciences*, 119:173–181, 1928.

[89] T. A. Ameen, H. Ilatikhameneh, J. Z. Huang, M. Povolotskyi, R. Rahman, and G. Klimeck. Combination of equilibrium and nonequilibrium carrier statistics into an atomistic quantum transport model for tunneling heterojunctions. *IEEE Trans. Electron Devices*, 64(6):2512–2518, June 2017.

[90] E. O. Kane. Zener tunneling in semiconductors. *J. Phys. Conf. Ser.*, 12(2):181–188, 1960.

[91] E. O. Kane. Theory of tunneling. *J. Appl. Phys.*, 32(1):83–89, 1961.

[92] M. Vallone, M. Mandurrino, M. Goano, F. Bertazzi, G. Ghione, W. Schirmacher, S. Hanna, and H. Figgemeier. Numerical modeling of SRH and tunneling mechanisms in high-operating-temperature MWIR HgCdTe photodetectors. *J. Electron. Mater.*, 44(9):3056–3063, 2015.

[93] N. Moulin, M. Amara, F. Mandorlo, and M. Lemiti. Tunnel junction $I(V)$ characteristics: review and a new model for p-n homojunctions. *J. Appl. Phys.*, 126:033105, July 2019.

[94] G. A. M. Hurkx. On the modelling of tunnelling currents in reverse-biased p-n junctions. *Solid-State Electron.*, 32(8):665–668, 1989.

[95] G. A. M. Hurkx, D. B. M. Klaassen, and M. P. G. Knuvers. A new recombination model for device simulation including tunneling. *IEEE Trans. Electron Devices*, 39(2):331–338, 1992.

[96] H.-Y. Wong, D. Dolgos, L. Smith, and M. Rimvydas V. Modified Hurkx band-to-band-tunneling model for accurate and robust TCAD simulations. *Microelectron. Reliability*, 104:113552, January 2020.

[97] Synopsys, Inc., Mountain View, CA. *Sentaurus Device User Guide. Version N-2017.09*, September 2017.

[98] A. Tibaldi, J. A. Gonzalez Montoya, M. G. C. Alasio, A. Gullino, A. Larsson, P. Debernardi, M. Goano, M. Vallone, G. Ghione, E. Bellotti, and F. Bertazzi. Analysis of carrier transport in tunnel-junction vertical-cavity surface-emitting lasers by a coupled nonequilibrium Green's function–drift-diffusion approach. *Phys. Rev. Appl.*, 14(2):024037, August 2020.

[99] D. Esseni, M. Pala, P. Palestri, C. Alper, and T. Rollo. A review of selected topics in physics based modeling for tunnel field-effect transistors. *Semiconductor Sci. Technol.*, 32(8):083005, July 2017.

[100] A. Schenk and S. Sant. Tunneling between density-of-state tails: Theory and effect on Esaki diodes. *J. Appl. Phys.*, 128(1):014502, 2020.

[101] K. Louarn, C. Fontaine, A. Arnoult, F. Olivié, G. Lacoste, F. Piquemal, A. Bounouh, and G. Almuneau. Modelling of interband transitions in gaas tunnel diode. *Semiconductor Sci. Technol.*, 31(6):06LT01, apr 2016.

[102] K. Louarn, Y. Claveau, D. Hapiuk, C. Fontaine, A. Arnoult, T. Taliercio, C. Licitra, F. Piquemal, A. Bounouh, N. Cavassilas, and G. Almuneau. Multi-band corrections for the semi-classical simulation of interband tunneling in GaAs tunnel junctions. *J. Phys. D*, 50(38):385109, sep 2017.

[103] R. Tsu and L. Esaki. Tunneling in a finite superlattice. *Applied Physics Letters*, 22(11):562–564, 1973.

[104] I. Vurgaftman, J. R. Meyer, and L. R. Ram-Mohan. Band parameters for III–V compound semiconductors and their alloys. *J. Appl. Phys.*, 89(11):5815–5875, June 2001.

[105] M. Mazharuddin, A. S. Verhulst, D. Verreck, M. L. Van de Put, W. Magnus, B. Sorée, and G. Groeseneken. Phonon-assisted tunneling in direct-bandgap semiconductors. *J. Appl. Phys.*, 125(1):015701, January 2019.

[106] S. W. Corzine, Randall S. Geels, J. W. Scott, R.-H. Yan, and L. A. Coldren. Design of Fabry-Perot surface-emitting lasers with a periodic gain structure. *IEEE J. Quantum Electron.*, 25(6):1513–1524, June 1989.

[107] G. P. Bava, P. Debernardi, and L. Fratta. Three-dimensional model for vectorial fields in vertical-cavity surface-emitting lasers. *Phys. Rev. A*, 63(2):23816, 2001.

[108] P. Debernardi, G. P. Bava, F. Monti di Sopra, and M. B. Willemsen. Features of vectorial modes in phase-coupled VCSEL arrays: experiments and theory. *IEEE J. Quantum Electron.*, 39(1):109–119, 2003.

[109] P. Debernardi and G. P. Bava. Coupled mode theory: a powerful tool for analyzing complex VCSELs and designing advanced devices features. *IEEE J. Select. Topics Quantum Electron.*, 9(3):905–917, 2003.

[110] P. Debernardi, R. Orta, T. Gründl, and M.-C. Amann. 3-D vectorial optical model for high-contrast grating vertical-cavity surface-emitting lasers. *IEEE J. Quantum Electron.*, 49(2):137–145, 2013.

[111] Y. P. Varshni. Temperature dependence of the energy gap in semiconductors. *Physica*, 34(1):149–154, 1967.

[112] C. Hilsum. Simple empirical relationship between mobility and carrier concentration. *Electron. Lett.*, 10(13):259–260, 1974.

[113] S. Zollner, P. P. Paradis, F. Abadizaman, and N. S. Samarasingha. Drude and Kukharskii mobility of doped semiconductors extracted from Fourier-transform infrared ellipsometry spectra. *J. Vac. Sci. Technol. B*, 37(1):012904, 2019.

[114] E. Haga and H. Kimura. Free-carrier infrared absorption in III-V semiconductors III. GaAs, InP, GaP and GaSb. *J. Phys. Soc. Japan*, 19(5):658–669, 1964.

[115] U. Strauss, W. W. Rühle, and K. Köhler. Auger recombination in intrinsic GaAs. *Appl. Phys. Lett.*, 62(1):55–57, January 1993.

[116] M. Takeshima. Effect of Auger recombination on laser operation in $Ga_{1-x}Al_xAs$. *J. Appl. Phys.*, 58(1):3846–3850, November 1985.

[117] C. Canuto, M. Y. Hussaini, A. Quarteroni, and T. A. Zang. *Spectral methods: evolution to complex geometries and applications to fluid dynamics*. Springer-Verlag, Berlin, 1st edition, 2007.

[118] A. Tibaldi, R. Orta, O. A. Peverini, G. Addamo, G. Virone, and R. Tascone. Skew incidence plane-wave scattering from 2-D dielectric periodic structures: analysis by the mortar-element method. *IEEE Trans. Microwave Theory Tech.*, 63(1):11–19, 2015.

[119] H. K. Gummel. A self-consistent iterative scheme for one-dimensional steady state transistor calculations. *IEEE Trans. Electron Devices*, ED-11:455–465, October 1964.

[120] P. L. George P. J. Frey. *Mesh Generation: Application to Finite Elements*. Wiley ISTE, Reading, MA, 2008.

[121] M. Spevak and T. Grasser. Discretization of macroscopic transport equations on non-cartesian coordinate systems. *IEEE Trans. Computer-Aided Design*, 26(8):1408–1416, 2007.

[122] W. Kausel, G. Nanz, S. Selberherr, and H. Poetzl. A new boundary condition for device simulation considering outer components. In *Simulation of Semiconductor Devices and Processes*, volume 3, pages 625–636, Bologna, September 1988.

[123] E. F. Schubert, L. W. Tu, G. J. Zydzik, R. F. Kopf, A. Benvenuti, and M. R. Pinto. Elimination of heterojunction band discontinuities by modulation doping. *Appl. Phys. Lett.*, 60(4):466–468, 1992.

[124] E. R. Hegblom, D. I. Babic, B. J. Thibeault, and L. A. Coldren. Scattering losses from dielectric apertures in vertical-cavity lasers. *IEEE J. Select. Topics Quantum Electron.*, 3(2):379–389, 1997.

[125] H. K. Bissessur, F. Koyama, and K. Iga. Modeling of oxide-confined vertical-cavity surface-emitting lasers. *IEEE J. Select. Topics Quantum Electron.*, 3(2):344–352, 1997.

[126] S. Adachi. *Properties of Group-IV, III–V and II-VI Semiconductors*. John Wiley & Sons, Chichester, U.K., 2005.

[127] Ioffe Physico-Technical Institute, St. Petersburg, Russia. Physical properties of semiconductors. http://www.ioffe.ru/SVA/NSM/Semicond/index.html.

[128] H. C. Casey, Jr. and M. B. Panish. *Heterostructure Lasers. Part A: Fundamental Principles*. Academic Press, New York, 1978.

[129] S. Adachi. GaAs, AlAs, and $Al_xGa_{1-x}As$: Material parameters for use in research and device applications. *J. Appl. Phys.*, 58(3):R1–R29, August 1985.

[130] M. A. Afromowitz. Thermal conductivity of $Ga_{1-x}Al_xAs$ alloys. *J. Appl. Phys.*, 44(3):1292–1294, March 1973.

[131] A. Tibaldi, A. Gullino, J. A. Gonzalez Montoya, M. G. C. Alasio, A. Larsson, P. Debernardi, M. Goano, M. Vallone, G. Ghione, E. Bellotti, and F. Bertazzi. Modeling tunnel junctions for VCSELs: a self-consistent NEGF-DD approach. In *20th International Conference on Numerical Simulation of Optoelectronic Devices (NUSOD 2020)*, pages 67–68, online, September 2020.

[132] A. Gullino, S. Pecora, A. Tibaldi, F. Bertazzi, M. Goano, and P. Debernardi. A multiscale approach for BTJ-VCSEL electro-optical analysis. In *21st International Conference on Numerical Simulation of Optoelectronic Devices (NUSOD 2021)*, pages 79–80, online, September 2021.

[133] M. D'Alessandro, A. Gullino, A. Tibaldi, F. Bertazzi, M. Goano, and P. Debernardi. Physics-based time-domain modeling of VCSELs. In *22nd International Conference on Numerical Simulation of Optoelectronic Devices (NUSOD 2022)*, pages 61–62, online, September 2022.

[134] M. Farzaneh, R. Amatya, D. Lüerßen, Kathryn J. Greenberg, Whitney E. Rockwell, and J. A. Hudgings. Temperature profiling of VCSELs by thermoreflectance microscopy. *IEEE Photon. Technol. Lett.*, 19(8):601–603, 2007.

[135] S. Gehrsitz, F. K. Reinhart, C. Gourgon, N. Herres, A. Vonlanthen, and H. Sigg. The refractive index of $Al_xGa_{1-x}As$ below the band gap: accurate determination and empirical modeling. *J. Appl. Phys.*, 87(13):7825–7837, 2000.

[136] A. Gullino, A. Tibaldi, F. Bertazzi, M. Goano, M. Daubenschüz, R. Michalzik, and P. Debernardi. Modulation response of VCSELs: a physics-based simulation approach. In *20th International Conference on Numerical Simulation of Optoelectronic Devices (NUSOD 2020)*, pages 65–66, online, September 2020.

[137] S. Adachi, editor. *Properties of Aluminium Gallium Arsenide*. EMIS Datareviews Series. INSPEC, London, 1993.

[138] A. Gnudi, P. Ciampolini, E. Guerrieri, M. Rudan, and G. Baccarani. Small-signal analysis of semiconductor devices containing generation-recombination centers. In *Proceedings of NASECODE V Conference*, pages 207–212. IEEE, Dublin, 1987.

[139] M. Wasiak, P. Spiewak, N. Haghighi, M. Gebski, E. Pruszynska-Karbownik, Paulina Komar, J. A. Lott, and R. P. Sarzała. Numerical model for small-signal modulation response in vertical-cavity surface-emitting lasers. *Journal of Physics D: Applied Physics*, 53(34):345101, jun 2020.

[140] K. L. Lear, V. M. Hietala, H. Q. Hou, J. Banas, B. E. Hammons, J. Zolper, and S. P. Kilcoyne. Small and large signal modulation of 850 nm oxide-confined vertical-cavity surface-emitting lasers. In *Conference on Lasers and Electro-Optics*, page CWA2. Optica Publishing Group, 1997.

[141] D. Wiedenmann, R. King, C. Jung, R. Jager, R. Michalzik, P. Schnitzer, M. Kicherer, and K.J. Ebeling. Design and analysis of single-mode oxidized VCSELs for high-speed optical interconnects. *IEEE J. Select. Topics Quantum Electron.*, 5(3):503–511, 1999.

[142] Y. Ou, J. S. Gustavsson, P. Westbergh, A. Haglund, A. Larsson, and A. Joel. Impedance characteristics and parasitic speed limitations of high-speed 850-nm vcsels. *IEEE Photon. Technol. Lett.*, 21(24):1840–1842, 2009.

[143] A. Al-Samaneh, S. Renz, A. Strodl, W. Schwarz, D. Wahl, and R. Michalzik. Polarization-stable single-mode VCSELs for Cs-based MEMS atomic clock applications. In Krassimir Panajotov, Marc Sciamanna, Angel A. Valle, and Rainer Michalzik, editors, *Semiconductor Lasers and Laser Dynamics IV*, volume 7720, page 772006. International Society for Optics and Photonics, SPIE, 2010.

[144] M. Wasiak, P. Spiewak, P. Moser, J. Walczak, R P Sarzała, T. Czyszanowski, and J. A. Lott. Numerical model of capacitance in vertical-cavity surface-emitting lasers. *J. Phys. D*, 49(17):175104, mar 2016.

[145] Jr. Peter S. Zory. *Quantum Well Lasers*. Ed. Academic Press, Boston, 1993.

[146] B. Tell, K. F. Brown-Goebeler, R. E. Leibenguth, F. M. Baez, and Y.-H. Lee. Temperature dependence of GaAs-AlGaAs vertical cavity surface emitting lasers. *Appl. Phys. Lett.*, 60(6):683–685, 1992.

[147] M. Kamp, G. Mörsch, J. Gräber, and H. Lüth. Te doping of GaAs using diethyl-tellurium. *J. Appl. Phys.*, 76:1974, April 1994.

[148] I. García, I. Rey-Stolle, and C. Algora. Performance analysis of AlGaAs/GaAs tunnel junctions for ultra-high concentration photovoltaics. *J. Phys. D*, 45(4):045101, January 2012.

[149] X. Gan, X. Zheng, Y. Wu, S. Lu, H. Yang, M. Arimochi, T. Watanabe, M. Ikeda, I. Nomachi, and H. Yoshida. GaAs tunnel junction grown using tellurium and magnesium as dopants by solid-state molecular beam epitaxy. *Japan. J. Appl. Phys.*, 53(2):021201, January 2014.

[150] A. Gullino, A. Tibaldi, F. Bertazzi, M. Goano, and P. Debernardi. Multiscale and multiphysics solvers for AlGaAs TJ-VCSEL. In Giuseppe Cocorullo, Felice Crupi, and Ernesto Limiti, editors, *Proceedings of SIE 2022*, pages 190–195, Cham, 2023. Springer Nature Switzerland.

[151] A. E. Bond, P. D. Dapkus, and J. D. O'brien. Aperture placement effects in oxide-defined vertical-cavity surface-emitting lasers. *IEEE Photon. Technol. Lett.*, 10(10):1362–1364, 1998.

[152] B. Demeulenaere, P. Bienstman, B. Dhoedt, and R. G. Baets. Detailed study of AlAs-oxidized apertures in VCSEL cavities for optimized modal performance. *IEEE J. Quantum Electron.*, 35(3):358–367, 1999.

[153] P. Debernardi, G. P. Bava, C. Degen, I. Fischer, and W. Elsäßer. Influence of anisotropies on transverse modes in oxide-confined VCSELs. *IEEE J. Quantum Electron.*, 38(1):73–84, 2002.

[154] M. Goano. Series expansion of the Fermi-Dirac integral $\mathscr{F}_j(x)$ over the entire domain of real j and x. *Solid-State Electron.*, 36(2):217–221, 1993.

[155] J. S. Blakemore. Approximation for Fermi-Dirac integrals, especially the function $\mathscr{F}_{1/2}(\eta)$ used to describe electron density in a semiconductor. *Solid-State Electron.*, 25(11):1067–1076, 1982.

[156] H. C. Casey, Jr. and M. B. Panish. *Heterostructure Lasers. Part B: Materials and Operating Characteristics*. Academic Press, New York, 1978.

[157] J. Piprek, editor. *Handbook of Optoelectronic Device Modeling and Simulation*. CRC Press, Boca Raton, FL, 2017.

List of Publications

Journal papers

1. A. Tibaldi, J. A. Gonzalez Montoya, M. G. C. Alasio, A. Gullino, A. Larsson, P. Debernardi, M. Goano, M. Vallone, G. Ghione, E. Bellotti, and F. Bertazzi. "Analysis of Carrier Transport in Tunnel-Junction Vertical-Cavity Surface-Emitting Lasers by a Coupled Nonequilibrium Green's Function–Drift-Diffusion Approach," *Phys. Rev. Appl.*, 14(2):024037, August 2020.

2. A. Gullino, A. Tibaldi, F. Bertazzi, M. Goano, and P. Debernardi. "Reduced dimensionality multiphysics model for efficient VCSEL optimization," *MDPI Appl. Sci.*, 11(15):6908, 2021.

Conference proceedings

1. A. Gullino, A. Tibaldi, F. Bertazzi, M. Goano, M. Daubenschüz, R. Michalzik, and P. Debernardi. "Modulation response of VCSELs: a physics-based simulation approach", in *20th International Conference on Numerical Simulation of Optoelectronic Devices (NUSOD 2020)*, pages 65–66, online, September 2020.

2. A. Tibaldi, *A. Gullino*, J. A. Gonzalez Montoya, M. G. C. Alasio, A. Larsson, P. Debernardi, M. Goano, M. Vallone, G. Ghione, E. Bellotti, and F. Bertazzi. "Modeling tunnel junctions for VCSELs: a self-consistent NEGF-DD approach," in *20th International Conference on Numerical Simulation of Optoelectronic Devices (NUSOD 2020)*, pages 67–68, online, September 2020.

3. A. Gullino, S. Pecora, A. Tibaldi, F. Bertazzi, M. Goano, and P. Debernardi. "A multiscale approach for BTJ-VCSEL electro-optical analysis," in *21st International Conference on Numerical Simulation of Optoelectronic Devices (NUSOD 2021)*, pages 79–80, online, September 2021

4. M. D'Alessandro, A. Gullino, A. Tibaldi, F. Bertazzi, M. Goano, and P. Debernardi. "Physics-based time-domain modeling of VCSELs," in *22nd International Conference on Numerical Simulation of Optoelectronic Devices (NUSOD 2022)*, pages 61–62, online, September 2022

5. A. Gullino, A. Tibaldi, F. Bertazzi, M. Goano, and P. Debernardi. "Multiscale and multiphysics solvers for AlGaAs TJ-VCSEL," in Giuseppe Cocorullo, Felice Crupi, and Ernesto Limiti, editors, *Proceedings of SIE 2022*, pages 190–195, Cham, 2023. Springer Nature Switzerland